André Filipe Ferreira Violas

Bachelor in Micro and Nanotechnologies Engineering

Novel Rear Contact Architectures in CIGS Solar Cells: Modelling and Experimental Fabrication

Dissertation submitted in partial fulfillment
of the requirements for the degree of

Master of Science in
Micro and Nanotechnology Engineering

Adviser:	Doctor Pedro Salomé, Group Leader, International Iberian Nanotechnology Laboratory and Associate Professor, University of Aveiro
Co-adviser:	Doctor Hugo Águas, Associate Professor, NOVA University of Lisbon

Examination Committee

Chair:	Rodrigo Martins, Full Professor, NOVA University of Lisbon
Rapporteur:	Karl Adam Hultqvist, Researcher, Uppsala University
Member:	Pedro Salomé, PhD, International Iberian Nanotechnology Laboratory

FACULDADE DE CIÊNCIAS E TECNOLOGIA
UNIVERSIDADE NOVA DE LISBOA

December, 2020

Novel Rear Contact Architectures in CIGS Solar Cells: Modelling and Experimental Fabrication

Para o meu pai,

Acknowledgements

My journey on the last 5 years throughout the course of Micro and Nanotechnology Engineering was fulfilled with amazing people that gave me strength to keep going and to achieve my results. I want to thank you all!

First, I would like to acknowledge Prof. Dr. Rodrigo Martins and Prof. Dr. Elvira Fortunato for the creation of the course I am finishing with this work and for providing access to the facilities of CENIMAT|I3N and CEMOP that allowed me to be in contact with state-of-the-art equipment. Additionally, I want to thank all the great professors at the Materials Science Department, all very helpful and motivating.

Quero agradecer toda a ajuda e dedicação demonstrada pelo meu orientador Prof. Dr. Pedro Salomé, mesmo nos tempos mais difíceis da pandemia e onde tive de alterar parte do meu tema de tese. Deste-me a oportunidade de poder trabalhar num grupo acolhedor, NOA, no INL durante dois estágios de verão e também de realizar esta tese. Admiro todo o esforço, dedicação, conhecimento e espírito de entreajuda dispendidos a todo o grupo contribuindo para um ótimo ambiente de trabalho e para o avanço das tarefas do dia-a-dia. Quero também agradecer toda a ajuda e grande contributo para a minha candidatura com sucesso a doutoramento, tanto ao Pedro com ao Prof. Dr. Paulo Fernandes e à Dr. Jennifer Teixeira! Eu apenas fui ajudando onde era necessário.

Ao meu co-orientador Prof. Dr. Hugo Águas, na FCT/NOVA, por toda a ajuda e por todo o trabalho realizado nestes 5 anos numa posição exigente como é a de coordenador de curso. Sempre que foi necessário o professor esteve sempre disponível para ajudar.

Obrigado a todos do grupo NOA que estiveram comigo durante a minha tese no INL! Ao Paulo e Jennifer que com o seu conhecimento e boa disposição sempre me ajudaram a mim e a todo o grupo. Ao Kevin, Tomás, Barbosa, António e Marco pela ajuda nos trabalhos em sala limpa e muito boa disposição em todos os momentos, destaco as excelentes imagens de cross-section no SEM obtidas tanto pelo Kevin como pelo Marco. Quero realçar a ajuda disponibilizada pelo Tomás e pelo António, além do Pedro e da Jennifer, nas minhas simulações elétricas, muito obrigado! Ao Miguel que desde o início do primeiro estágio no INL sempre se mostrou disponível para me ajudar e tirar dúvidas em qualquer momento. Deixo o meu agradecimento especial aos meus companheiros de tese, à Célia, ao Barbosa e à Margarida, que apesar desta pandemia conseguimos acabar todo o trabalho relacionado com a tese.

Agradeço à minha família que sempre me apoiou desde a minha mudança para este curso até à realização da tese em Braga. Dedico este trabalho da tese, que representa o culminar dos últimos 5 anos na Universidade, ao meu pai! Sei que gostarias de poder ter visto todo o meu persurso académico na Universidade e provavelmente foste quem fez crescer em mim o gosto pela ciência desde muito cedo.

O apoios dos vários colegas de curso foi também importante para o meu sucesso académico. João Durand não sei se consigo apanhar o comboio.

Em especial, meh obrigado Luís, obrigado Rui, obrigado Tiago e obrigado Célia, por me terem acompanhado nesta jornada e por ter tido a oportunidade de partilhar tantos momentos bons dentro e fora da faculdade! Não teria sido o mesmo sem vocês.

Tiago e Célia, vocês são quem mais de perto me acompanhou em todo este percurso, agradeço-vos muito por tudo, tanto a nível académico como pessoal! Um abraço longo Tiago.

Célia solar, além de praticamente todo o curso ainda tiveste a paciência de me acompanhar de perto também na tese. Muito obrigado por me teres ajudado ao longo destes anos e por todas as conversas, mesmo. Tens a capacidade de fazer tudo o que quiseres!

Abstract

$Cu(In,Ga)Se_2$ (CIGS) solar cells are amongst the best performing thin-film technologies mainly due to post-deposition treatment (PDT) improvement of the last years. However, the electrical simulation baseline models did not quite follow the experimental results. Moreover, there is no baseline model for recent CIGS solar cells until the time of writing of this thesis, whereas a scientific paper is already being written to be submitted, to provide with an updated model.

This study provided with an updated experimentally-based baseline model for electrical simulations in SCAPS-1D with the incorporation of the PDT effects and high-efficient device characteristics. This baseline model produces comparable results with high-efficient 22.6 % record cell from ZSW. In order to be even more cost and environmental competitive with the widely used silicon photovoltaic technology, it is important the implementation of ultra-thin devices. However, electrical and optical limitations prevent the widespread of these devices, such as rear recombination and insufficient light absorption. The baseline model is applied to ultra-thin absorbers, whereas an increased bulk CIGS defect density is necessary to model the experimental data. Furthermore, simulations results reveal that by addressing these limitations would be possible to achieve an ultra-thin solar cell with at least 19.0 % power conversion efficiency, with open circuit voltage values even higher compared to the ZSW record cell.

On the other hand, it is shown the feasibility of the fabrication of a metal/dielectric structure at the rear contact with industrial-friendly processes. The innovative rear contact has the potential to tackle the rear recombination with the passivating dielectric and improving light absorption with the high reflecting metal layer in ultra-thin devices. Such structure effectively with both benefits has not been reported yet.

Keywords: SCAPS-1D, electrical simulations, baseline model, CIGS solar cells, ultra-thin, rear contact

Resumo

A tecnologia fotovoltaica Cu(In,Ga)Se_2 (CIGS) apresenta das maiores eficiências de conversão, considerando as tecnologias de filme-fino, devido principalmente aos avanços no processo de tratamento pós-deposição (do inglês PDT) nos últimos anos. No entanto, os modelos base para simulações elétricas não acompanharam esta evolução experimental. Além do mais, não existe um modelo base adaptado às células CIGS mais recentes até ao momento, pelo que um artigo científico já está a ser escrito e preparado para submissão.

Este estudo desenvolve um modelo base para simulações elétricas, em SCAPS-1D, atualizado e realista onde se incorpora os efeitos associados ao PDT e outras características de células de alta eficiência. O modelo produz resultados comparáveis com a célula recorde da ZSW de 22.6 % de eficiência. De forma a aumentar a competitividade ambiental e em custos de fabrico, em comparação com a tecnologia dominante no mercado, o silício, é importante a implementação de dispositivos ultra-finos. No entanto, existem limitações elétricas e óticas que impedem a sua utilização massiva, tais como recombinação de portadores no contacto posterior e insuficiente absorção da luz solar. O modelo base é aplicado em células ultra-finas, no qual foi necessário aumentar a densidade de defeitos no interior do CIGS de forma a ajustar os resultados aos dados experimentais. Além disto, resultados das simulações revelam que ultrapassando estas limitações será possível alcançar células solares ultra-finas com eficiência de pelo menos 19 %, sendo mesmo os valores de tensão em circuito aberto superiores aos da célula recorde da ZSW.

Adicionalmente, mostrou-se a viabilidade do fabrico experimental de uma estrutura metal/-dielétrico no contacto posterior da célula através de processos compatíveis com a indústria. Esta inovação tem o potencial de combinar a passivação com o aumento da reflexão em dispositivos ultra-finos. Tal estrutura com efetivamente ambos o benefícios não foi reportado ainda.

Palavras-chave: SCAPS-1D, simulações elétricas, modelo base, células solares CIGS, ultrafino, contacto posterior

Contents

List of Figures xv

List of Tables xix

Acronyms xxi

Symbols xxiii

Motivation and Objectives xxiii

1 Introduction 1
- 1.1 Solar Cells . . . 1
- 1.2 CIGS Technology . . . 2
  - 1.2.1 Standard CIGS Solar Cell Layers . . . 3
- 1.3 Ultra-Thin CIGS Solar Cells . . . 4
  - 1.3.1 Losses Mitigation Strategies . . . 4
- 1.4 Modelling . . . 5

2 Materials and Methods 7
- 2.1 Electrical Simulations SCAPS-1D . . . 7
- 2.2 Experimental Rear Passivation Structure . . . 8
  - 2.2.1 Calibration . . . 8
  - 2.2.2 Fabrication and Characterisation . . . 10

3 Results and Discussion 13
- 3.1 Baseline Model: to High-Efficiency Devices . . . 13
  - 3.1.1 Baseline Initial Set . . . 13
  - 3.1.2 Electrical Parameters Optimisation . . . 14
  - 3.1.3 Optical Parameters Optimisation . . . 22
- 3.2 Baseline Model: to Ultra-Thin Devices . . . 25
  - 3.2.1 Modelling . . . 25
  - 3.2.2 Modelling Validation with Experimental Data . . . 27
- 3.3 Limitations of Ultra-Thin Solar Cells . . . 28
  - 3.3.1 Optical Limitations . . . 28
  - 3.3.2 Recombination Losses Limitations . . . 29
- 3.4 Experimental Rear Passivation Structure . . . 31
  - 3.4.1 Calibration . . . 31
  - 3.4.2 Lift-off . . . 32

4 Conclusion and Future Perspectives 35

Bibliography 37

Appendices 49

A SCAPS-1D Parameters 49

B Supplementary Figures and Tables 53

Annexes 59

I Program to Retrieve Figures of Merit in SCAPS-1D **59**

List of Figures

1.1 J-V curves characteristic of solar cells, adapted from [24] 1

1.2 Standard layer structure of CIGS solar cells, layers not at scale. 3

1.3 Crystal structure of the CIGS absorber (a) and chalcopyrite polytype of $CuIn_5Se_8$ ordered vacancy compound (b). Adapted from [54]. 4

2.1 Mask used in the calibration process. Pitch of 2.8 μm and exposure line width of 1.2, 1.4, and 1.6 μm. Note that in the results chapter it is only presented the 1.6 μm line width results. 9

2.2 Fabrication steps to obtain the desired rear structure: adjusted to an RBC solar cell [77], which already has the metal layer; and the alternative on the conventional Mo coated SLG. Layers thicknesses: Al - 10 nm; 2nd Mo - 30 nm; LOR 5B - 500 nm; AZ1505 - 600 nm; Al_2O_3 - 18 nm. Not at scale. Note the more directional Al deposition and more conformal Al_2O_3 deposition in the alternative path. 11

3.1 Scheme of the layers used in the SCAPS-1D model, thicknesses not at scale. Initial layers thickness: CIGS 1.8 µm; SDL 15 nm; CdS 50 nm; i:ZnO 100 nm; AZO 300 nm. 13

3.2 Bandgap gradings of the initial model (1a) and the incorporated double grading. The initial model has a CIGS layer thickness of 1.8 µm, while for the double grading model this absorber thickness is 2.5 µm separated into two Ga gradients. 16

3.3 Shallow acceptors grading profile and indication of the shallow donor defect density incorporated in the CIGS layer. It is compared the cases with and without n-type inversion. 18

3.4 GB defect grading profile due to the effects of PDT at the CIGS/CdS interface. It is compared with the previous case without grading. 20

3.5 Band diagrams obtained for the solar cell model simulation: before changes in Further optimisation sub section (left); after CBO update (right). 21

3.6 EQE response curve for the sequential modifications in the solar cell layers. Inset, it is presented the J_{sc} increase with each modification. It is noted that the ZMO thickness reduction does not affect the solar cell performance. 22

3.7 Left - EQE response curves comparing the rear optical reflection of 0 % with the presented Mo rear optical reflection (dashed line) obtained with the Lumerical 3D optical simulations. Right - EQE response varying the front reflection at fixed values and with optical simulated Mo rear optical reflection. 24

3.8 Left - ARC thickness test from 80 nm to 150 nm in steps of 10 nm, with EQE response curves and respective front reflection values. The optimised ARC thickness lead to a J_{sc} value of 36.59 $mA \cdot cm^{-2}$. Note that the others Figures of Merit do not change significantly its values. The J_{sc} values inset follow the same thickness colour code. Right - EQE response curve with the optimised ARC and additional CIGS roughness, which is used in the baseline model for high-efficiency devices. 24

3.9 Scheme with the Figures of Merit results of the different combinations test: double/single defects and low/high defect. The double defects refers to double acceptors/donors already mentioned in this study, while the single defects replaces the double defects and uses the CIGS bulk defect used in the initial model, Table A.2 and Table A.1 respectively. The High defect represent an overall increase in the CIGS bulk defects: GB defect density increases from $5.0{\times}10^{15}\,cm^{-3}$ wo PDT and the grading $5.0{\times}10^{13}$ - $2.0{\times}10^{13}\,cm^{-3}$ PDT to $1.5{\times}10^{16}/7.5{\times}10^{15}\,cm^{-3}$ (double/single defects) wo PDT and $5.0{\times}10^{15}$ - $2.0{\times}10^{15}/5.0{\times}10^{14}$ - $2.0{\times}10^{14}\,cm^{-3}$ (double/single defects) PDT. Additionally, only for single defects, GB defect density increase for high defects is coupled with the CIGS single bulk defect density increase from $1.0{\times}10^{14}$ to $2.6{\times}10^{15}\,cm^{-3}$. Please see Table 3.9 for experimental results. 26
3.10 Left - Comparison between the simulated (filled squares with dashed connecting lines) and measured (filled stars) solar cells figures of merit. The solid lines represent the uncertainty associated with each device measurement, also present in Table 3.9. Right - J-V curves for different $KInSe_2$ thickness from 0 to 50 nm, that was incorporated into the model (without passivation) between the SDL and CdS layers. The same trend is observed for the model with passivation (not shown here). 28
3.11 EQE curves for the optical optimisation at both the rear and front contact (left) and only at the front contact (right), with the model including PDT and passivation. J_{sc} improvements are presented inset. The thin CdS and ZnO layers at the left light blue curve refers to the thickness used in baseline model for high-efficiency devices. 29
3.12 Figures of Merit values for different recombination velocity values at the rear contact. It was used the model with PDT without passivation and without R_s and R_p. 30
3.13 Impact of the GB defect density on the ultra-thin solar cell performance for the model with PDT without passivation (left) and with passivation (right). Note that with rear passivation, the defect density decrease lead to a V_{oc} value higher compared with the high-efficiency record cell from ZSW. 30
3.14 SEM cross-section image of the resists profile with the chosen combination of parameters I 60 %, F -40 and development time 40 s. 32
3.15 SEM cross-section image before (a) and after (c) the lift-off, and top image (b) after the lift-off. The dimensions presented within the images correspond to 10 different measurements at different locations and images with the same scale. 33

B.1 Bulk and interface recombination currents with (left) and without (right) the SDL layer. 53
B.2 Cross-section test with the variation of electrons (bottom) and holes (top) capture cross-section, in the double donors (left) and double acceptors (right) defects. . . . 53
B.3 Band diagram adapted from [132] illustrating the Fermi level (E_F) pinning process. Here E_F is pinned at energy E_4, with other possible three defect levels at the interface. The E_F pinning at E_4 provides the highest V_{oc} in opposition with the pinning at E_1. 54
B.4 J-V curve comparison between the baseline model obtained with this study and the experimental result of the high-efficiency record cell from ZSW. 54
B.5 Optical microscope images for the calibration of the DWL laser Focus and Intensity conditions together with the development time. All the exposed lines presented here have 1.6 μm width and 2.8 μm pitch. Note the different scale unit at different images. 55
B.6 AFM analysis of the substrate after the lift-off, the correspondent SEM image is shown in Figure 3.15 b) and c). It is demonstrated the dielectric thickness with the linear profile (right) through 10 measurements at different locations, and as an example it is presented the referred linear profile on the gray line at AFM image (left). 56
B.7 SEM top image pf the substrate after the lift-off. This SEM image is an example of the uniformity of the lines dimension obtained with this study. 56

B.8 SEM image of the successful lift-off of the ALD alumina deposited at ≈ 100 ºC. However, this lift-off was done before the DWL exposure calibration to assess the viability of the ALD high-quality dielectric lift-off and does not have the proper line dimensions, as it is possible to see by the areas without lines where the resist peeled-off. 57

I.1 Example of an output Excel sheet of the VBA program to retrieve the Figures of Merit from the .txt file obtained with the SCAPS-1D simulation results. 59

I.2 Example of an output .txt file obtained with SCAPS-1D I-V simulations with the Figures of Merit values. 59

List of Tables

3.1 Comparison of the simulation results obtained with Pettersson's model (which has the SDL layer) and the initial model of this study. Pettersson's model η was calculated from the respective figures of merit. Additional SDL test with the result for the initial model without the SDL layer . . . 14

3.2 Adoption of native defects and addition of GB defect to the bulk CIGS and comparison with the simulation results for the initial model. $^{*}R_s$ here is set to 0 Ω. . . . 16

3.3 Comparison of results between the model with the incorporated bandgap double grading and the previous model with linear grading. The respective bandgap gradings are present in Figure 3.2 . . . 17

3.4 Comparison of the results with and without n-type inversion at the CIGS surface, incorporated in the model 3. The respective shallow acceptor grading profiles are present in Figure 3.3. The shallow acceptor density values were increased, compared to the initial model, due to PDT . . . 18

3.5 Solar cell results with the incorporation of GB passivation due to PDT and comparison with previous results (4b). The GB passivation was obtained through the reduction in the GB defect density. The results correspond to the case without n-type inversion . . . 19

3.6 Solar cell results with the incorporation of GB defect grading due to the effects of PDT at the interface and comparison with previous results of GB passivation at model 5. The grading profile is present in Figure 3.4 . . . 20

3.7 Results for the solar cell model with the sequential modification of the E_F pinning, CdS N_t increase and CBO update, compared with the previous result of the PDT interface effect at model 6 . . . 21

3.8 Simulation results for the final updated model, i.e. baseline model to high-efficiency devices. The value in brackets represent the J_{sc} value considering the 1.7 % grid coverage in real devices. Additional comparison with the experimental data of the record cell from ZSW . . . 25

3.9 Simulated and experimental (in brackets with averages and standard deviation values) results for the 3 devices in [94]. The simulated results follow the combination of double defects + high defects from Figure 3.9. In this simulation, it was introduced the experimental series and shunt resistances for each device [94] . . . 27

A.1 Parameters used in SCAP-1D for the initial model. All defects are mid-gap defects, except for the E_F pinning interface defect which are placed 0.2 eV below E_c. See Symbols chapter for all parameters meaning. "A" stands for acceptor, "D" for donor, and "N" for neutral. This initial model represents the previous baseline from Pettersson *et al.* [15]. . . . 49

A.2 Parameters used in SCAP-1D for the baseline model for high-efficiency devices obtained with this study. The interface defects are the same as in Table A.1, except the removal of the E_F pinning defect. Furthermore, the optical reflection simulations are presented and discussed in chapter 3. See Symbols chapter for all parameters meaning. "A" stands for acceptor, and "D" for donor. . . . 50

A.3 Parameters used in SCAP-1D for the baseline model for ultra-thin devices. The interface defects are the same as in Table A.1, except the removal of the E_F pinning defect. Furthermore, the optical reflection simulation is presented and discussed in chapter 3. See Symbols chapter for all parameters meaning. "A" stands for acceptor, and "D" for donor. . . . 51

B.1 Resume of the simulation results for the optical optimisation steps of the baseline model to high-efficiency devices, without considering the ARC optimisations. . . . 55

Acronyms

AFM	atomic force microscopy
ALD	atomic layer deposition
ARC	anti-reflective coating
AZO	ZnO:Al
CBO	conduction band offset
C-V	capacitance - voltage
CBD	chemical bath deposition
CBM	conduction band minimum
CIGS	$Cu(In,Ga)Se_2$
DWL	direct write laser
EDX	energy-dispersive X-ray spectroscopy
EQE	external quantum efficiency
FDTD	Finite-Difference Time-Domain
GB	grain boundary
GGI	[Ga]/([Ga] + [In])
i:ZnO	intrinsic ZnO
INL	International Iberian Nanotechnology Laboratory
IR	infra-red
ITO	In_2O_3:Sn
J-V	current density - voltage
ODC	ordered defect compound
OVC	ordered vacancy compound
PDT	post-deposition treatment
PR	photoresist
PV	photovoltaic
RBC	reflective back contact
RIE	reactive-ion etching
SCR	space charge region
SDL	surface defect layer
SEM	scanning electron microscopy
SLG	soda-lime glass
SRH	Shockley-Read-Hall

TCO	transparent conductive oxide
TRPL	time-resolved photoluminescence
UV	ultra-violet
VBA	Visual Basic for Applications
VBO	valence band offset
ZMO	$Zn_{1-x}Mg_xO$
ZSW	Center for Solar Energy and Hydrogen Research Baden-Württemberg

Symbols

A	Ideality factor	
Cd_{Cu}	Cd on Cu antisite defect	
σ_h	Hole capture cross-section	cm^2
σ_e	Electron capture cross-section	cm^2
Cu_{In}	Cu on In antisite defect	
D_e	Diffusion coefficient of electrons	
D_h	Diffusion coefficient of holes	
E_c	Energy level at conduction band minimum	eV
E_F	Fermi level energy	eV
η	Light to power conversion efficiency	%
m_e^*	Electron effective mass	Kg
m_h^*	Hole effective mass	Kg
E_g	Bandgap	eV
χ_a	Electro-affinity	eV
E_t	Bulk trap defect position	eV
E_v	Energy level at valence band maximum	eV
F	DWL laser focus	
FF	Fill factor	%
G	Carriers generation rate	
h	Planck constant	$m^2Kg \cdot s^{-1}$
I	DWL laser intensity	%
In_{Cu}	In on Cu antisite defect	
N_A^-	Ionised acceptor defect concentration	cm^{-3}
N_D^+	Ionised donor defect concentration	cm^{-3}
J	Current density	$mA \cdot cm^{-2}$
J_{mp}	Current at the solar cell's maximum power working point	$mA \cdot cm^{-2}$
J_n	Electrons current density	$mA \cdot cm^{-2}$
J_0	Saturation current density	$mA \cdot cm^{-2}$
J_p	Holes current density	$mA \cdot cm^{-2}$
J_{ph}	Photogenerated current density	$mA \cdot cm^{-2}$
J_{sc}	Short-circuit current density	$mA \cdot cm^{-2}$
k_B	Boltzmann constant	$J \cdot K^{-1}$
λ	Wavelength	nm

μ_e	Electron mobility	$cm^2 \cdot V^{-1}s^{-1}$
μ_h	Hole mobility	$cm^2 \cdot V^{-1}s^{-1}$
n	Electrons charge concentration	cm^{-3}
N_A	Shallow acceptor defect density	cm^{-3}
N_c	Density of states at conduction band minimum	cm^{-3}
N_D	Shallow donor defect density	cm^{-3}
N_{it}	Interface trap density	cm^{-2}
N_t	Bulk trap density	cm^{-3}
N_v	Density of states at valence band maximum	cm^{-3}
p	Holes charge concentration	cm^{-3}
ϵ	Dielectric permittivity	$F \cdot m^{-1}$
ϵ_r	Relative dielectric permittivity	$F \cdot m^{-1}$
P_{inc}	Incident power on a solar cell	$W \cdot m^{-2}$
q	Electronic charge	C
R	Carriers recombination rate	
R_p	Parallel, or shunt, resistance	Ω
R_s	Series resistance	Ω
SRV	Surface recombination velocity	$cm \cdot s^{-1}$
T	Temperature	K
V	Voltage	V
V_{Cu}	Cu vacancy defect	
V_{In}	In vacancy defect	
V_{mp}	Voltage at the solar cell's maximum power working point	V
V_{oc}	Open-circuit voltage	V
V_{Se}	Se vacancy defect	
v_{th}^h	Hole thermal velocity	$m \cdot s^{-1}$
v_{th}^e	Electron thermal velocity	$m \cdot s^{-1}$

Motivation and Objectives

Over the past years there has been an increasing awareness on the problem of climate change as well as on limited resources of the planet [1, 2]. It is well known that the consumption of fossil fuels has a huge negative impact on the planet ecosystem.

On the other side there are the less pollutant renewable energy resources. Here, the energy arising from the sun stands in the pole position. As an example of sun energy potential, in the small country of Portugal, in a region with an area of 31 711 km^2 and assuming a solar irradiance of 1 kW/m^2 on a clear sunny day, the sun energy reaching this region surface during 7 months would give the energy we need to supply the world total energy consumption in a year, which is about 160 000 TWh in 2019 [3, 4].

So, to overcome the world demand for electrical energy, devices that harvest solar energy and convert it into usable electrical energy are of utmost importance. This is precisely what photovoltaic (PV) devices are capable of doing. The PV systems rapid growth and cost effectiveness can heavily contribute to the de-carbonization towards a sustainable future [4–6]. According to [1] a global solar PV energy generation will have a share of about 69 % of the total electricity generated in 2050, which is a good indicator for the photovoltaics importance in the future.

Several technologies already claim their position in the market. Furthermore, thin-film solar cells are already cost [7, 8] and environmental [9] competitive compared with silicon that dominates the industry. Cu(In,Ga)Se_2 (CIGS) thin-film technology has unique characteristics and numerous advantages over mono- and multi-crystalline silicon solar cells, some include: possibility of flexible and low-weight substrates [10, 11]; high performance under low-irradiance conditions, ideal for building integrated photovoltaics [12]; superior performance with high cell record of power conversion efficiency of 23.35 % [13]; and great sustainability indicators over the competition [9].

To further lower the fabrication costs and increase the manufacture throughput of CIGS devices researchers worldwide are taking efforts in ultra-thin absorbers solar cells. The ultra-thin solar cells employ absorber thicknesses below 1 μm with the environmental advantage of lower In and Ga consumption, which are considered as scarce elements on Earth [14].

The further comprehension on CIGS properties will enable even further developments in the correspondent solar devices. Electrical simulations may take part in this path to understand the mechanisms limiting the performance of such devices. The best practice of simulation includes the change of a few parameters, to clearly discriminate the corresponding effects. So, an important requirement is to set a baseline, i.e. a base model that describes the performance and results of the current high-efficiency solar cells. The last updated and realistic baseline, with various parameters verified experimentally, was established in 2011 by Pettersson *et al.* [15]. Following the even older and widely used baseline from Gloeckler *et al.* in 2003 [16].

Since 2011, many advances occurred in CIGS thin-film technology that boosted the performance of solar cells. The power conversion efficiency was enhanced from 20.3 % [17] to the current world record laboratory cell of 23.35 % [13]. This improvement in the solar cell performance is mainly due to the recent development of a post-deposition treatment (PDT) with heavy alkali fluorides and to other minor improvements in the materials properties of the solar cell layers. Furthermore, the effects of PDT that benefits the performance of the solar cells are not included in the Pettersson's baseline model, which is the last relevant and experimentally verified baseline and whom power conversion efficiency is 17 %.

The main objective of this work is to develop an updated and realistic electrical baseline model that tackle the recent PDT developments in CIGS technology and include high-efficiency CIGS features, to be reported in the literature. Furthermore, the baseline model for high-efficiency solar cells is tested for ultra-thin devices. The results obtained provide a baseline set for ultra-thin CIGS solar cells as well and indicate at some extent better performances than the

thicker counterparts.

The experimental study aims to provide an industrial-friendly process through lift-off to fabricate a metal/dielectric innovative rear structure that address some limitations in ultra-thin CIGS solar cells.

1 | Introduction

This chapter gives an introductory overview of the important concepts to understand this work. It ranges from the basic solar cell functioning to the CIGS technology and its state of the art.

1.1 Solar Cells

A solar cell is a p-n junction based device that converts the sunlight energy into electrical energy through the photovoltaic effect. To achieve a p-n junction one simply needs to join two semiconductor materials, p- and n-type. Such structure is the basis of a diode, so an easy way to model the solar cell behaviour is by using the Shockley one-diode model [18, 19] through the following equation 1.1.

$$J = J_0\left(\exp\left(\frac{qV}{Ak_BT}\right) - 1\right) \tag{1.1}$$

Where J is current density that passes across the diode, J_0 is the saturation current density, q is the electronic charge, V is the voltage applied to the diode, A is the diode ideality factor, k_B is the Boltzmann constant and T is the temperature.

It is possible to describe a solar cell as an illuminated diode. The photons with energy higher than the bandgap excite the electrons in the absorber semiconductor and generate electron-hole pairs. These additional minority charge carriers are separated due to the built-in electric field of the space charge region (SCR) in the junction. Whereas the charge carriers generated at a distance within its diffusion length of the SCR, and also the ones in the SCR, can be collected [20]. Consequently, the solar cell outputs a photogenerated current J_{ph}, which promotes a vertical shift in the characteristic diode current-voltage I-V curve [21], Figure 1.1. The term J_{ph} is added and presented in equation 1.2.

However, this description of the solar cell's behaviour is rather ideal. To account for some realistic losses [21, 22], it is introduced the series resistance R_s and parallel, or shunt, resistance R_p, equation 1.2 [23]. So, it is considered the effects from electrodes and other ohmic losses and leakage currents [19, 20, 22].

$$J = J_0\left(\exp\left(\frac{qV - qJR_s}{Ak_BT}\right) - 1\right) + \frac{V - JR_s}{R_p} - J_{ph} \tag{1.2}$$

Solar cells are easily characterised with characteristic current density - voltage (J-V) curves, Figure 1.1. Furthermore, to reliably compare different devices there is some Figures of Merit that allow to assess the performance of solar cells.

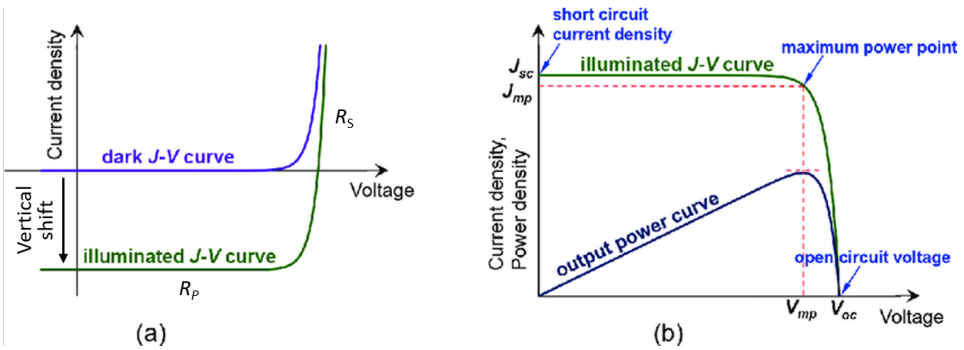

Figure 1.1: J-V curves characteristic of solar cells, adapted from [24]

J-V curves provide most of the following performance parameters: short-circuit current density J_{sc}, which is the current for 0 V applied voltage; open-circuit voltage V_{oc}, which represents the voltage for no current passing through the solar cell; fill factor FF, which indicates how close, in percentage, the solar cell is from its maximum potential power considering the V_{oc} and J_{sc}, see equation 1.3; and light to power conversion efficiency η, which relates to the solar cell conversion efficiency. Additionally, it is possible to extract from J-V curves the current and voltage of the solar cell working in its maximum power point, J_{mp} and V_{mp} respectively, as well as the R_s and R_p resistances. Equations 1.3 and 1.4 describe the relation of the FF with current and voltage parameters and the expression to obtain η, respectively.

$$FF = \frac{J_{mp} V_{mp}}{J_{sc} V_{oc}} \tag{1.3}$$

$$\eta = \frac{J_{mp} V_{mp}}{P_{inc}} = \frac{J_{sc} V_{oc} FF}{P_{inc}} \tag{1.4}$$

Whereas P_{inc} refers to the incident power of light per area on the solar cell.

Other possible characterisation can be performed through external quantum efficiency (EQE) curves. External quantum efficiency describes the ratio of the number of collected charge carriers to the number of incoming photons for different wavelength values. Therefore, it is obtained the efficiency of the solar cell in converting photons into charge carriers at the respective absorption wavelength range of the device, which provides an additional information about possible absorption losses.

1.2 CIGS Technology

CIGS thin-film solar cells are amongst the most efficiency PV devices in thin-film technology [25], with a power conversion efficiency of 23.35 % [13], being comparable with the non-crystalline Si solar cells

The beginning of the CIGS technology history dates to the decade of 1970's and took place at the Bell Laboratories. Wagner *et al.* were fabricating photo-detectors when they found the potential of $CuInSe_2$/CdS p-n junction to be applied in solar cell devices [26]. From this discovery they focused on solar cell characteristics and were able to produce solar cell with 12 % power conversion efficiency [27]. Since the devices fabricated by Wagner *et al.* several improvements in CIGS-based device properties enhanced its power conversion efficiency [28] to the current 23.35 %. They include the Ga doping in the original $CuInSe_2$ chalcopyrite material [29–31], which enabled the increase and tuning of the bandgap between ≈ 1.0 eV to ≈ 1.7 eV [32], and improved deposition techniques for both CIGS and CdS layers, such as the co-evaporation in one- or three-stage process [33, 34] and the chemical bath deposition (CBD) [35], respectively. Furthermore, doping with alkali elements, which started with the diffusion of Na from the substrate [36], to the most recent post-deposition treatment (PDT) with heavier alkalies [13, 37–40], further improved the CIGS properties. The alkali PDT process consists in the evaporation of an alkali-fluoride, such as KF, RbF or CsF, after the CIGS deposition in a Se atmosphere, with consequent alkali diffusion into the CIGS [37, 38].

A recent strategy to lower the fabrication costs and increase the manufacture throughput of CIGS devices is the transfer from thin to ultra-thin absorbers solar cells. The ultra-thin solar cells employ absorber thicknesses below 1 μm with the advantage of lower bulk recombination compared to the thicker counterparts [41], together with the environmental advantage of lower In and Ga scarce elements consumption. However, the recombination occurring at interfaces increase its impact on device performance due to the increase of the generated charge carriers near the rear interface. Moreover, the thinner absorber lead to an insufficient light absorption. Strategies to mitigate the referred ultra-thin solar cell limitations are discussed below in section 1.3.

1.2.1 Standard CIGS Solar Cell Layers

Typically, the conventional CIGS solar cells are composed by the layers present in Figure 1.2. The soda-lime glass (SLG) is as the common substrate to be used in the industry and at the laboratory scale. During the CIGS growth, Na diffuses into the CIGS absorber improving its structural and electrical properties [36, 42], as already mentioned. Additional advantages of SLG is its low cost, accessibility and the expansion coefficient being near the CIGS coefficient value [28].

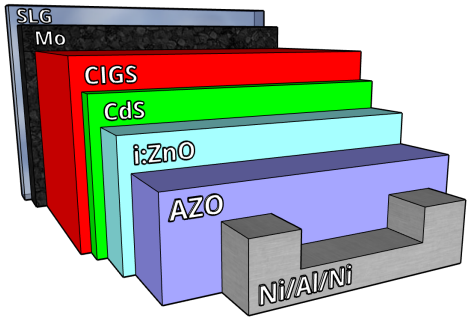

Figure 1.2: Standard layer structure of CIGS solar cells, layers not at scale.

The Mo layer is the rear contact and the positive electrode. The choice for this metal lies on the production of an ohmic-type contact with the absorber, good adhesion to the SLG substrate, low sheet resistivity, and thermal and Se atmosphere resistance during the CIGS deposition, most of these properties are mainly due to the production of a thin layer of the mechanically stable $MoSe_2$ at the Mo/CIGS [43, 44]. However, the lack of higher optical reflectivity values at the Mo rear contact forces researchers worldwide to implement strategies to overcame this limitation in ultra-thin CIGS solar cells, as will be referred in section 1.3. Furthermore, Mo is permeable to Na allowing for a sufficient Na diffusion from the SLG into the CIGS [45, 46].

Regarding the CIGS absorber, in standard devices it has thickness values about $2-3\,\mu$m. CIGS is a chalcopyrite-type I-III-VI_2 compound with a tetragonal structure, Figure 1.3 a). The III element consists of a ration between In and Ga, [Ga]/([Ga] + [In]) (GGI), from $CuInSe_2$ to $CuGaSe_2$, repectively. The GGI is known to influence the CIGS conduction band minimum (CBM) [29] and therefore vary the bandgap, allowing to adjust the light absorption to the solar spectrum. Furthermore, recent high-efficient solar cells deposit the CIGS layer by co-evaporation with a three-stage process [39, 47], that typically vary the GGI composition in-depth, specifically with a high concentration of Ga at the rear contact, decreasing to a minimum value and followed by a small increase of the Ga concentration at the CIGS/CdS interface [34]. The Ga concentration grading towards the Mo rear contact creates a quasi-electric field that repeals the minority charge carriers (electrons) towards the p-n junction interface, improving the charge carriers collection [48]. Another property of CIGS is its direct bandgap transition and very high optical absorption ($\approx 10^5\,\mathrm{cm}^{-1}$) that allows for the low absorber thickness values mentioned above [49].

The p-type nature of the CIGS material is governed by its the defect nature, specifically defined by the Cu vacancies (V_{Cu}) due the very shallow level of 30 meV above the valence band and low formation energy [50]. Thus, the normal designation of a self-doped material. Another native defect-type affecting the solar cell performance are the antisite defects, i.e. in A_B the atom A is on the site of atom B in the AB compound [51]. Otherwise, the CIGS surface is reported to be Cu-poor with a wider bandgap than the bulk [31, 52, 53]. An example of a Cu-poor phase at the surface is presented in Figure 1.3 with the $CuIn_5Se_8$ compound and is normally referred to as ordered vacancy compound (OVC) or ordered defect compound (ODC). Further properties and impact in the solar cell performance will be discussed in Results and Discussion chapter.

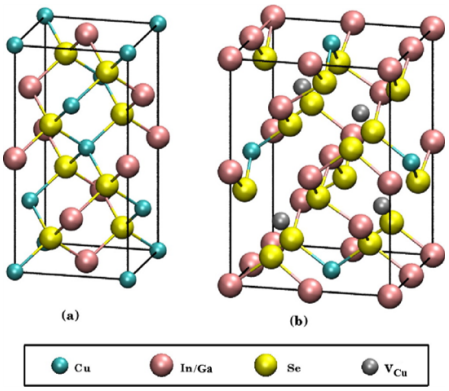

Figure 1.3: Crystal structure of the CIGS absorber (a) and chalcopyrite polytype of $CuIn_5Se_8$ ordered vacancy compound (b). Adapted from [54].

The n-type CdS buffer layer, typically deposited by CBD, completes the p-n junction and creates the necessary built-in electric field. CdS is a semiconductor with a bandgap of 2.4 eV which promote a suitable band alignment at the CIGS/CdS interface and lattice match with CIGS [27, 55]. The window layer is composed by a zinc oxide bi-layer. Near the CdS is deposited an intrinsic ZnO (i:ZnO) to prevent possible shunts, that degrade the cell performance by providing alternative paths to charge current, due to its high resistivity. Towards the front contact this zinc oxide layer is typically doped with aluminium, ZnO:Al (AZO), due to its high conductivity coupled with high transparency allowing for an effective charge collection [55]. Finally, it is normally deposited a Ni/Al/Ni grid layer as a front contact and connection to the external circuit. The presence of Ni is justified by the encapsulation of Al to prevent it to react with both the AZO window layer and the atmosphere [56].

1.3 Ultra-Thin CIGS Solar Cells

A research trend of the recent years is the fabrication of ultra-thin CIGS absorber solar cells. The fabrication costs, environmental and performance advantages were already mentioned early in section 1.2. Nonetheless, some performance limitations hinder the full potential of ultra-thin devices. It was referred also the importance of rear interface recombination and the necessity to enhance the light absorption. The first may be addressed with passivation techniques, while the latter may be tackled with modifications both at the rear and front contacts.

1.3.1 Losses Mitigation Strategies

The passivation strategy of interfaces was pioneered by Green *et al.* and first implemented in silicon solar cells [57, 58]. Latter this technology was transferred to thin-film devices, namely Cu_2ZnSnS_4 [59], CdTe [60], GaAs [61], and CIGS [62–64].

CIGS rear interface passivation consists in the deposition of a dielectric layer between the Mo rear contact and the CIGS absorber. It has essentially 3 benefits, namely i) field-effect passivation; ii) chemical passivation; and iii) enhanced rear reflection. The field-effect benefit is related to the fixed negative charges at the dielectric which creates an electric-field repelling the electrons from the recombinative rear contact towards the p-n junction [65–68]. The chemical benefit refers to the low defect density at the dielectric/CIGS interface [65, 67]. Finally, most dielectrics have higher optical reflection values compared with the Mo and therefore increase the the optical reflection at the rear contact for wavelength values in the visible–near infra-red (IR) range [69, 70].

Several rear passivation designs were reported in the literature, which include as an example the patterning with nanoparticles [69], electron-beam lithography to produce point

contact structures [64, 71] and optical direct write laser (DWL) lithography to produce rear line contacts [72, 73].

Regarding the light absorption losses in ultra-thin CIGS solar cell devices, the research community reported developments in light trapping schemes with nanoparticles at the rear contact [74, 75], rear contact reflectors [76, 77], and, recently, the incorporation of metal layers between the Mo rear contact and the passivating dielectric [73, 78] to further enhance the rear reflection of standard Mo rear contacts.

The experimental work performed within this thesis, reduced to a small section due to the pandemic situation restrictions at the time of thesis work, focus on the last referred metal/dielectric stack at the rear contact fabricated with optical DWL lithography, to mitigate some limitations of ultra-thin devices, which are supported by the performed electrical simulations. The metal/dielectric stack benefits from high optical reflection values provided by the metallic layer and from the passivating properties of the dielectric layer. Therefore, this experimental study aims to provide an industrial-friendly process through lift-off to fabricate the desired rear structure.

1.4 Modelling

Electrical device simulation of complete solar cells always helped in the comprehension of the mechanisms limiting the performance of such devices. Several studies entirely based on numerical simulations [79–81] or at least including complementary simulations [10, 82–84] were published. The simplest tools for electrical simulation include 1D software. Solar Cell Capacitor Simulator 1D simulation (SCAPS-1D) software [85] is widely used for thin-film solar cells and it was originally designed for CIGS and CdTe thin-film technologies.

The best practice of simulation includes the change of a few parameters, to clearly discriminate the corresponding effects. So, an important requirement is to set a baseline, i.e. a base model that describes the performance and results of the current high-efficiency solar cells. The last updated and realistic baseline, with various parameters verified experimentally, was established in 2011 by Pettersson *et al.* [15]. Following the even older and widely used baseline from Gloeckler *et al.* in 2003 [16].

Since 2011, many advances occurred in CIGS thin-film technology that boosted the performance of solar cells. The power conversion efficiency enhanced from 20.3 % [17] to the current world record laboratory cell of 23.35 % [13]. This improvement in the solar cell performance is mainly due to the recent development of a PDT with heavy alkali fluorides, such as KF [37], RbF [39] and CsF [40]. Furthermore, the effects of PDT that benefits the performance of the solar cells are not included in the Pettersson's baseline model, which is the last relevant and experimentally verified baseline and whom power conversion efficiency is 17 %. Some authors study several parameters of CIGS solar cells with rather idealistic models [86, 87]. On the other hand, recent studies still base their simulations and conclusions with old baseline models [79, 88].

The main objective of this work is to develop an updated and realistic electrical baseline model that tackle the recent PDT developments in CIGS technology. This model builds upon data from the literature and own experimental results and measurements. Additionally to the beneficial effects of PDT, it includes other experimental-based CIGS features and contributions from an optical simulation software, 3D Finite-Difference Time-Domain (FDTD) within the Lumerical package [89], to take into account with the optical component present in SCAPS-1D, namely rear and front contact reflection.

Furthermore, the baseline model for high-efficiency solar cells is tested for ultra-thin devices. The results obtained provide a baseline set for ultra-thin CIGS solar cells as well. Moreover, a comparison with experimental results proves its reliability.

2 | Materials and Methods

This study is mainly divided into electrical simulations with SCAPS-1D and a smaller experimental section with the implementation of solutions to mitigate some ultra-thin solar cells limitations. So, the methodology used will be described together with the fabrication and characterisation techniques.

2.1 Electrical Simulations SCAPS-1D

The one-dimensional Solar cell Capacitance Simulator (SCAPS-1D) software developed at ELIS, University of Gent, is used to carry out the electrical simulations of CIGS thin-film solar cells [85]. SCAPS-1D was originally designed for CdTe and CIGS polycrystalline thin-film technologies and it is widely used in the PV community for thin-film devices. This numerical simulation software obtain the cell behaviour by solving the following semiconductors equations: the one-dimensional Poisson equation which relates the charge with the electrostatic potential Φ, electrons and holes continuity equations which assures the charge conservation, and drift-diffusion equations responsible for the driven forces of the electrical current [85, 90, 91]. The Poisson is presented as follows, in equation 2.1.

$$\frac{d^2}{dx^2}\Phi = \frac{q}{\epsilon}\left(n - p + N_{\mathrm{A}}^{-} - N_{\mathrm{D}}^{+}\right) \tag{2.1}$$

Where q is electronic charge, ϵ is the dielectric permittivity of the semiconductor, n and p are electrons and holes concentration, respectively, and N_{A}^{-} and N_{D}^{+} are the ionised acceptor and donor defects, respectively. Equation 2.2 presents the electrons/holes continuity equations, respectively.

$$\frac{d}{dx}J_{\mathrm{n/p}} = \pm q\frac{\partial(n/p)}{\partial t} \pm q\,(G - R) \tag{2.2}$$

Whereas $J_{\mathrm{n}}/J_{\mathrm{p}}$ stand for the electron and hole current density, respectively, G is the generation rate, and R is recombination rate. Finally, the drift-diffusion equation 2.3 for electrons/-holes are presented below.

$$J_{\mathrm{n/p}} = -q(n/p)\mu_{\mathrm{e/h}}\frac{d}{dx}\Phi \pm qD_{\mathrm{e/h}}\frac{d}{dx}(n/p) \tag{2.3}$$

Whereas $\mu_{\mathrm{e}}/\mu_{\mathrm{h}}$ represent the mobility of electrons and holes, respectively, and $D_{\mathrm{e}}/D_{\mathrm{h}}$ are the diffusion coefficient for electrons and holes, respectively.

In the first results section of this study, the baseline model for high-efficiency devices is set. One of the major objectives of this study is to update the older baseline models with the recent advances in the CIGS technology, namely the PDT technique. Additionally, other experimentally-based material and high-efficiency solar cell characteristics are implemented, as it will be demonstrated in the following chapter 3.

To obtain a set of baseline parameters that model high-efficiency devices, the previous well-debated baseline model from Pettersson *et al* [15] is used as a starting point, followed by electrical and optical optimisations based on the literature and experimental results. The final model is compared with the 22.6 % record cell from Center for Solar Energy and Hydrogen Research Baden-Württemberg (ZSW) [39]. Note that the baseline model is not compared with the most recent record cells as they have additional steps of sulfurisation [13, 40] and their properties are not as well characterised as in the record solar cells from ZSW.

It is important to refer how some bulk parameters of all layers in the simulation were obtained, in table A.1 in annex with all the parameters of the first initial model and in equations 2.4 to 2.6, also present in [15]. The remaining parameters are discussed throughout the

next chapter 3. So, the density of states at the conduction band minimum (N_c) and at valence band maximum (N_v) are present in equation 2.4 [15, 20] and are dependent of the effective electron (m_e^*) and hole (m_h^*) effective masses in the respective layers [20, 92, 93].

$$N_{c/v} = 2\left(\frac{2\pi m_{e/h}^* k_B T}{h^2}\right)^{\frac{3}{2}} \tag{2.4}$$

Whereas k_B is Boltzmann constant, T the temperature and h stands for the Planck constant.

Additionally, the electron (v_{th}^e) and hole (v_{th}^h) thermal velocities also are dependent of the respective effective masses, as shown and calculated from equation 2.5.

$$v_{th}^{e/h} = \sqrt{\frac{k_B T}{m_{e/h}^*}} \tag{2.5}$$

Finally, μ_e and μ_h are defined with relation of the effectives masses in equation 2.6, whereas in the CIGS layer it would provide an electron diffusion length of $\approx 1\,\mu$m [15].

$$\frac{\mu_h}{\mu_e} \approx \frac{m_e^*}{m_h^*} \tag{2.6}$$

The next step includes the application of the baseline achieved for high-efficiency devices to ultra-thin solar cells. The modelling of ultra-thin devices is performed also with experimental results and measurements from reported devices within the group [94]. So, it is modelled 4 devices with all combinations of PDT treatment and/or rear interface passivation and compared with the respective experimental results.

Finally, some limitations of ultra-thin solar cells are studied. It was carried out simulations to address the impact of rear and front contact optical reflection. The rear optical reflection is increased to simulate a rear reflector, while the front optical reflection is studied on the cell model with and without the anti-reflective coating (ARC) layer. Additionally, the impact on the cell performance of the rear contact recombination velocity and bulk defect density are assessed through the variation of the respective values.

2.2 Experimental Rear Passivation Structure

This section provides an overview on fabrication steps required to achieve the final rear nanostructure and the associated characterisation techniques. The objective is to obtain a rear structure as in the final step at Figure 2.2 below. By achieving this structure, the subsequent solar cell would benefit from the passivation effect [65, 71, 72] and simultaneously benefit from the higher rear reflection from the metal layer compared with the standard Mo rear contact [73, 78, 95]. Note that a more extensive study on the electrical and optical properties of a similar structure is performed elsewhere [95]. Instead, this study aims to provide a simpler industrial-friendly process to achieve that similar rear structure and assess the respective feasibility, with just one lithography step compared to the three steps necessary in the referred study. The single lithography step to obtain the desired rear contact requires a calibration on the photoresist (PR) exposure conditions and subsequent development step, in order to have the proper structures dimension [95, 96].

2.2.1 Calibration

This study proposes a solution to obtain the final rear structure, see Figure 2.2, that requires a lift-off process. Furthermore, it was used a bi-layer of two different photoresists: LOR 5B, based on polydimethylglutarimide [97]; and AZ1505 [98]. It will be now specifically described the steps necessary for the calibration process, possible to verify at steps i), a), and b) in Figure 2.2.

The calibration procedure begins with a direct current sputtered 350 nm of Mo coated SLG substrates received from our partner Uppsala University. Then, the substrates are cleaned in a set of 3 different ultra-sound baths: 10 minutes in acetone, followed by another 10 minutes in isopropanol, 5 minutes in water, and blown with nitrogen to dry the substrate. At this moment, the calibration process itself starts with the dehydration of the substrate in the Vapor Prime Oven YES-310TA at 150 ºC for 15 minutes (LOR 5B do not require HMDS - hexamethyldisilizane to improve adhesion [97]). The LOR 5B was deposited on the dehydrated substrate by spin coating in the Suss Microtec Gamma automated Cluster equipment with in-house International Iberian Nanotechnology Laboratory (INL) recipe to obtain 500 nm of thickness [97]. Rapidly, the subsequent deposition by spin coating of the PR AZ1505 is performed in other equal Suss Microtec Gamma Cluster equipment optimised for 600 nm thickness. Finally, the samples are prepared for the lithography step, which is achieved with the 405 nm laser exposure in the Heidelberg DWL2000 equipment. The designed mask in Figure 2.1 is exposed on the upper PR AZ1505, for different laser Focus (F) and Intensity (I) values as described in the next paragraph. This mask encompasses a features pitch, i.e. distance between two consecutive points, of 2.8 μm and an exposed line width of 1.2, 1.4, and 1.6 μm, however only the 1.6 μm line width results will be presented as explained below. The development of the exposed samples are performed again in the Suss Microtec Gamma Cluster with the AK 400K developer 1:4 with deionised water, which is a KOH-based developer. The development times were also varied. Note that this developer acts on both photoresists, having the bottom PR LOR 5B a higher dissolution rate compared with the upper PR AZ1505, thus producing the desired undercut.

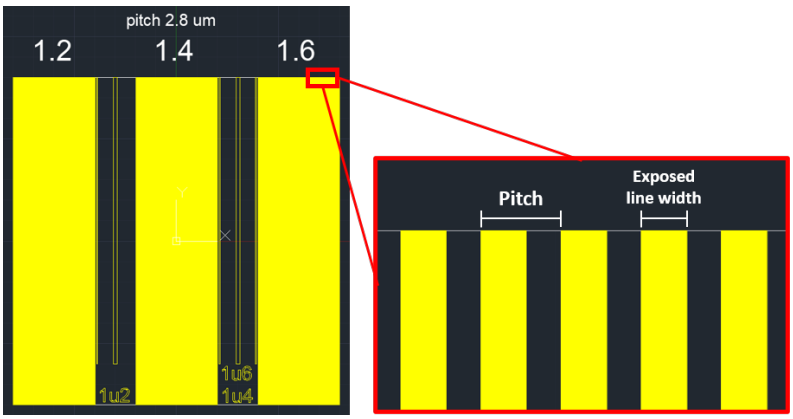

Figure 2.1: Mask used in the calibration process. Pitch of 2.8 μm and exposure line width of 1.2, 1.4, and 1.6 μm. Note that in the results chapter it is only presented the 1.6 μm line width results.

The aim of this calibration is to achieve a proper undercut below the upper resist, to allow the lift-off of the dielectric, together with a final contact line width of about 500 to 700 nm [95], i.e. the width of the remaining bottom resist. So, It was varied the DWL exposure conditions, F and I: -20, -40; and 40 %, 50 %, 60 %, respectively. Moreover, the development time after DWL exposure was varied between 40 s, 45 s, and 50 s. The exposure conditions values were defined according to the standard calibrated values (F -20 and I 50 %) by the equipment responsible, while the development time is based on previous experience and results [99]. Note that in this calibration, it was also varied the width of the exposed lines: 1.2; 1.4; 1.6 μm, whose CAD design was personalised and is present in Figure 2.1. It was observed (not shown here) and is reported that the undercut increases with the line width [99]. However, it is only presented the results for 1.6 μm exposed line width, as the rear reflection benefit increases with the coverage area of the metal layer which is associated with this line width.

The developed samples from this calibration process were briefly analysed on the Nikon

Eclipse L200N optical microscope. The experience gained in several repetitions of the calibration steps allowed to roughly discriminate whether a set of conditions produced the desired undercut based on the optical microscope images. The conditions which provide the potential best results were analysed through cross-section scanning electron microscopy (SEM) images in the NovaNanoSEM 650 equipment, with further details below in sub-section 2.2.2.

2.2.2 Fabrication and Characterisation

The fabrication steps of this study, whose results are shown in section 3.4, use a lift-off process that were adjusted to a posterior incorporation in solar cells employing a reflective back contact (RBC) [77]. The rear contact of RBC solar cells are composed by the AZO/Ag/AZO/In_2O_3:Sn (ITO) stack deposited on a SLG substrate, where the metal layer is already present. However, this study tests the suggested rear structure on Mo coated SLG substrates used in conventional CIGS solar cells, so this work would start with the deposition of the 2nd Mo on ITO of real RBC cells, Figure 2.2. An alternative procedure to be used directly in the conventional substrate is also presented in Figure 2.2 that was already used in the preliminarily test of the lift-off of the alumina deposited by atomic layer deposition (ALD) referred in sub-section 3.4.2 of chapter 3 and in Figure B.8 in annex B. The advantage of this alternative procedure, which benefits from the different deposition conformabilities, is the even simpler processes without the Mo deposition and respective etching, however due to the not working DWL equipment at that time, a successful complete alternative rear structure was not yet achieved.

It will be now described the experimental process steps of this study, also present in Figure 2.2. The rear contact substrate fabrication begins at our partner Uppsala University with the 350 nm Mo coated SLG substrates, as already referred in the previous sub-section 2.2.1. Furthermore, the steps i), 2) and 3) of Figure 2.2 were also described in the previous sub-section 2.2.1. However, the rear fabrication includes the consecutive deposition of sputtered 10 nm of Aluminium on the Kenosistec - UHV confocal sputtering equipment and a second sputtered 30 nm of Mo in a home made sputtering tool before the lithography step and PR deposition. With the desired PR profile in Figure 2.2 step 3), the Mo is etched through reactive-ion etching (RIE) in the SPTS ICP system. This etching step is important due to high Mo parasitic light absorption of the incoming light that would be reflected by the high reflective Al. The Figure 2.2 step 5) refers to the Al_2O_3 layer deposition by sputtering at the Timaris FTM equipment with 18 nm of thickness. The mentioned dielectric passivates the rear contact and, simultaneously, encapsulates the metal layers, preventing the inter-diffusion of elements between CIGS and the metal during the harsh CIGS growth conditions (selenium atmosphere at $\approx 550\,^{o}$C) [78]. The final step consists on the lift-off of the Al_2O_3 dielectric. So, it was placed the samples in ultra-sound bath, to improve lift-off efficiency, heated to 60 ^{o}C with the mr-500 REM remover during 30 minutes. To avoid water from contact with the remover the glass container were covered with parafilm or a plastic cover. The remover bath was followed by an ultra-sound bath in isopropanol for 5 minutes, water rinse and dried with a nitrogen blown.

The samples were characterised in the NovaNanoSEM 650 SEM equipment, through cross-section images at 5 kV and top-view images at 10 kV. The respective cross-section images were taken after the Nikon Eclipse L200N optical microscope sample observation in calibration process and on selected conditions to verify to produced PR undercut and uniformity. Furthermore, cross-section and top-view images were obtained after the etching step and after the lift-off process to characterise the substrate and assess the effectiveness of the etch and lift-off, respectively. Note the importance of the optical microscope analysis which provides a technique where the information is rapidly obtained, specially in the calibration repetitions with several parameter conditions. The referred microscope analysis allows to save time in other more time-consuming techniques, such as the SEM analysis, by the appropriate selection of the conditions to be analysed in the calibration process.

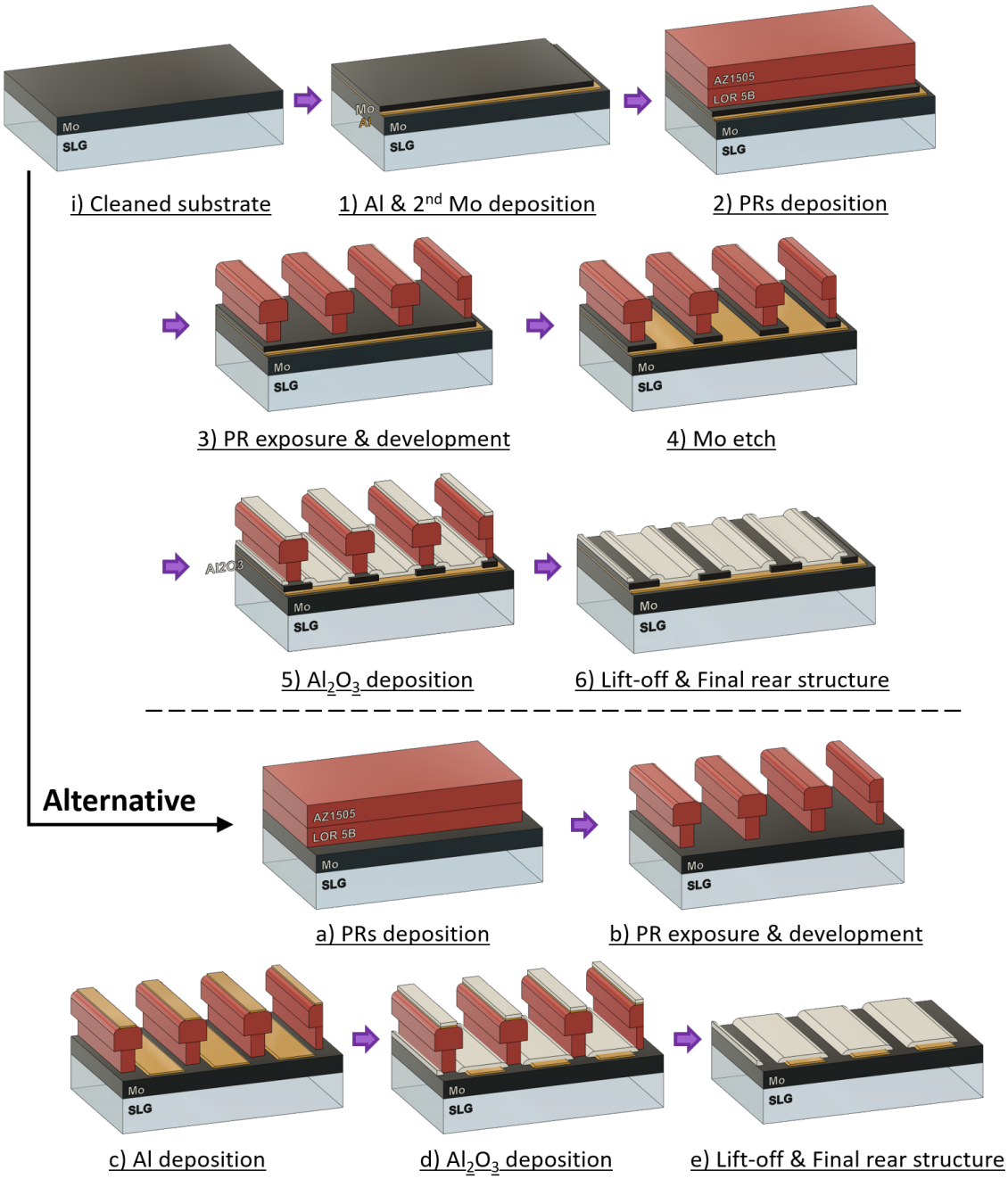

Figure 2.2: Fabrication steps to obtain the desired rear structure: adjusted to an RBC solar cell [77], which already has the metal layer; and the alternative on the conventional Mo coated SLG. Layers thicknesses: Al - 10 nm; 2nd Mo - 30 nm; LOR 5B - 500 nm; AZ1505 - 600 nm; Al_2O_3 - 18 nm. Not at scale. Note the more directional Al deposition and more conformal Al_2O_3 deposition in the alternative path.

The Bruker Icon atomic force microscopy (AFM) equipment was used to provide additional information on the substrate, on tapping mode at 1 Hz scanning rate. Since the AFM analysis has a high precision on z-axis, it was possible to confirm the encapsulation of the metal layer by the dielectric with the respective approximate thickness value.

3 | Results and Discussion

In this chapter, it is presented and discussed the results obtained for electrical simulations and experimental rear nanostructure fabrication.

Section 3.1 focuses on the development of an updated and realistic baseline model for high-efficiency devices, with experimental-based CIGS characteristics and the recent advances with PDT in the CIGS technology. Additionally, this baseline is applied to ultra-thin CIGS solar cells in section 3.2, which paves the way for an ultra-thin solar cell baseline model. Furthermore, section 3.3 refers to some limitations regarding ultra-thin devices.

Finally, it is fabricated a rear nanostructure with industrial-friendly processes that simultaneously increase light absorption and reduces rear contact recombination, section 3.4.

3.1 Baseline Model: to High-Efficiency Devices

The recent improvements in the CIGS solar cells performance due to the PDT process did not reflect a significant and realistic advance in the older baseline models for electrical simulation with SCAPS-1D. Furthermore, the previous well debated and experimentally-based baseline is the model from Pettersson *et al.* [15] from 2011. So, the initial step in the path to achieving an updated and experimentally-based baseline model of high-efficiency devices is to replicate his model and results, together with a comprehensive analysis of this initial model.

3.1.1 Baseline Initial Set

To replicate the Pettersson's model, the CIGS solar cell is composed of 5 layers, Figure 3.1: CIGS; surface defect layer (SDL); CdS; i:ZnO; and AZO.

Some simulation studies do not present the SDL (also referred to as OVC or ODC) layer [10, 82] or only present one ZnO layer [16, 88]. Otherwise, many other studies employ these layers [100–103]. However, both situations with SDL and a ZnO bi-layer are more related to experimental evidence and real devices, respectively. The SDL is often associated with a Cu-poor region at the surface of CIGS based solar cells, with the corresponding widening of the bandgap [31, 52, 79, 103–105]. Moreover, to assess the impact in the solar cell performance it is compared, below, the results with and without the SDL layer. Whereas the intrinsic and doped ZnO have different doping levels and light absorption properties, thus the importance of discriminating between these two layers.

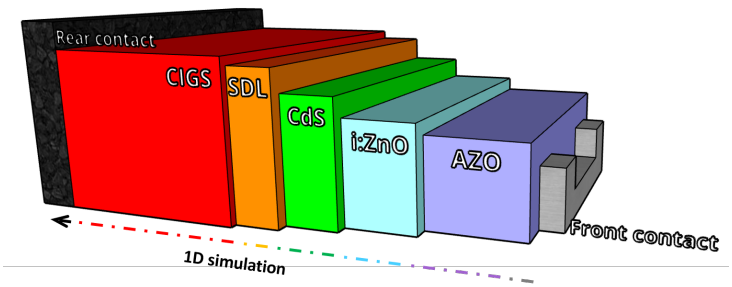

Figure 3.1: Scheme of the layers used in the SCAPS-1D model, thicknesses not at scale. Initial layers thickness: CIGS 1.8 µm; SDL 15 nm; CdS 50 nm; i:ZnO 100 nm; AZO 300 nm.

The results of this initial model are presented in table 3.1. The initial model has the parameter values as in the Pettersson model, except for some optical properties, namely front reflection and the absorption coefficients of all layers that are taken from [32, 106].

One concludes that there is a good agreement between both results, Pettersson's model and CIGS initial model, presented in table 3.1. The discrepancies in the J_{sc} value can be attributed to the different optical properties. So, this work updated the optical constants for each layer: CIGS is based on [32], according to its GGI composition, and the CdS, i:ZnO and AZO layers are based on [106]. It is important to note that the absorption coefficient takes into account the infrared light absorption due to free carriers in the AZO layer. Additionally, the front reflection was set to 0 %, which is an ideal situation, whereas the Pettersson model used its own experimental data. Moreover, the FF value was adjusted with a R_s of 0.4 $\Omega \cdot cm^2$, characteristic of solar cells with good performance [17, 47, 107]. Pettersson's model in [15] refers to the R_s fitting from measured J-V curves. The efficiency numbers in Table 3.1 are typical of non-anti reflection and non-PDT devices [46, 108] considering that the common ARC normally increases the absolute cell efficiency by 1.0 – 1.2 % [109].

Table 3.1: Comparison of the simulation results obtained with Pettersson's model (which has the SDL layer) and the initial model of this study. Pettersson's model η was calculated from the respective figures of merit. Additional SDL test with the result for the initial model without the SDL layer

CIGS model	V_{oc} (mV)	J_{sc} (mA $\cdot$ cm^{-2})	FF (%)	η (%)
Pettersson's model [15]	645	34.5	76.4	17.0
1a - CIGS initial model	646	34.0	76.7	16.9
1b - CIGS initial model (without SDL)	593	34.4	76.9	15.7

It is important to mention the role of the SDL layer. Within the simulation, this layer has most of the CIGS properties, except for the electron/hole mobility and bandgap [15]. Later, a few parameters will be adjusted according to the CIGS surface values due to their grading nature.

To discriminate the SDL layer effect on the solar cell performance, the results also in table 3.1 compare the respective performance with and without this SDL layer. It is possible to observe that there is a significant improvement in the V_{oc} with the SDL. The explanation may be attributed to the reduction of the CIGS/CdS interface recombination. Figure B.1 confirms that, with SDL, the interface recombination is lower than bulk recombination, also in [15]. Otherwise, without SDL the interface recombination is higher than bulk recombination. Additionally, the valence band offset (VBO) intrinsic of this layer acts as a hole barrier, decreasing the hole density at the interface, consequently decreasing interface recombination probability [31, 110–112].

This comparison indicates a good starting point of the initial model in agreement with the previous most relevant baseline model.

3.1.2 Electrical Parameters Optimisation

The initial model obtained previously will be optimised and some model parameters will be successively added and/or changed. So, the respective impact on the performance will be addressed. This sub-section optimises the electrical parameters and introduces the PDT effects.

Deep bulk defects

The first optimisation deals with deep bulk CIGS defects. Typically, old baseline models define one deep bulk defect that acts as a recombination centre [15, 16].

In this study, deep bulk CIGS defects are addressed with theoretically and experimentally found defects. Furthermore, the heavily cited study [50] calculated several native point defects in $CuInSe_2$ chalcopyrite semiconductor and compared the respective defect transition levels with available experimental data. The defects having a higher probability of occurrence due

to its formation energy are Cu vacancies (V_{Cu}), In on Cu (In_{Cu}) antisites, and Cu on In (Cu_{In}) antisites, excluding In vacancies (V_{In}). V_{In} is a triple acceptor defect, i.e. it has 3 acceptor transition levels with 3 different defect ionization states [51]. So, to keep the model as simple as possible, it contains only double defects. In_{Cu} antisite is a double donor defect with 2 donor levels at 0.25 eV and 0.34 eV below the energy level at conduction band minimum (E_c) and the Cu_{In} antisite is a double acceptor with 2 acceptor levels at 0.29 eV and 0.58 eV above the energy level at valence band maximum (E_v) [50, 113, 114]. Additionally, V_{Cu} is a shallow acceptor defect, which is addressed directly by SCAPS-1D with a parameter with the same name. This defect affects the net free carrier concentration as it is the most shallow defect (E_v + 0.03 eV).

Considering the defect density, the literature [50, 115, 116] refers to experimentally found density values around 10^{13} cm^{-3}, both for the double donor and double acceptor defects.

Moreover, there are not many reported experimental values for electron/hole cross-section (σ_e/σ_h) and, when available, they are rather small, about 10^{-24} – 10^{-22} cm^2 [117] and 10^{-18} – 10^{-17} cm^2 [115]. So, the σ_e/σ_h values of the respective bulk defects follow the work from Pettersson *et al.* [15] and consider the equation of the attractive capture cross-sections that associate electron/hole charge carriers with donor/acceptor defects, respectively [16].

Due to a few experimental information in defects capture cross-section, Figure B.2 in annexes demonstrate the impact of the σ_e and σ_h values variation for the double donor and double acceptor defects in the solar cell performance. This test is performed in the cell model with all the updated features in this section, so it is possible to address the respective impact on the baseline model for high-efficiency devices. One concludes that the electron capture cross-section heavily affects the J-V curve and respective Figures of Merit. The lower performance occurs for higher σ_e values due to the increased recombination probability into that defect. Otherwise, the hole capture cross-section value induces almost no change in the J-V curve. The explanation for the different behaviour between electrons and holes may be attributed to the recombination of the generated electrons minority carriers in the CIGS bulk, preventing its charge collection.

The solar cell model uses the deep double defects referred above. Additionally, Table 3.2 shows the effect of replacing the previous single donor defect by these double donor and double acceptor defects, referred to as native defects. However, the reported defects by Zhang *et al.* [50] refer to a single crystal material. So, due to the polycrystalline nature of CIGS in thin-film solar cells, it is important to take into account the grain boundary (GB) effect on solar cell performance [118, 119]. Several experimental studies in the literature report a band bending at grain boundaries that lower the solar cell performance [120–122] with barrier heights of about 100 meV. To encompass with the reported GB barrier height, GB interface defect densities of 2×10^{12} cm^{-2} [79, 118] within a defect level at 0.27 eV above E_v are required [118]. Therefore, considering a grain size of 2 µm, these GB defects are included in the SCAPS-1D model as a CIGS deep bulk defect, according to the interface/bulk defects relation in [118]. This relation is obtained by the ratio of the interface defect density (2×10^{12} cm^{-2}) to the grain size, resulting in the transposition of the GB interface defect to CIGS bulk GB defect (1×10^{16} cm^{-3}). So, in addition to the native defects, it is included GB defects at E_v + 0.27 eV, density of 1×10^{16} cm^{-3} and σ_e/σ_h of 10^{-15} cm^2, half acceptors and half donors [118]. Hence, there is a decoupling between native point defects from the grain interior and GB defects. Where in such 1D simulation, the effect of GB defects can be considered as being distributed along the CIGS bulk material. The effect of the addition of this GB defect on solar cell performance is present in table 3.2.

It is possible to see in table 3.2 that, by comparing the simulation results with the previous initial model and the native + GB defects, the V_{oc} is significantly lower in the latter case. The high V_{oc} of the initial model, representing the previous baseline model, indicates a low bulk recombination rate in this previous baseline, due to the low deep bulk defect density [15, 16]. Suggesting that with the native + GB defects, based on experimental evidence, the V_{oc} is limited by bulk recombination. Nonetheless, a good passivation of GB would lead to a significant gain

in solar cell performance, mainly in V_{oc} and FF.

Table 3.2: Adoption of native defects and addition of GB defect to the bulk CIGS and comparison with the simulation results for the initial model. *R_s here is set to 0 Ω.

CIGS model	V_{oc} (mV)	J_{sc} (mA · cm^{-2})	FF (%)	η (%)
1a	645	34.1	78.5	17.3*
2a - Native defects	687	34.6	81.3	19.3
2b - Native + GB defects	597	34.1	78.6	16.0

Bandgap grading

Another characteristic of high-efficiency devices is the CIGS bandgap grading due to the variation of GGI in depth from the Mo to the CdS buffer layer. The GGI is known to influence the CIGS CBM [29]. Until this point, the model tested had a linear grading, a high concentration of Ga at the back and a lower concentration at the superficial region of the CIGS, presented in Figure 3.2. However, bandgap double grading towards both Mo and CdS interfaces has been used in CIGS technology even before PDT [123], being associated with the 3-stage process for CIGS grown films, i.e. a high concentration of Ga at the back surface, that decreases until a minimum value (the notch), followed by a small increase of the Ga concentration at the front surface [34]. Generally, the advantages over linear grading include improved current density due to absorption in the notch, i.e. region with lower bandgap value, and high voltage as a result of larger bandgap in the SCR [124]. Moreover, Frisk *et al.* [124] report improvements in solar cells performance with double grading over linear grading. So, it will be incorporated a double grading scheme in the model, according to experimental high-efficiency solar cell devices from ZSW [82, 83] and to literature studies [31, 105, 124]. Figure 3.2 compares the linear grading of the initial model with the implemented bandgap double grading.

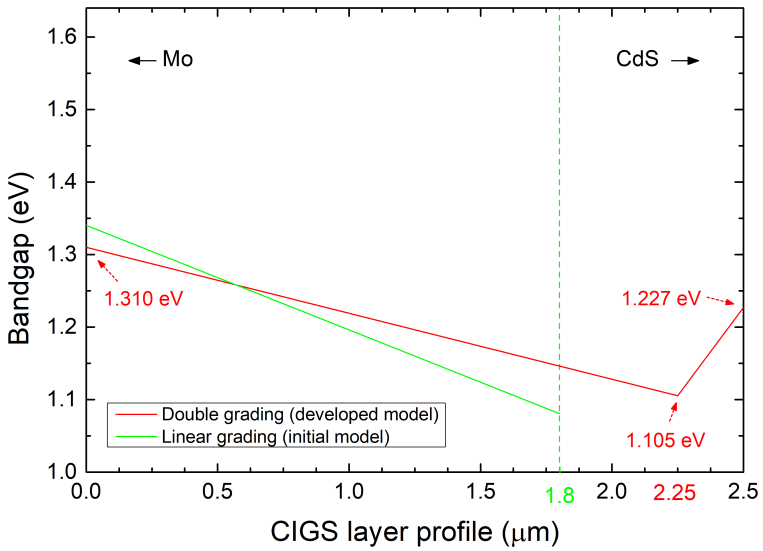

Figure 3.2: Bandgap gradings of the initial model (1a) and the incorporated double grading. The initial model has a CIGS layer thickness of 1.8 µm, while for the double grading model this absorber thickness is 2.5 µm separated into two Ga gradients.

It is important to note that with the incorporation of the double grading scheme, the CIGS

layer thickness increased from 1.8 µm of the initial model (representing the last relevant baseline model) to 2.5 µm, according to the last record solar cell from ZSW [39]. Consequently, the CIGS layer is separated into two layers, with the only difference being the bandgap and respective electro-affinity grading. The latter grading is to ensure a bandgap grading due to a variation in the CBM [29].

Additionally, the effect of the double grading on solar cell performance is presented in Table 3.3. The improvements observed in this Table 3.3 are in good agreement with results from literature [124, 125]. Mainly the V_{oc} is enhanced, which can be attributed to an overall higher bandgap and widening of the bandgap to the SCR in the double grading scheme. The V_{oc} is reported to increase with the bandgap in the SCR [30, 105]. Furthermore, this grading scheme will induce a quasi-electric field that will superimpose on the random movement of the carriers. Consequently, the electrons will be drifted to the p-n interface, pushing the electrons away from the highly recombinative back interface, allowing for a decrease in the recombination probability. The slight increase in J_{sc} is attributed to the increased CIGS thickness, as depicted from the respective EQE curves (not shown here).

Table 3.3: Comparison of results between the model with the incorporated bandgap double grading and the previous model with linear grading. The respective bandgap gradings are present in Figure 3.2

CIGS model	V_{oc} (mV)	J_{sc} (mA · cm^{-2})	FF (%)	η (%)
2b	597	34.1	78.6	16.0
3 - Double grading	623	34.4	79.3	17.0

Shallow acceptors

It was already referred above that V_{Cu} is a shallow acceptor defect. These defects heavily affect the net free carrier concentration and, in SCAPS-1D, define the respective doping of the layers.

Typically, the old baseline models define a constant shallow acceptor density [15, 16]. This study addresses this question with a more experimental-based approach. So, according to capacitance - voltage (C-V) measurements in the literature, the CIGS net free carrier concentration in solar cell devices varies with the distance from the CIGS/CdS interface [84, 107]. Moreover, the PDT process was shown to increase hole concentration [82, 84, 126] in the CIGS bulk. Additionally, it is added into the model compensating shallow donor defects with density of the same order of magnitude as the shallow acceptor defects, see Figure 3.3. These compensating defects may have origin in Se vacancies (V_{Se}) [50, 51].

Several PDT effects on CIGS devices are still highly debatable [127]. One of its effects concerns the n-type inversion at the CIGS surface due to the Cu-depletion and consequent diffusion of Cd during CdS deposition, that would occupy the V_{Cu} and form Cd_{Cu} antisite shallow donor defects [38, 53, 54, 84]. Hence, this model incorporates the PDT effect of increased net free carrier concentration [82, 84, 126] compared with the initial model. On the other hand, the two situations with and without n-type inversion at the CIGS surface are analysed. Therefore, the shallow acceptor density decreases from 5×10^{16} cm^{-3} at the Mo interface to 1.1×10^{16} cm^{-3} and 1×10^{14} cm^{-3} at the CdS interface, without and with n-type inversion, respectively. While the shallow donors' density is kept constant, 1×10^{16} cm^{-3}, through the CIGS layer. The grading of the shallow acceptor defects together with the compensating shallow donors are better visualised in Figure 3.3.

The results in Table 3.4 show that the increase in the net free carrier concentration led to the increase of the V_{oc} and FF, in both cases with and without n-type inversion. One concludes the CIGS doping could be limiting the solar cell performance, which is dominated by bulk recombination as referred above about the results in Table 3.2. The J_{sc} value remains unaltered

with the increased doping, which would reduce the SCR. However, the collection length comprises the SCR and also the diffusion length of the minority carriers (SCR + diffusion length). The explanation for the unchanged J_{sc} value may be attributed to the higher diffusion length (> 1 µm) compared the SCR (< 0.3 µm), so, variations in the SCR do not significantly affect the minority carriers collection probability, thus the J_{sc} value.

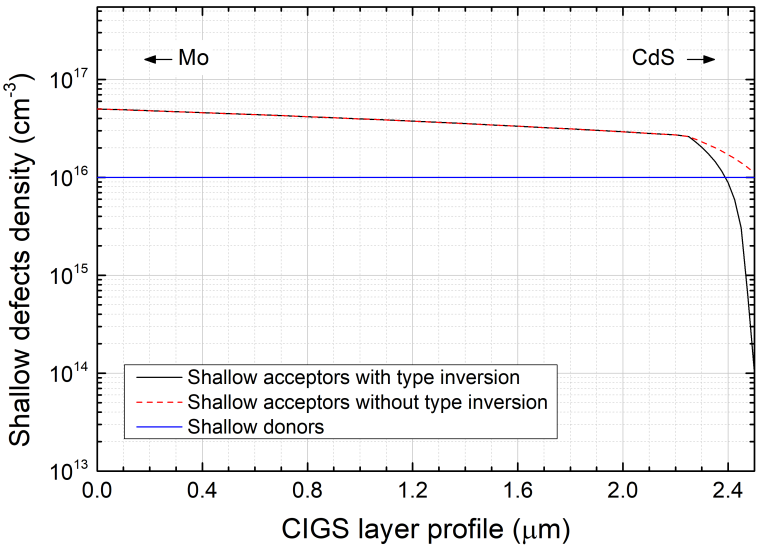

Figure 3.3: Shallow acceptors grading profile and indication of the shallow donor defect density incorporated in the CIGS layer. It is compared the cases with and without n-type inversion.

Table 3.4: Comparison of the results with and without n-type inversion at the CIGS surface, incorporated in the model 3. The respective shallow acceptor grading profiles are present in Figure 3.3. The shallow acceptor density values were increased, compared to the initial model, due to PDT

CIGS model	V_{oc} (mV)	J_{sc} (mA · cm^{-2})	FF (%)	η (%)
3	623	34.4	79.3	17.0
4a - Shallow acceptors update with type inversion	633	34.4	80.8	17.6
4b - Shallow acceptors update without type inversion	638	34.4	80.6	17.7

Another conclusion is that the debated n-type inversion at the CIGS surface due to PDT does not introduce significant improvements or differences in these simulation results. These differences will be even less substantial after the implementation of other PDT effects of this study. So, for the next steps to achieve a baseline model for high-efficiency devices, this study will keep the shallow acceptors grading profile without n-type inversion at the CIGS surface.

PDT - GB passivation

This study introduces some PDT effects that will update the old electrical baseline models with SCAPS-1D. The PDT is responsible for the latest developments and improvement in the power conversion efficiency in CIGS solar cell technology.

The PDT effects are generally divided in bulk and surface effects, according to modifications in the CIGS bulk or surface, respectively [127–129]. Firstly, the model developed in this

study will focus on bulk effects. So, experimental evidence of heavy alkali PDT points to GB passivation through alkali secondary phases reducing the density of charged defects and band bending at GB [128, 130], which is detrimental for the solar cell performance.

This model already includes the effect of GB band bending in the solar cell performance, as discussed above within deep bulk defects. Therefore, the GB passivation is achieved with the reduction of the GB defect density to $1\times10^{14}\,\mathrm{cm}^{-3}$ in SCAPS-1D, corresponding to an interface defect density of $2\times10^{10}\,\mathrm{cm}^{-2}$. This GB defect density represents a reduction in two orders of magnitude than the initial experimentally-based density of $2\times10^{12}\,\mathrm{cm}^{-2}$ for solar cells without PDT, in Table 3.2. Moreover, the referred defect density reduction is within the range of values studied in [118].

Considering the results in Table 3.5, it is possible to see that the V_{oc} is heavily enhanced, followed by some improvements in J_{sc} and FF. The improved performance mainly due to the V_{oc} is expected and follows the experimental results elsewhere [84, 126, 128, 130] in PDT treated solar cells. The GB passivation leads to a strong reduction of bulk recombination described by the Shockley-Read-Hall (SRH) model, which limited the solar cell performance. Furthermore, this PDT passivating effect represents an improvement in the power conversion efficiency of about 3 %, which is in agreement with the improvement observed from experimental record solar cells without PDT, $\approx 20\,\%$ [17], to PDT treated solar devices, $\approx 23\,\%$ [13]. Considering the J_{sc} value, the observed increase allows the conclusion that the minority carrier's diffusion length increased due to the reduction in bulk recombination, and the consequent increase of its collection probability. This conclusion is justified by the overall enhancement in the EQE curve for $\lambda > 600\,\mathrm{nm}$ (not shown here) with GB passivation.

Table 3.5: Solar cell results with the incorporation of GB passivation due to PDT and comparison with previous results (4b). The GB passivation was obtained through the reduction in the GB defect density. The results correspond to the case without n-type inversion

CIGS model	V_{oc} (mV)	J_{sc} ($\mathrm{mA\cdot cm^{-2}}$)	FF (%)	η (%)
4b	638	34.4	80.6	17.7
5 - GB passivation	735	35.4	81.0	21.1

PDT - interface effects

This section refers to the interface effects of PDT. So, the Solar Frontier study in [131] considers PDT mainly as a surface treatment. They reported reduced interface and SCR recombination with the PDT treatment. Moreover, within their simulations, it is introduced a defect density grading from the Mo contact to CdS, with lower density at CIGS/CdS interface. Therefore, this model incorporates a similar defect density variation through the GB defects, represented in Figure 3.4. This study already discussed another interface effect of PDT with the analysis of the n-type inversion at the CIGS surface, in the shallow acceptors' section.

The results in Table 3.6 show an increase in V_{oc} and a decrease in FF, which combined with the unchanged J_{sc} led to an improvement of only 0.1 % in power conversion efficiency. The performance improvement stems from a slight reduction of the recombination within and near the SCR .

Although there is almost no difference in efficiency in Table 3.6, the results with the GB grading profile lead to a model with Figures of Merit close to the high-efficiency record cell fabricated by ZSW. Therefore, the V_{oc} and FF values are similar to the results achieved by [39]. One concludes through the results with the bulk and interface PDT effects that the bulk effects had a much higher impact in the solar cell performance than the interface effects. Note that the analysis with the n-type inversion at the CIGS surface and increased net free carrier concentration, in the respective section, was considered as PDT interface and bulk effect, respectively.

The conclusion of the higher impact for the bulk PDT effects is in agreement with a recent study in [128].

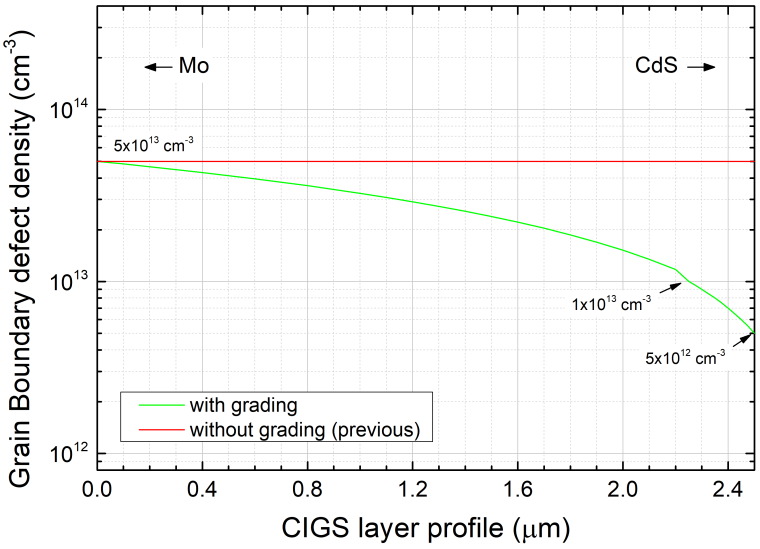

Figure 3.4: GB defect grading profile due to the effects of PDT at the CIGS/CdS interface. It is compared with the previous case without grading.

Table 3.6: Solar cell results with the incorporation of GB defect grading due to the effects of PDT at the interface and comparison with previous results of GB passivation at model 5. The grading profile is present in Figure 3.4

CIGS model	V_{oc} (mV)	J_{sc} (mA · cm^{-2})	FF (%)	η (%)
5	735	35.4	81.0	21.1
6 - Interface effect	744	35.4	80.3	21.2

Further optimisation

The study of the PDT effects was performed until the previous sub-section. So, the last electrical optimisations are related mainly with the band alignment and band bending at the CdS layer. Thus, it is first studied the influence of the Fermi level (E_F) pinning at the CIGS/CdS interface. The E_F pinning at the CIGS/CdS consists on the E_F fixed at a specific position or with a discrete number of possible positions at this interface due to the respective pinning at the interface defects level [132], Figure B.3 exemplifies this process.

The model of this study follows the initial model based on Pettersson *et al.* [15] to implement the E_F pinning. So, the CIGS/CdS interface has a donor-like type of defects with low capture cross-section values placed near the CBM energy level (E_c) to pin E_F, beyond the additional neutral interface defect, i.e. an idealised uncharged defect possible to implement in SCAPS-1D software that, in this case, accounts for the recombination at the interface.

Table 3.7 compares the previous model 6 with and without E_F pinning, i.e. with and without the donor-like interface defect, respectively. It is not possible to see any modification in the Figures of Merit, nor modifications in the solar cell band diagram. Another approach of achieving the same effect on the band diagram than the previous E_F pinning is through an n-type surface [133], which already was analysed previously. Both approaches did not produce any significant impact. So, considering that, this is a much-debated property [15, 133], this model

will continue without the donor-like interface defect. On the other hand, there is great variability in the CdS doping and compensating defect density [15, 16, 79, 82, 131, 133]. So, to obtain a smoother band bending at the CdS layer and following other simulation studies which have a high density of compensating CdS defects [16, 82, 131, 133], it will be increased the defect density at the CdS layer. The defect density value varied from 5×10^{16} cm^{-3} to 3×10^{17} cm^{-3}.

The CdS bulk trap density (N_t) increase results presented in Table 3.7 do not show a relevant impact in solar cell performance. Furthermore, the CdS band bending follows the trend in [80]. Finally, this model proceeds with increased CdS N_t.

The last electrical optimisation corresponds to the conduction band offset (CBO) at the CIGS/CdS and CdS/i:ZnO interfaces. The CBO is the difference between the respective E_c, by the same order, which in SCAPS-1D can be described as the difference between the respective electro-affinities (χ_a), e.g. the CBO at CIGS/CdS interface corresponds to $\chi_{a\ \mathrm{CIGS}} - \chi_{a\ \mathrm{CdS}}$.

As the initial model, in Table 3.1, the CIGS/CdS CBO of the current model is 0 eV, whereas the CdS/i:ZnO is -0.2 eV. However, several studies report a CBO between CIGS and CdS about 0.2 eV [80, 81, 134], which is among the values yielding higher efficiencies [80, 135]. Considering the CdS/i:ZnO CBO, an exhaustive simulation study in [80] identifies a CBO equal or higher than −0.1 eV attributed to high-efficiency devices. Therefore, this model will set the CBO at CIGS/CdS and CdS/i:ZnO interfaces as 0.2 eV and −0.1 eV, respectively. The band diagram near these interfaces is possible to see in Figure 3.5, before and after the last three modifications in this section.

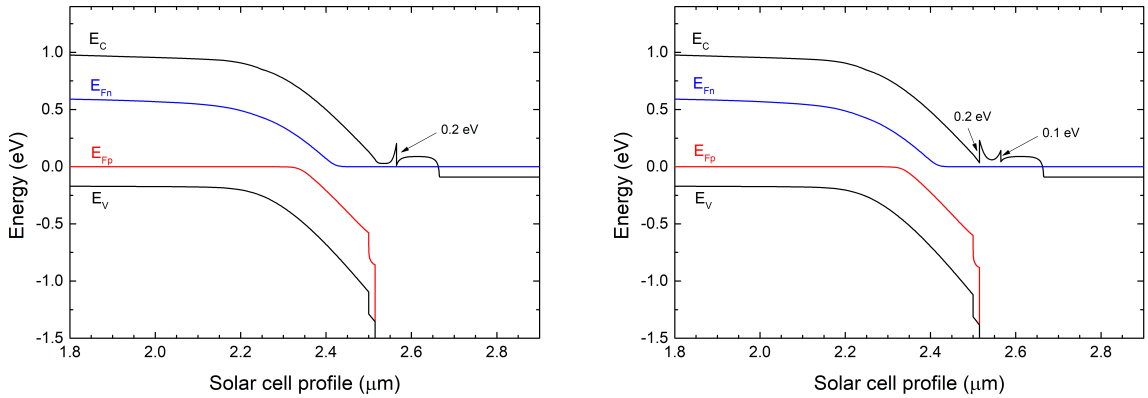

Figure 3.5: Band diagrams obtained for the solar cell model simulation: before changes in Further optimisation sub section (left); after CBO update (right).

Table 3.7: Results for the solar cell model with the sequential modification of the E_F pinning, CdS N_t increase and CBO update, compared with the previous result of the PDT interface effect at model 6

CIGS model	V_{oc} (mV)	J_{sc} (mA · cm^{-2})	FF (%)	η (%)
6	744	35.4	80.3	21.2
7a - E_F pinning	744	35.4	80.3	21.2
7b - CdS N_t increase	742	35.4	80.4	21.1
7c - CBO update	745	35.4	80.4	21.2

The solar cell performance with the CBO update, in Table 3.7, presents a slight increase in the V_{oc} and J_{sc}. The positive CBO at the CIGS/CdS interface is likely reducing the interface recombination [15], and the same is suggested for CdS/i:ZnO CBO ≥ −0.1 eV [80]. However, the reduced interface recombination effect is attenuated due to other characteristics of this model

with a similar impact: the presence of the SDL layer; and a reduced GB defect density near the CIGS/CdS interface. The V_{oc} and FF, in Table 3.7, are similar to the high-efficiency record solar cell by ZSW [39]. However, the J_{sc} still present lower values, explained with non-optimised solar cell layer thicknesses as well as rear and front reflection.

3.1.3 Optical Parameters Optimisation

This section optimises the optical parameters, namely the thickness of the different layers, rear and front reflection. Therefore, the objective is to obtain a solar cell efficiency and Figures of Merit values similar to the high-efficiency record device by ZSW [39].

It is important to refer that the absorption coefficient of all layers in the solar cell stack was updated in section 3.1.1. Hence, the CIGS optical constant is based on [32], according to its GGI composition, and the CdS, i:ZnO and AZO layers are based on [106].

Layers thickness

The final model of the previous section 3.1.2 achieved a J_{sc} of 35.4 mA $\cdot$ cm^{-2}. However, the ZSW devices reported different CdS, i:ZnO and AZO thickness compared with this model. Furthermore, the high-resistive ZnO layer is doped with Mg, thus referred to as $Zn_{1-x}Mg_xO$ (ZMO), reaching higher bandgap values.

The CdS layer thickness was adjusted according to the reported range thickness values [39] and EQE response in the 400 – 550 nm wavelength range. So, the CdS thickness is reduced from 50 to 21 nm. The impact in solar cell performance mainly refers to J_{sc}, as it is possible to observe in resume Table B.1 in annexes. Additionally, Figure 3.6 shows the evolution of the EQE curve with every step in the layers thickness optimisation.

Considering the ZnO window layers, they also have their thickness reduced. The high-resistive ZnO layer thickness decreased from 100 to 50 nm. While the AZO layer reduced its thickness from 300 to 150 nm. The values used in the model corresponds to the bottom of the range of values reported in [39], even for the CIGS layer thickness. Furthermore, the simulation of the ZMO layer is attained by adapting the bandgap to the Mg content [136]. Hence, the ZMO bandgap is set to 3.8 eV, considering a Mg content of 25 % ($x = 0.25$) [83, 136].

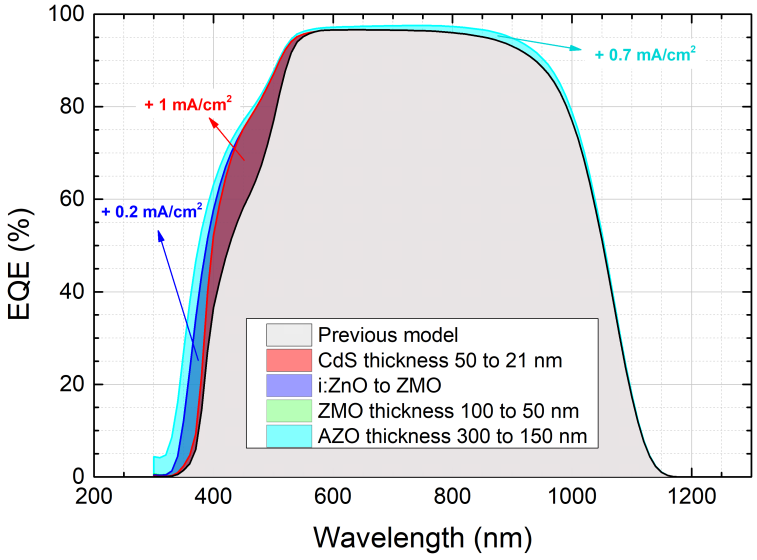

Figure 3.6: EQE response curve for the sequential modifications in the solar cell layers. Inset, it is presented the J_{sc} increase with each modification. It is noted that the ZMO thickness reduction does not affect the solar cell performance.

The J_{sc} improvement of 1 mA · cm^{-2} with the CdS thickness reduction, as already mentioned, is entirely associated with the solar cell light absorption in the 400 – 550 nm wavelength range, Figure 3.6. So, the light with shorter wavelength values that was absorbed in the thicker CdS, now reaches the CIGS absorber layer, contributing to the collected current. Furthermore, the CdS thickness reduction is considered as a PDT effect due to a more homogeneous CBD CdS growth at initial stages [13, 38, 40, 82]. Consequently, it is possible to benefit from the CdS thickness reduction without the often associated electrical losses [84]. Moreover, ZMO layer led to higher light absorption at the 300 – 400 nm wavelength range, possible to verify by the respective EQE curve in Figure 3.6. The respective enhancement observed in J_{sc} of 0.2 mA · cm^{-2} follows the higher bandgap compared with the intrinsic ZnO, which allow shorter wavelength values to pass through the window and buffer layers. Furthermore, the thickness reduction of the ZMO did not alter the EQE response and respective J_{sc}.

Finally, the AZO thickness reduction produces an overall improvement in the EQE curve, correspondent to the J_{sc} increase of 0.7 mA · cm^{-2}. Mainly, the light absorption is enhanced in the ultra-violet region due to the same reason mentioned for the CdS thickness reduction. Additionally, there is an improvement for wavelength values > 600 nm due to lower IR absorption by the free carriers present in the AZO material.

Rear and front reflection

Both rear and front reflection were set to 0 % from the initial model. The commercial software Lumerical [89], employing the 3D FDTD numerical method, assists the electrical SCAPS-1D simulations. So the Lumerical 3D optical simulations will provide the necessary optical reflection values.

It was simulated the reflection of the Mo substrate placed inside a medium with refractive index (n) of 3. This value corresponds to the mean value of the CIGS material with the same GGI composition at the rear contact in SCAPS-1D. The fixed refractive index is an approximation of the reality due to the grading nature of this index with wavelength (index variation of 2.8 – 3.2). However, simulating with this increased complexity would be time-consuming. Moreover, the refractive index at wavelength values near the visible-IR region is ≈ 3.

The rear optical reflection used in the SCAPS-1D simulations is present in Figure 3.7, together with the impact in the EQE curve. One concludes that there is an improvement in the light absorption for the IR region. The light in this region of the spectrum reaches the Mo rear contact, followed by some percentage of reflection to CIGS. Consequently, it travels through the CIGS absorber a second time, with a higher probability of being absorbed due to increased light travelling inside CIGS.

Finally, it will be considered the front reflection. The first step was to define a constant reflection value found in the literature [137], considering the reported reflection loss with a standard ARC with 130 nm of MgF_2. So, in Figure 3.7 is presented the EQE curve with 2.7 % front reflection with the respective impact in J_{sc}, resumed in Table B.1 in annexes. It is possible to observe a good fitting with the ZSW's EQE curve for the 22.6 % champion cell. However, the experimental curve presents some interference fringes due to the deposition of the buffer and window thin-films.

Hence, the next step tests the MgF_2 ARC layer and varies its thickness in the optical 3D simulations. The ARC thickness variation ranges from 80 to 150 nm, in Figure 3.8. It is important to note that the optical simulation considered the same thickness values used in SCAPS-1D for all layers. Additionally, it is considered the minimum bandgap with the respective minimum GGI ratio.

It is possible to see the effect of the interference fringes by the window and buffer layers. The shift that occurs in the interference peaks leads to different conclusions for the different ARC layers, concerning the fit to the ZSW result. Therefore, higher ARC thickness values provide a better fit at long wavelength values, while the opposite happens for lower thickness values

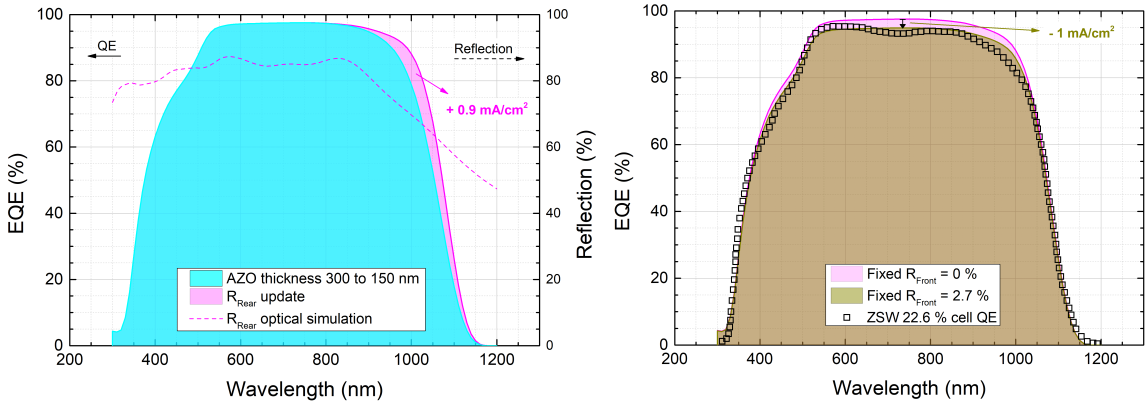

Figure 3.7: Left - EQE response curves comparing the rear optical reflection of 0 % with the presented Mo rear optical reflection (dashed line) obtained with the Lumerical 3D optical simulations. Right - EQE response varying the front reflection at fixed values and with optical simulated Mo rear optical reflection.

where it better fits the experimental EQE curve at shorter wavelength values. Nevertheless, the optimised ARC layer providing the highest J_{sc} value is represented in Figure 3.8, with 113 nm of thickness.

The final step introduces roughness in the CIGS layer with the optimised ARC layer of 113 nm, to provide for a better fit with the experimental curve. The CIGS roughness is obtained from an AFM measurement of a complete CIGS solar cell. Then, it is directly introduced in the optical simulation software at the CIGS layer, which is translated to the upper layers until the ARC. Figure 3.8 right compares the optimised ARC layer with and without the CIGS roughness.

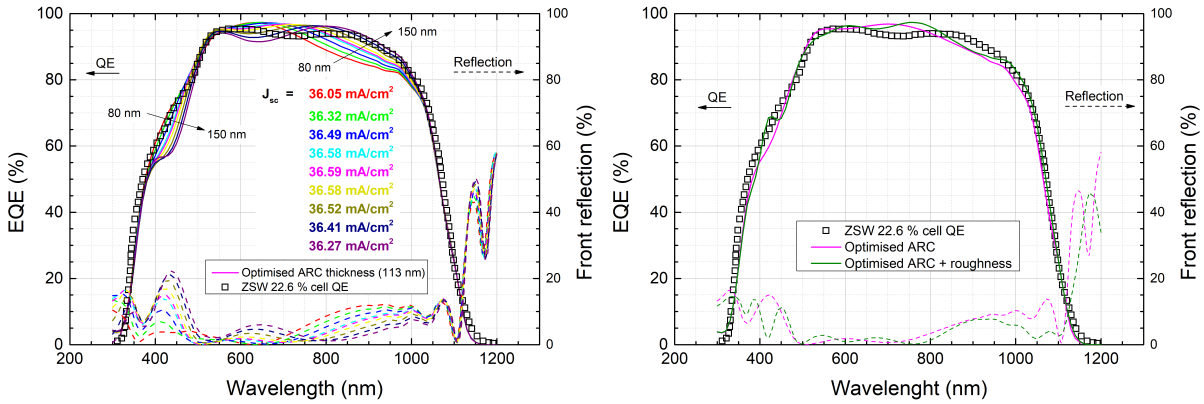

Figure 3.8: Left - ARC thickness test from 80 nm to 150 nm in steps of 10 nm, with EQE response curves and respective front reflection values. The optimised ARC thickness lead to a J_{sc} value of 36.59 mA $\cdot$ cm^{-2}. Note that the others Figures of Merit do not change significantly its values. The J_{sc} values inset follow the same thickness colour code. Right - EQE response curve with the optimised ARC and additional CIGS roughness, which is used in the baseline model for high-efficiency devices.

The fitting of the simulated EQE curve with the CIGS roughness to the ZSW experimental curve, in Figure 3.8, is optimised in the IR and ultra-violet (UV) region. However, the simulated roughness introduced additional interference peaks that still do not quite fit the experimental curve. Furthermore, there was an improvement of 0.4 mA $\cdot$ cm^{-2} in J_{sc} with this final step compared to the optimised previous ARC layer, concluded from the results in Figure 3.8 left

and Table 3.8.

The experimental roughness in high-efficient devices is rather variable and process-dependent, so the final model incorporates the ARC layer with the CIGS roughness, which is in reasonable agreement with the ZSW EQE curve.

Finally, it is important to correct the J_{sc} value to the grid shadow, considering that the J_{sc} obtained with SCAPS-1D simulation does not take into account the respective current losses. Moreover, this study compares the model results with record cell from ZSW, which lead to 1.7 % grid coverage [138]. So, 1.7 % of the current does not count for the J_{sc} in real devices. Table 3.8 presents the corrected J_{sc} value.

The baseline model to high-efficiency devices updated the 10-years old most relevant electrical baseline model with 17 % solar cell performance. It was optimised the electrical and optical parameters and introduced some reported PDT effects, which enhanced significantly the experimental CIGS solar cells performance in the last decade. Table 3.8 shows the Figures of Merit achieved with the baseline model of this study compared with experimental results from the ZSW record cell. Figure B.4 in annex B provides a visual comparison with J-V curves.

Table 3.8: Simulation results for the final updated model, i.e. baseline model to high-efficiency devices. The value in brackets represent the J_{sc} value considering the 1.7 % grid coverage in real devices. Additional comparison with the experimental data of the record cell from ZSW

CIGS model	V_{oc} (mV)	J_{sc} (mA · cm^{-2})	FF (%)	η (%)
Final Baseline model	747	37.0 (36.4)	80.3	22.2
ZSW [39] / difference (rel.)	741 / −0.8 %	37.8 / +2 %	80.6 / +0.4 %	22.6 / +2 %

3.2 Baseline Model: to Ultra-Thin Devices

This section follows the previous baseline model to high-efficiency devices by its application to ultra-thin CIGS solar cells. It will be modelled the in-house experimental ultra-thin solar cell devices to be reported in the literature [94]. Additionally, it is updated some model features compared to the model used in this referred study.

First, it is discussed the optical properties regarding mainly the rear and front reflection. And, second, the ultra-thin model adjusts the electrical parameters to better fit the experimental results. Finally, the model results are compared with the experimental Figures of Merit. Ultimately, this section provides a path to an ultra-thin solar cell baseline model .

3.2.1 Modelling

The 3D optical simulation software Lumerical [89] was again used to obtain the front reflection for the device layer structure, i.e. ultra-thin CIGS (∼ 500 nm)/CdS 50 nm/i:ZnO 150 nm/AZO 400 nm, without ARC. The front reflection is present in section 3.3 below, Figure 3.11, where it is discussed solar cells with and without the ARC layer. Moreover, the optical constants for all layers are the same as the constants used for the baseline model to high-efficiency devices.

Lopes *et al.* report 3 ultra-thin solar cells: with KF-PDT; with rear passivation; and simultaneously with KF-PDT and rear passivation [94]. Therefore, the various combinations between KF-PDT and rear passivation will be modelled. So, to discriminate the passivated cell with the non-passivated cell regarding the optical rear reflection, the values were set to 30 % and 50 %, respectively based on [69, 70]. These referred rear optical reflection values correspond to the 900 – 1000 nm light wavelength range, with a higher probability of reaching the rear contact. Additionally, the shunt conductance and series resistance were extracted from J-V measurements and applied in the final ultra-thin model in Table 3.9.

Regarding the rear passivation, and since ultra-thin devices have high rear interface recombination, it is introduced a rear surface recombination velocity (SRV) of $10^7\,\mathrm{cm}\cdot\mathrm{s}^{-1}$ for the non-passivated models, in opposition to the $10^2\,\mathrm{cm}\cdot\mathrm{s}^{-1}$ for the passivated models [69, 71]. Hence, the SRV variation models the rear passivation effect of the alumina layer.

The PDT modelled devices incorporate the PDT features introduced in the electrical parameters optimisation in section 3.1. However, some experimental characteristics were introduced, such as the net carrier concentration value experimentally obtained through C-V measurements, although with maintained higher concentration values characteristic of PDT in this modelling. Consequently, the donor compensation in the CIGS layer for the high-efficiency model was removed. It is worth to mention that it is suggested in the experimental work an increased donor defect concentration at the CIGS surface [94], so the ultra-thin model simulations present this feature with the n-type inversion at the SDL layer, recall to Figure 3.1.

Additionally, together with thickness reduction to the ultra-thin absorber, the bandgap was defined according to the GGI profile measured by glow-discharge optical emission spectroscopy and considered to be equal across all devices, as the CIGS deposition occurred in the same batch [94], with the respective electro-affinity variation.

Furthermore, it was set two different poles regarding bulk defect density, named as low and high defects. Additionally, the simpler single bulk defect from the initial model in section 3.1 is tested together with the more experimental double defects present in the final baseline model to high-efficiency devices, Figure 3.9. The objective is to achieve the best fit to experimental results, considering the different combinations of KF-PDT and passivation.

The low defect models correspond to the defect density used in the previous models, while in the high defect models the CIGS defect density is increased, together with the CdS defects. It is noted that for the double defects the higher defect density is applied only to the GB defects. The results are present in the scheme of Figure 3.9, which can be compared with experimental results inside brackets in Table 3.9.

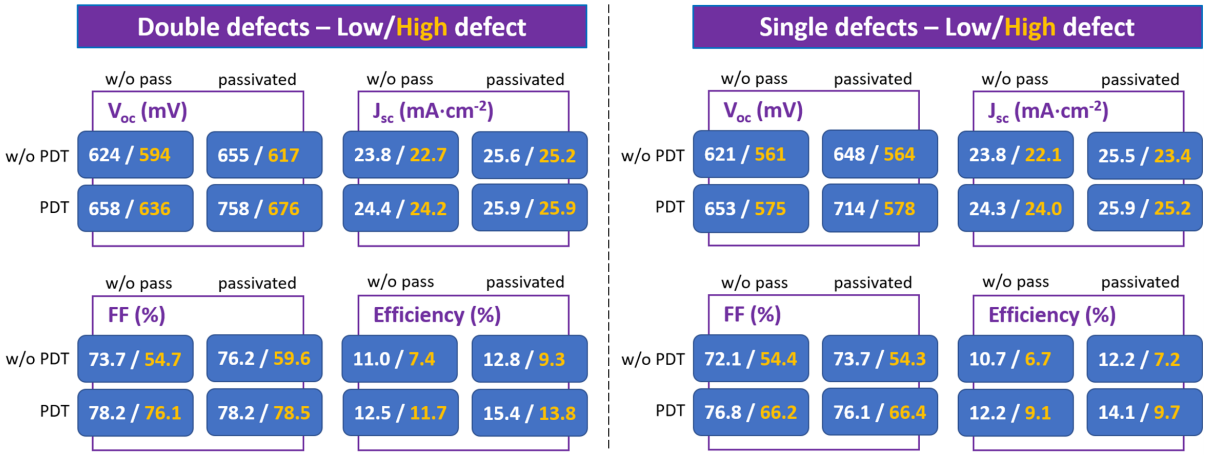

Figure 3.9: Scheme with the Figures of Merit results of the different combinations test: double/single defects and low/high defect. The double defects refers to double acceptors/donors already mentioned in this study, while the single defects replaces the double defects and uses the CIGS bulk defect used in the initial model, Table A.2 and Table A.1 respectively. The High defect represent an overall increase in the CIGS bulk defects: GB defect density increases from $5.0{\times}10^{15}\,\mathrm{cm}^{-3}$ wo PDT and the grading $5.0{\times}10^{13}$ - $2.0{\times}10^{13}\,\mathrm{cm}^{-3}$ PDT to $1.5{\times}10^{16}/7.5{\times}10^{15}\,\mathrm{cm}^{-3}$ (double/single defects) wo PDT and $5.0{\times}10^{15}$ - $2.0{\times}10^{15}/5.0{\times}10^{14}$ - $2.0{\times}10^{14}\,\mathrm{cm}^{-3}$ (double/single defects) PDT. Additionally, only for single defects, GB defect density increase for high defects is coupled with the CIGS single bulk defect density increase from $1.0{\times}10^{14}$ to $2.6{\times}10^{15}\,\mathrm{cm}^{-3}$. Please see Table 3.9 for experimental results.

3.2.2 Modelling Validation with Experimental Data

The results present in Figure 3.9 allow to conclude that both results with low defects, left and right respectively, reproduce Figures of Merit values much higher than the experimental ultra-thin solar cells data in [94], with more impact on V_{oc} and FF.

Therefore, the high defect models fit better the increased defect density in ultra-thin solar cells, possibly due to a non-optimised absorber deposition compared to the thicker high-efficiency counterparts. Moreover, the single defect model High defect does not quite reproduce the experimental findings, as the passivation does not influence the V_{oc} and FF values in the models with and without PDT, where in the experimental results there is a clear positive effect of the rear passivation. It suggests that rear passivation only gains importance and greatly benefit the solar cells' performance if manufacturers firstly address such CIGS high bulk defects, that could dominate the device performance.

Nonetheless, comparing the simulation results for the low and high defect models, one observes that the variation in the figures of merit is even higher for the low defect model. So, the simulation suggests that if one tackle the high CIGS bulk defect density, the effects of PDT and rear passivation improve even further the ultra-thin solar cells performance.

Finally, the high defect model with double defects provides the best fit considering the different combinations. Although the V_{oc} in general and the FF for the PDT devices are higher in simulation than the experimental results, the trend in the simulation results is the same as the experimental ultra-thin solar cells, which indicates good modelling of the KF-PDT and rear passivation effects. This model was used to discuss the experimental work performed within the group and reported in [94]. Furthermore, the model and experimental results are present in Table 3.9.

Table 3.9: Simulated and experimental (in brackets with averages and standard deviation values) results for the 3 devices in [94]. The simulated results follow the combination of double defects + high defects from Figure 3.9. In this simulation, it was introduced the experimental series and shunt resistances for each device [94]

Device	V_{oc} (mV)	J_{sc} (mA $\cdot$ cm^{-2})	FF (%)	η (%)
KF-PDT	631 (519 ± 45)	24.1 (23.2 ± 1.5)	66.5 (49.0 ± 4.9)	10.1 (5.7 ± 1.6)
Rear passivation	612 (426 ± 16)	25.1 (25.4 ± 0.3)	54.4 (51.4 ± 2.6)	8.4 (5.6 ± 0.5)
Rear pass. + KF-PDT	675 (604 ± 20)	25.8 (25.5 ± 0.7)	66.9 (51.3 ± 2.4)	11.7 (7.9 ± 0.7)

The higher simulated V_{oc} in the model that was used to discuss experimental work, high defect model with double defects in Figure 3.10 and Table 3.9, could be a result of recombination losses due to a higher number of defects that we could not simulate. The high recombination losses were evidenced by the J-V measurements and time-resolved photoluminescence (TRPL) decay times performed on the devices [94].

The high FF simulated values for the PDT devices, greater than 10 % absolute compared with the experimental data, may be attributed to the existence of an electron barrier limiting charge collection, resultant of the PDT process and not included in the model. Recent studies [88, 128, 139] report the formation of an Alkali-In-Se_2 layer at the CIGS surface due to the heavy alkali PDT process, which forms an electron barrier and lowers the FF. Figure 3.10 shows the effect of introducing the $KInSe_2$ layer between the CIGS absorber and the CdS buffer, focusing on this layer thickness. Since the experimental devices with KF-PDT show collection losses, and even a roll-over in the J-V curve for the device with additional rear passivation [94], the simulated $KInSe_2$ thickness variation indicates that these devices may have this layer at some extent, lowering the FF. So, after experimental validation that such layer is present, it could easily be implemented in the ultra-thin model.

Furthermore, all devices show an excellent fitting with the experimental J_{sc} values, which indicates a good fitting of the optical properties in the models.

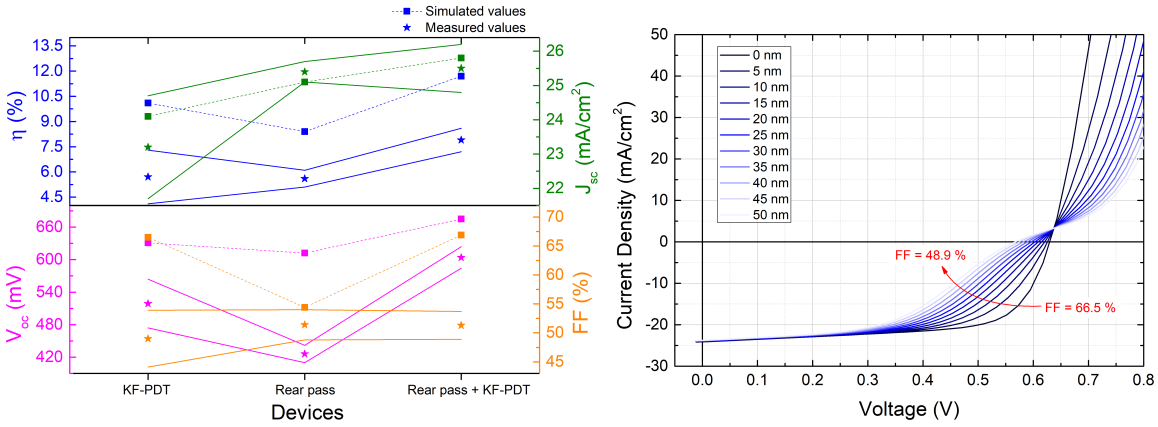

Figure 3.10: Left - Comparison between the simulated (filled squares with dashed connecting lines) and measured (filled stars) solar cells figures of merit. The solid lines represent the uncertainty associated with each device measurement, also present in Table 3.9. Right - J-V curves for different $KInSe_2$ thickness from 0 to 50 nm, that was incorporated into the model (without passivation) between the SDL and CdS layers. The same trend is observed for the model with passivation (not shown here).

In short, the simulation results for the ultra-thin solar cell devices follow the same trend as the experimental results and suggest that combining PDT with rear interface passivation enhances the solar cell performance even further compared to the application of only one of these processes. Moreover, it is important to address the CIGS bulk recombination to achieve the full potential of rear passivation and to have an effective impact in the ultra-thin solar cells performance.

Furthermore, the model used to discuss the experimental ultra-thin devices paves the way for a baseline model of ultra-thin CIGS solar cells.

3.3 Limitations of Ultra-Thin Solar Cells

This section highlights some of the possible limiting factors that hinder the performance of ultra-thin solar cells, based on the simulations work performed in the previous sections.

So, it will be briefly discussed how some improvements in the optical properties, namely rear and front reflection, affect the performance of the ultra-thin devices. Furthermore, electrical characteristics, i.e. rear and bulk recombination, will be varied to assess the respective impact in the cell's performance.

3.3.1 Optical Limitations

In sub-section 3.1.3, the electrical model adopted the rear Mo optical reflection from optical simulations. Additionally, it was tuned the front reflection according to an experimental high-efficiency device.

It is demonstrated in Figure 3.11 that the incorporation of a reflector at the rear contact has the potential to further increase the J_{sc} from 25.9 $mA \cdot cm^{-2}$ to 27.7 $mA \cdot cm^{-2}$. Note that this rear reflector is applied to the electrical model with PDT and passivation while maintaining all the parameters and conditions as in section 3.2. The impact of the rear reflector is amplified in the ultra-thin solar cells compared to the thicker counterparts due to the lower probability of light absorption in its first passage through the ultra-thin absorber [73, 77]. To model such rear

reflector, the optical rear reflection value was increased to 92 % at the rear contact in SCAPS-1D, instead of the 50 % value for the passivated model, whose effect is present in Figure 3.11. This reflection value follows the minimum simulated value that is reported elsewhere for a metal/dielectric stack at the rear contact [70].

On the other hand, the deposition of the ARC layer, without the above mentioned rear reflector, significantly enhances the J_{sc} value from 25.9 mA · cm^{-2} to 27.9 mA · cm^{-2}, Figure 3.11. Additionally, improvements on the anti-reflection properties, e.g. with a nanostructured transparent conductive oxide (TCO) window layer, may reduce even further the front reflection losses. The optical simulation of the front reflection with the nanostructured TCO show the elimination of most of the previous interference fringes, which further enhanced the J_{sc} performance as presented in Figure 3.11 to 28.1 mA · cm^{-2}. The performance impact of this optimised nanostructured TCO is even higher for thicker thin-film solar cells due to lower front reflection in the IR region (not shown here). The ARC layer is modelled with input on the front reflection from the Lumerical 3D optical simulations.

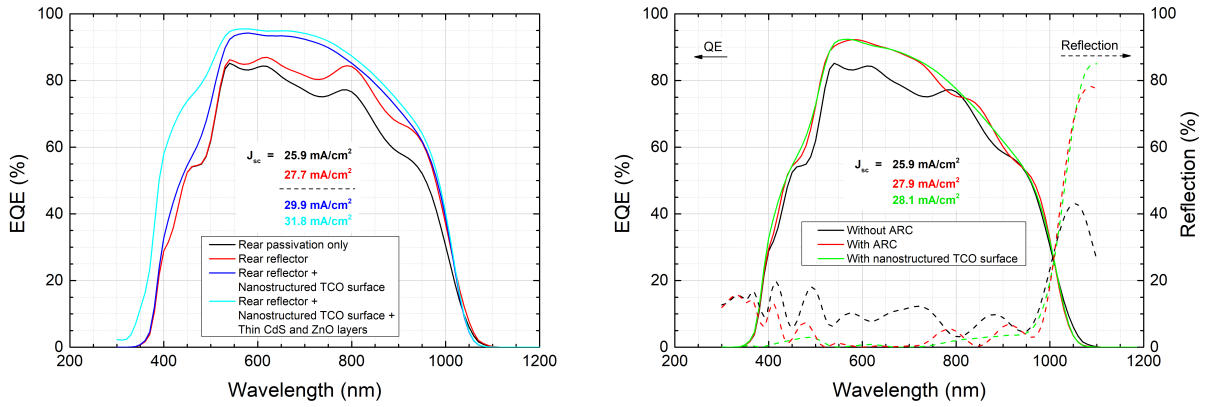

Figure 3.11: EQE curves for the optical optimisation at both the rear and front contact (left) and only at the front contact (right), with the model including PDT and passivation. J_{sc} improvements are presented inset. The thin CdS and ZnO layers at the left light blue curve refers to the thickness used in baseline model for high-efficiency devices.

Thus, optical improvements both at the rear and at the front contact may be introduced in the solar cells to address the light absorption losses due to the thickness reduction of the ultra-thin absorbers. The combined effect of both high rear optical reflection and reduced front reflection would lead to a J_{sc} improvement, respective efficiency in brackets, from 25.9 mA · cm^{-2} (13.8 % eff.) to 29.9 mA · cm^{-2} (16.0 % eff.). Note that further optimisation in the reduction of the buffer and window layers thickness may lead to an increased J_{sc} of 31.8 mA · cm^{-2} (17.3 % eff.), here with the CdS and ZnO layers thickness as in section 3.1.

3.3.2 Recombination Losses Limitations

This sub-section tests the solar cell parameters above mentioned and modelled in section 3.2.

The ultra-thin devices are more sensitive to recombination losses at the rear contact due to the proximity of the heterojunction interface and generation of minority carriers near the rear contact. So, Figure 3.12 shows the Figures of Merit results for different SRV values to demonstrate the impact on the performance of the solar cells. Note that this SRV variation does not include the increased rear optical reflection that might come from passivation structures.

We observe from Figure 3.12 that the rear interface heavily affects the performance of ultra-thin solar cells. However, below the rear SRV of 10^4 cm · s^{-1} only small changes in the Figures of Merit are detected. Typically, the passivated devices present recombination velocity values lower than 10^4 cm · s^{-1}, and even an optimum passivation with $SRV = 10^2$ cm · s^{-1} [64, 69]. So,

it is feasible the fabrication of passivated ultra-thin solar cells that takes advantage of low rear recombination probability, with a high potential to have a significant impact on the respective performance.

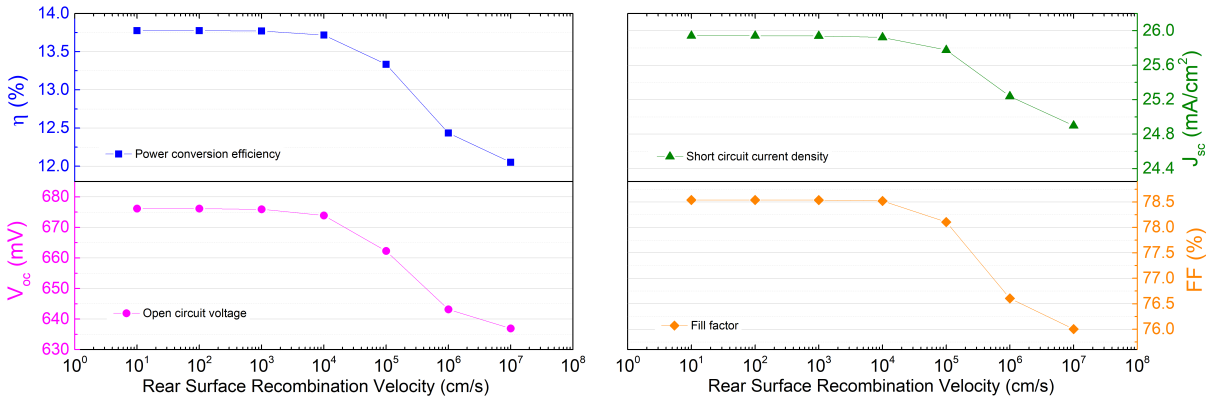

Figure 3.12: Figures of Merit values for different recombination velocity values at the rear contact. It was used the model with PDT without passivation and without R_s and R_p.

Regarding the bulk recombination together with passivation, Figure 3.13 presents the J-V curves and some Figures of Merit results for different values of bulk GB defect density. One concludes that there is an increase in the performance of these ultra-thin solar cells both for devices with and without passivation, i.e. with SRV of 10^2 and 10^7 cm $\cdot$ s^{-1} respectively. Moreover, the results indicate that the passivation clearly potentiates the performance of the solar cell with the reduction of the bulk defect density, i.e. bulk recombination probability. The improvement of the CIGS bulk properties may be achieved with an optimised PDT, as already mentioned. Furthermore, the conclusions about the impact of the rear SRV and CIGS bulk recombination follow the results with the baseline model to ultra-thins devices, demonstrating the importance of passivation and PDT in ultra-thin CIGS solar cells.

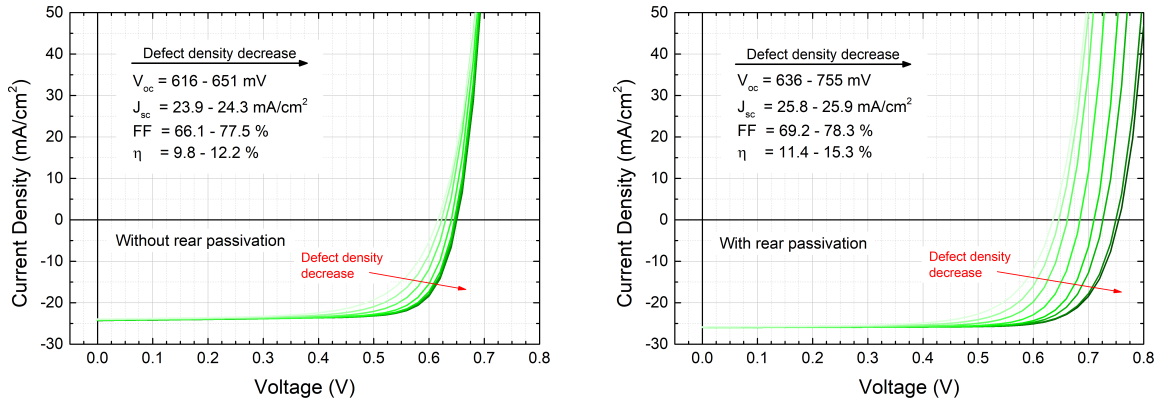

Figure 3.13: Impact of the GB defect density on the ultra-thin solar cell performance for the model with PDT without passivation (left) and with passivation (right). Note that with rear passivation, the defect density decrease lead to a V_{oc} value higher compared with the high-efficiency record cell from ZSW.

Interestingly, de Wild *et al.* reported a saturation in the V_{oc} value in their devices with KF-PDT, but without passivation, to about 640 mV [140], which is in great agreement with the value obtained with this work without passivation, demonstrating again that the model that is being created is in agreement with experimental data.

This study focused on the update of old baseline models with experimentally-based features, that include the recent advances in the CIGS technology, namely the PDT effects. Furthermore, the baseline model to high-efficiency devices was applied to ultra-thin solar cells. So, the limitations of the ultra-thin devices is highlighted in this section and it would result in a significantly improved performance towards the high-efficiency thicker counterparts. It was suggested performance optimisations in the optical parameters with the ARC layer and rear reflector, together with the electrical optimisations with interface passivation and bulk defects.

Finally, if we apply all the mentioned optical and electrical optimisations, ultra-thin solar cells may achieve an efficiency of 19.0 % (V_{oc} 750 mV; J_{sc} 31.8 mA $\cdot$ cm^{-2}; FF 79.5 %) which is +11.6 % abs. compared with the model used to describe the experimental data in subsection 3.2.2 without passivation and without PDT (7.4 % eff.). We note that the simulated V_{oc} values are above the ones of the world record cell. This happens mostly because with thinner layers, less bulk recombination takes place [41], and even if the defect level is still high, there is already a positive effect. Such detail means that if the CIGS quality of ultra-thin layers can reach the conventional ones, the ultra-thin devices could ultimately overtake conventional devices in terms of performance. On the other hand, the tremendous performance enhancement demonstrate that the optimised PDT and passivation together with optimised optical rear and front reflection may have a real impact in ultra-thin devices and, at last, in its future wide commercialisation.

3.4 Experimental Rear Passivation Structure

This final section optimises a lift-off procedure aiming to create a nanostructured Mo rear contact with an additional metal and dielectric layers. The objective is to benefit from the dielectric passivation effect and the increased rear optical reflection with the highly reflective metal layer, mitigating some limitations of ultra-thin CIGS solar cells.

A previous study report the deposition of the two mentioned layers followed by an etch procedure [78]. However, it often led to inter-diffusion between the metal layer and the CIGS absorber due to the harsh conditions in the absorber growth, deteriorating the solar cell performance. So, this study focuses on the encapsulation of the metallic layer by the passivating dielectric with industrial-friendly processes and optimised nanostructures dimension. Please see Figure 2.2 in Materials and Methods to remember the desired final structure. The dimension optimisation requires a calibration step in the photolithographic exposure conditions.

3.4.1 Calibration

It was varied two parameters in the exposure conditions (F and I) at the lithography step and the development time of the bi-layer PR (40 s, 45 s, and 50 s). So, to chose between the different parameters, it was observed the samples after the development step in the optical microscope, some images in Figure B.5 in annexes. One verifies that the laser Intensity has more impact on the undercut than the laser Focus. So, for 45 and 50 s development time, $I \geq 50$ % leads to the peel-off of the lines due to full development of the bottom resist. Furthermore, the repeated experience on several calibration steps and from optical microscope images allow to conclude that for laser Intensity of 40 %, the samples are underdeveloped or produces low undercut values (< 50 nm). The latter would lead to low passivation coverage areas and high rear contact line width, reducing the passivation benefit. The combination of 40 s and 50 % also produced lower undercut values compared with the chosen combination. Note that the line pattern in Figure B.5 is created due to the slight variation of the beam intensity through the movement of the laser when the laser head remains fixed ($\approx 160\,\mu$m). Therefore, the combination Intensity of 60 %, development time of 40 s and both Focus were analysed through SEM images.

Although there are no major differences between Focus −20 and −40, it was chosen the *F* −40, present in Figure 3.14, due to slightly higher uniformity than *F* −20. The SEM cross-section analysis in Figure 3.14 allowed to assess the suitability of the resists profile. It was obtained a bottom resist width value of ≈ 550 − 600 nm, i.e. rear Mo contact width value, a passivation line width ≈ 2.2 µm and the defined 1.6 µm line width for the area that benefits from the highly reflective metal.

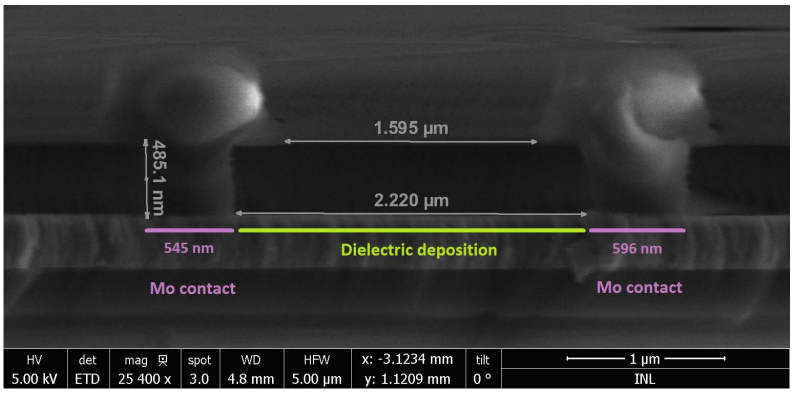

Figure 3.14: SEM cross-section image of the resists profile with the chosen combination of parameters *I* 60 %, *F* -40 and development time 40 s.

3.4.2 Lift-off

The parameters chosen above were applied to the fabrication of the whole rear nanostructure, as mentioned in chapter 2.

Figure 3.15 a) shows the SEM cross-section image of the sample after the Mo etch step. The etch of Mo introduced some roughness or dirt in the exposed area as seen in Figure 3.15 a) in-between the resist sections. Posterior energy-dispersive X-ray spectroscopy (EDX) analysis revealed the presence of Cu in the sample lines (not shown here), which was attributed to a contamination during the Al sputtering deposition. Consequently, during the etch process and after the Mo over-etch, the Cu metal redeposited on the substrate, as the RIE equipment and the recipe used do not allow the etch of some metals, namely Au, Ag, and Cu, due to the gas chemistry used. Additionally, one observes some lateral etching of the bottom resist, increasing slightly the undercut, comparing Figure 3.14 and Figure 3.15 a).

The effectiveness of the lift-off is shown by the top and cross-section images in Figure 3.15 b) and c). Furthermore, the conformability of the dielectric deposition is visible by the SEM images. It was obtained a rear contact line width of about 550 nm and a dielectric/metal stack line width of about 1.8 um, with a pitch of 2.8 um, representing a passivation area of 80 % and a metal stack coverage area 64 %. Other studies within the group report the rear optical reflection benefits [78, 95, 99] and the optimised passivation area around the 80 % coverage[141].

In Figure B.6, the AFM analysis confirms the presence of the dielectric underneath the resist undercut due to the step between the rear Mo contact and the dielectric layer of ≈ 18 nm, in agreement with the respective dielectric deposition value.

Finally, the uniformity of the nanostructures dimension through the substrate was confirmed by the observation of different SEM top images at different locations of the substrate. One example top image is present in Figure B.7 in annexes.

With industrial-friendly processes, the rear passivation was implemented together with a highly reflective rear contact strategy, which comprises a double layer of metal encapsulated by the dielectric. However, one limitation is the lift-off of the dielectric that limits the dielectric deposition temperature. Nonetheless, it was tested the lift-off of an alumina layer deposited by low-temperature (≈ 100 ºC) ALD, at the beginning of this study, which would be considered

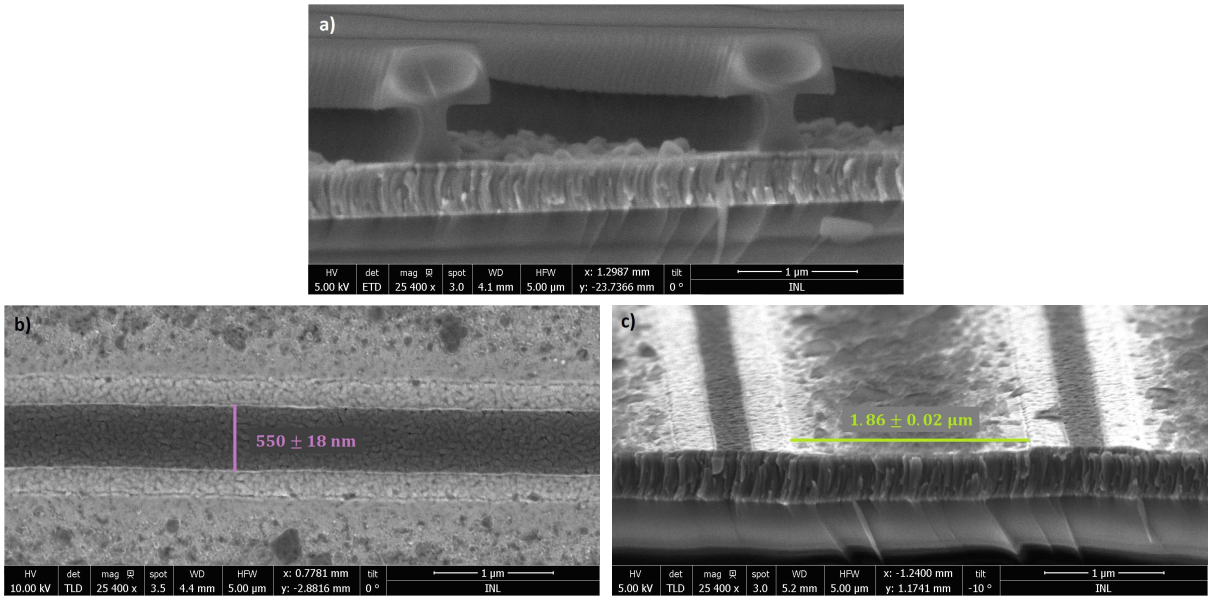

Figure 3.15: SEM cross-section image before (a) and after (c) the lift-off, and top image (b) after the lift-off. The dimensions presented within the images correspond to 10 different measurements at different locations and images with the same scale.

to be difficult due to its high conformability, SEM top view in Figure B.8 in annexes. The lift-off of the ALD alumina was successful even with the non-optimised nanostructures, which, although with non-uniform rear contact lines and no encapsulation, the lift-off was possible. The ALD alumina lift-off success makes the rear contact optimisation techniques used in this study compatible with high-quality dielectric passivating layers. So, as this structure allows for rear electrical passivation and high optical rear reflection, the door to achieve the ultra-thin high performance that the model predicts is now open.

4 | Conclusion and Future Perspectives

The work performed with this thesis provided with an update of the older baseline electrical models with SCAPS-1D and compared with high-efficiency solar cells. With the old baseline from Pettersson *et al.*, it was update the CIGS bulk defects based on experimental and theoretical results from literature. The experimental-based bulk defects allowed for a decoupling between native points defects from the grain interior and the grain boundary defects of such polycrystalline CIGS absorbers used in high-efficiency devices. Therefore the electrical model was capable of introducing the reported PDT effect of GB passivation. Several other electrical and optical characteristics were optimised together with the study of some PDT effects on CIGS solar cells. Furthermore, the Lumerical FDTD software provided with the rear and front reflection values, through 3D optical simulations.

It was observed that the PDT bulk effects led to a greater impact in the solar cell performance than the PDT interface effects, in agreement with recent studies, mainly due to GB passivation and strong reduction of bulk recombination, affecting mostly V_{oc} and FF. Furthermore, the performance improvement with the incorporation of PDT was about 3 %, also in agreement with the experimental record cells results. Additionally, it was modelled the record cell from ZSW with 22.6 % with comparable results. There is now a working tool that the community can use to understand where to concentrate their efforts. The identification that the PDT effect on front interface recombination leads to minimal impact in device performance is of the utmost importance as it indicates that there is a vast potential to improve there with for instance front passivation layers [142].

The baseline for high-efficiency devices was applied to ultra-thin solar cells and tested different combinations regarding CIGS bulk defects. It was demonstrated that the increased defect density in ultra-thin experimental devices were better fitted with the high defect model, possibly due to a non-optimised absorber deposition compared to the thicker high-efficiency counterparts. Such fact is already an indication that efforts should be made into increasing the bulk quality of ultra-thin layers. Examples of such improvement can be increasing deposition time, increasing deposition temperature or to improve the control over the introduction of Na. Furthermore, the simulation results follow the same trend as the experimental results and suggests that combining PDT with rear interface passivation enhances the solar cell performance even further compared to the application of only one of these processes. This model paves the way for a baseline model of ultra-thin CIGS solar cells.

Together with the electrical optimisations referred above, the optical limitations may be addressed with improvements at rear contact with incorporation of a rear reflector and at the front contact with optimisation of the anti-reflection properties. If one incorporates all the optical and electrical optimisations at an architecture level, it was demonstrated an improved ultra-thin cell performance of 19 % compared to only 7.4 % conversion efficiency for the model without PDT and without rear passivation, with even higher V_{oc} values compared to the ZSW record cell. Nonetheless, this high-performed ultra-thin device lacks of an optimised bandgap grading. Moreover, a higher bandgap buffer layer would enhance even further the J_{sc} value and respective performance. The aforementioned CIGS quality improvements could also lead the ultra-thin devices to performance values close, or even higher, than traditional devices as it was demonstrated by the very high simulated V_{oc} value even with a high defect quality.

Future tests with the baseline model may be performed to further guarantee its reliability, such as admittance simulations. Furthermore, additional tests regarding the CIGS solar cell properties will contribute to the understanding of the respective effects, namely compensating defects and absorber-buffer-window layers band alignment as an example.

The experimental results revealed the feasibility of a rear structure that simultaneously provides a higher reflection and benefit from passivation, with an industrially-friend lift-off

process, paving the way for the high-performing ultra-thin devices that were modelled previously. A rear architecture that comprises of both electrical passivation and the incorporation of a highly reflective layer had never been manufactured before this thesis. It was successfully fabricated a metal layer encapsulated with a dielectric at the rear surface with optimised rear contact dimensions. Additionally, it was proven the possibility of an effective lift-off of an alumina deposited by low temperature ALD, which allow high-quality passivating layers to be processed with the techniques used in this study. The fully development of a process suitable to be adapted in the industry will be further achieved with exposure techniques compatible with high throughput, such as the nano-imprint lithography which would allow a better control on the features dimension. The obtained rear structure has the potential of contributing to the future of high-efficiency ultra-thin CIGS solar cells.

It is noted that from the work performed within this thesis resulted in direct contribution on the simulation of ultra-thin solar cells for a scientific paper as a co-author already submitted to *ACS Applied Materials and Interfaces* [94]. Additionally, another scientific paper, as main author, is already being written to be submitted, aiming to report the updated baseline model adapted to recent CIGS solar cells and that has not been reported at the time of writing of this thesis.

Bibliography

[1] C. Breyer, D. Bogdanov, A. Aghahosseini, A. Gulagi, M. Child, A. S. Oyewo, J. Farfan, K. Sadovskaia, and P. Vainikka. "Solar photovoltaics demand for the global energy transition in the power sector." In: *Progress in Photovoltaics: Research and Applications* 26.8 (2018), pp. 505–523. DOI: 10.1002/pip.2950.

[2] NBC News. *Read Greta Thunberg's full speech at the United Nations Climate Action Summit*. 2019. URL: https://www.nbcnews.com/news/world/read-greta-thunberg-s-full-speech-united-nations-climate-action-n1057861 (visited on 07/13/2020).

[3] H. Ritchie and M. Roser. *Energy*. 2018. URL: https://ourworldindata.org/energy (visited on 07/14/2020).

[4] BP. *Statistical Review of World Energy*. Tech. rep. 2020. URL: bp.com/statisticalreview.

[5] A. Jäger-waldau. "Snapshot of Photovoltaics—February 2020." In: *Energies* 13.930 (2020), pp. 1–8. DOI: 10.3390/en13040930.

[6] I. E. Agency. *World Energy Outlook 2019*. Tech. rep. 2019. URL: https://www.iea.org/reports/world-energy-outlook-2019{\#}.

[7] *White paper for CIGS thin-film solar cell technology*. 2019. URL: https://cigs-pv.net/wortpresse/wp-content/uploads/2019/04/CIGS{_}White{_}Paper{_}2019{_}online.pdf (visited on 07/15/2020).

[8] B. Dimmler, M. Ag, and R. S. Hall. "CIGS and CdTe based thin film PV modules, an industrial r/evolution." In: *2012 38th IEEE Photovoltaic Specialists Conference* (2011), pp. 2494–2499. DOI: 10.1109/PVSC.2012.6318101.

[9] L. Stamford and A. Azapagic. "Environmental impacts of copper indium gallium-selenide (CIGS) photovoltaics and the elimination of cadmium through atomic layer deposition." In: *Science of the Total Environment* 688 (2019), pp. 1092–1101. DOI: 10.1016/j.scitotenv.2019.06.343.

[10] A. Chirila, S. Buecheler, F. Pianezzi, P. Bloesch, C. Gretener, A. R. Uhl, C. Fella, L. Kranz, J. Perrenoud, S. Seyrling, R. Verma, S. Nishiwaki, Y. E. Romanyuk, G. Bilger, and A. N. Tiwari. "Highly efficient Cu(In,Ga)Se_2 solar cells grown on flexible polymer films." In: *Nature Materials* 10.11 (2011), pp. 857–861. DOI: 10.1038/nmat3122.

[11] R. Carron, S. Nishiwaki, T. Feurer, R. Hertwig, E. Avancini, J. Löckinger, S. C. Yang, S. Buecheler, and A. N. Tiwari. "Advanced Alkali Treatments for High-Efficiency Cu(In,Ga)Se_2 Solar Cells on Flexible Substrates." In: 9.24 (2019), p. 1900408. DOI: 10.1002/aenm.201900408.

[12] M. Powalla, S. Paetel, D. Hariskos, R. Wuerz, F. Kessler, P. Lechner, W. Wischmann, and T. M. Friedlmeier. "Advances in Cost-Efficient Thin-Film Photovoltaics Based on Cu(In,Ga)Se_2." In: *Engineering* 3.4 (2017), pp. 445–451. DOI: 10.1016/J.ENG.2017.04.015.

[13] M. Nakamura, K. Yamaguchi, Y. Kimoto, Y. Yasaki, T. Kato, and H. Sugimoto. "Cd-Free Cu(In,Ga)(Se,S)$_2$ Thin-Film Solar Cell With Record Efficiency of 23.35%." In: *IEEE Journal of Photovoltaics* 9.6 (2019), pp. 1863–1867. DOI: 10.1109/JPHOTOV.2019.2937218.

[14] M. Raymond, K. Hudai, W. Peter, and K. Jaakko. *Critical Metals in Strategic Energy Technologies - Assessing Rare Metals as Supply-Chain Bottlenecks in Low-Carbon Energy Technologies*. Tech. rep. European Commission Joint Research Centre, 2011. URL: https://publications.jrc.ec.europa.eu/repository/handle/JRC65592.

[15] J. Pettersson, C. Platzer-Björkman, U. Zimmermann, and M. Edoff. "Baseline model of graded-absorber Cu(In,Ga)Se_2 solar cells applied to cells with $Zn_{1-x}Mg_xO$ buffer layers." In: *Thin Solid Films* 519.21 (2011), pp. 7476–7480. DOI: 10.1016/j.tsf.2010.12.141.

[16] M. Gloeckler, A. L. Fahrenbruch, and J. R. Sites. "Numerical modeling of CIGS and CdTe solar cells: Setting the baseline." In: *3rd World Conference on Photovoltaic Energy Conversion*. Osaka, Japan, 2003, pp. 491–494.

[17] P. Jackson, D. Hariskos, E. Lotter, S. Paetel, R. Wuerz, R. Menner, W. Wischmann, and M. Powalla. "New world record efficiency for Cu(In,Ga)Se_2 thin-film solar cells beyond 20%." In: *Progress in Photovoltaics: Research and Applications* 19.7 (2011), pp. 894–897. DOI: 10.1002/pip.1078.

[18] P. Salomé. "Chalcogenide Thin Films for Solar Cells: Growth and Properties." Doctoral dissertation. University of Aveiro, 2011, pp. 1–161. URL: http://hdl.handle.net/10773/3723.

[19] G. Ciulla, V. Lo Brano, V. Di Dio, and G. Cipriani. "A comparison of different one-diode models for the representation of I-V characteristic of a PV cell." In: *Renewable and Sustainable Energy Reviews* 32 (2014), pp. 684–696. DOI: 10.1016/j.rser.2014.01.027.

[20] S. M. Sze and K. K. Ng. *Physics of semiconductor devices*. John wiley & sons, 2006.

[21] M. Wolf and H. Rauschenbach. "Series resistance effects on solar cell measurements." In: *Advanced Energy Conversion* 3 (1963), pp. 455–479.

[22] A. Sabadus, V. Mihailetchi, and M. Paulescu. "Parameters extraction for the one-diode model of a solar cell." In: *AIP Conference Proceedings* 1916.040005 (2017). DOI: 10.1063/1.5017444.

[23] C. Zhang, J. Zhang, Y. Hao, Z. Lin, and C. Zhu. "A simple and efficient solar cell parameter extraction method from a single current-voltage curve." In: *Journal of Applied Physics* 110.064504 (2011). DOI: 10.1063/1.3632971.

[24] Y. Tao. "Screen-Printed Front Junction n-Type Silicon Solar Cells." In: *Printed Electronics - Current Trends and Applications*. 2016, pp. 47–73. DOI: 10.5772/63198.

[25] M. A. Green, E. D. Dunlop, J. Hohl-Ebinger, M. Yoshita, N. Kopidakis, and X. Hao. "Solar cell efficiency tables (version 56)." In: *Progress in Photovoltaics: Research and Applications* 28.7 (2020), pp. 629–638. DOI: 10.1002/pip.3303.

[26] S. Wagner, J. L. Shay, P. Migliorato, and H. Kasper. "CdS/$CuInSe_2$ heterojunction photovoltaic detectors." In: *Applied Physics Letters* 25.8 (1974), pp. 434–435. DOI: 10.1063/1.1655537.

[27] J Shay, S. Wagner, and H. Kasper. "Efficient $CuInSe_2$/CdS solar cells." In: *Applied Physics Letters* 27.2 (1975), pp. 89–90. DOI: 10.1063/1.88372.

[28] D. Abou-Ras, S. Wagner, B. J. Stanbery, H. W. Schock, R. Scheer, L. Stolt, S. Siebentritt, D. Lincot, C. Eberspacher, K. Kushiya, and A. N. Tiwari. "Innovation highway: Breakthrough milestones and key developments in chalcopyrite photovoltaics from a retrospective viewpoint." In: *Thin Solid Films* 633 (2017), pp. 2–12. DOI: 10.1016/j.tsf.2017.01.005.

[29] S. H. Wei, S. B. Zhang, and A. Zunger. "Effects of Ga addition to $CuInSe_2$ on its electronic, structural, and defect properties." In: *Applied Physics Letters* 72.24 (1998), pp. 3199–3201. DOI: 10.1063/1.121548.

[30] T. Dullweber, G. Hanna, W. Shams-Kolahi, A. Schwartzlander, M. A. Contreras, R. Noufi, and H. W. Schock. "Study of the effect of gallium grading in Cu(In,Ga)Se2." In: *Thin Solid Films* 361-362 (2000), pp. 478–481. DOI: 10.1016/S0040-6090(99)00845-7.

[31] T. Dullweber, G. Hanna, U. Rau, and H. W. Schock. "New approach to high-efficiency solar cells by band gap grading in Cu(In,Ga)Se_2 chalcopyrite semiconductors." In: *Solar Energy Materials and Solar Cells* 67 (2001), pp. 145–150. DOI: 10.1016/S0927-0248(00)00274-9.

[32] S. Minoura, K. Kodera, T. Maekawa, K. Miyazaki, S. Niki, and H. Fujiwara. "Dielectric function of Cu(In, Ga)Se_2-based polycrystalline materials." In: *Journal of Applied Physics* 113.6 (2013), p. 063505. DOI: 10.1063/1.4790174.

[33] A. M. Gabor, J. R. Tuttle, D. S. Albin, M. A. Contreras, R. Noufi, and A. M. Hermann. "High-efficiency $CuIn_xGa_{1x}Se_2$ solar cells made from $(In_x,Ga_{1x})_2Se_3$ precursor films." In: *Applied Physics Letters* 65.2 (1994), pp. 198–200. DOI: 10.1063/1.112670.

[34] P. M. Salomé, V. Fjällström, P. Szaniawski, J. P. Leitão, A. Hultqvist, P. A. Fernandes, J. P. Teixeira, B. P. Falcão, U. Zimmermann, A. F. da Cunha, and M. Edoff. "A comparison between thin film solar cells made from co-evaporated $CuIn_{1-x}Ga_xSe_2$ using a one-stage process versus a three-stage process." In: *Progress in Photovoltaics: Research and Applications* 23.4 (2015), pp. 470–478. DOI: 10.1002/pip.2453.

[35] T. Nakada and A. Kunioka. "Direct evidence of Cd diffusion into Cu(In,Ga)Se_2 thin films during chemical-bath deposition process of CdS films." In: *Applied Physics Letters* 74.17 (1999), pp. 2444–2446. DOI: 10.1063/1.123875.

[36] M. Bodegård, L. Stolt, and J. Hedström. "The influence of sodium on the grain structure of $CuInSe_2$ films for photovoltaic applications." In: *12th European Photovoltaic Solar Energy Conference*. Amsterdam, The Netherlands, 1994, pp. 1743–1746.

[37] P. Jackson, D. Hariskos, R. Wuerz, W. Wischmann, and M. Powalla. "Compositional investigation of potassium doped Cu(In,Ga)Se_2 solar cells with efficiencies up to 20.8%." In: *Physica Status Solidi - Rapid Research Letters* 8.3 (2014), pp. 219–222. DOI: 10.1002/pssr.201409040.

[38] A. Chirilă, P. Reinhard, F. Pianezzi, P. Bloesch, A. R. Uhl, C. Fella, L. Kranz, D. Keller, C. Gretener, H. Hagendorfer, D. Jaeger, R. Erni, S. Nishiwaki, S. Buecheler, and A. N. Tiwari. "Potassium-induced surface modification of Cu(In,Ga)Se_2 thin films for high-efficiency solar cells." In: *Nature Materials* 12.12 (2013), pp. 1107–1111. DOI: 10.1038/nmat3789.

[39] P. Jackson, R. Wuerz, D. Hariskos, E. Lotter, W. Witte, and M. Powalla. "Effects of heavy alkali elements in Cu(In,Ga)Se_2 solar cells with efficiencies up to 22.6%." In: *Physica Status Solidi - Rapid Research Letters* 10.8 (2016), pp. 583–586. DOI: 10.1002/pssr.201600199.

[40] T. Kato, J. L. Wu, Y. Hirai, H. Sugimoto, and V. Bermudez. "Record Efficiency for Thin-Film Polycrystalline Solar Cells Up to 22.9% Achieved by Cs-Treated Cu(In,Ga)$(Se,S)_2$." In: *IEEE Journal of Photovoltaics* 9.1 (2019), pp. 325–330. DOI: 10.1109/JPHOTOV.2018.2882206.

[41] R. Brendel and H. J. Queisser. "On the thickness dependence of open circuit voltages of p-n junction solar cells." In: *Solar Energy Materials and Solar Cells* 29.4 (1993), pp. 397–401. DOI: 10.1016/0927-0248(93)90098-N.

[42] D. Rudmann, D. Brémaud, A. F. Da Cunha, G. Bilger, A. Strohm, M. Kaelin, H. Zogg, and A. N. Tiwari. "Sodium incorporation strategies for CIGS growth at different temperatures." In: *Thin Solid Films* 480-481 (2005), pp. 55–60. DOI: 10.1016/j.tsf.2004.11.071.

[43] L. Assmann, J. C. Bernède, A. Drici, C. Amory, E. Halgand, and M. Morsli. "Study of the Mo thin films and Mo/CIGS interface properties." In: *Applied Surface Science* 246.1-3 (2005), pp. 159–166. DOI: 10.1016/j.apsusc.2004.11.020.

[44] T. Wada, N. Kohara, S. Nishiwaki, and T. Negami. "Characterization of the Cu(In,Ga)Se_2/Mo interface in CIGS solar cells." In: *Thin Solid Films* 387.1-2 (2001), pp. 118–122. DOI: 10.1016/S0040-6090(00)01846-0.

[45] P. M. P. Salomé, V. Fjallstrom, A. Hultqvist, P. Szaniawski, U. Zimmermann, and M. Edoff. "The effect of Mo back contact ageing on Cu(In,Ga)Se_2 thin-film solar cells." In: *Progress in Photovoltaics: Research and Applications* 22.1 (2014), pp. 83–89. DOI: 10.1002/pip.2360.

[46] P. M. Salomé, A. Hultqvist, V. Fjällström, M. Edoff, B. Aitken, K. Vaidyanathan, K. Zhang, K. Fuller, and C. Kosik Williams. "Cu(In,Ga)Se_2 solar cells with varying Na content prepared on nominally alkali-free glass substrates." In: *IEEE Journal of Photovoltaics* 3.2 (2013), pp. 852–858. DOI: 10.1109/JPHOTOV.2013.2247655.

[47] P. Jackson, D. Hariskos, R. Wuerz, O. Kiowski, A. Bauer, T. M. Friedlmeier, and M. Powalla. "Properties of Cu(In,Ga)Se_2 solar cells with new record efficiencies up to 21.7%." In: *Physica Status Solidi - Rapid Research Letters* 9.1 (2015), pp. 28–31. DOI: 10.1002/pssr.201409520.

[48] O. Lundberg, M. Edoff, and L. Stolt. "The effect of Ga-grading in CIGS thin film solar cells." In: *Thin Solid Films* 480-481 (2005), pp. 520–525. DOI: 10.1016/j.tsf.2004.11.080.

[49] L. L. Kazmerski. "Ternary-compound thin-film solar cells." In: *Il Nuovo Cimento D* 2.6 (1983), pp. 2013–2028. DOI: 10.1007/BF02457903.

[50] S. B. Zhang, S.-H. Wei, A. Zunger, and H Katayama-Yoshida. "Defect physics of the $CuInSe_2$ chalcopyrite semiconductor." In: *Physical Review B* 57.16 (1998), pp. 9642–9656. DOI: 10.1103/PhysRevB.57.9642.

[51] C. Rincón and R. Márquez. "Defect physics of the $CuInSe_2$ chalcopyrite semiconductor." In: *Journal of Physics and Chemistry of Solids* 60.11 (1999), pp. 1865–1873. DOI: 10.1016/S0022-3697(99)00190-0.

[52] D Schmid, M Ruckh, F Grunwald, and H. W. Schock. "Chalcopyrite / defect chalcopyrite heterojunctions on the basis of $CuInSe_2$." In: *Journal of Applied Physics* 73.6 (1993), pp. 2902–2909. DOI: 10.1063/1.353020.

[53] J. Kiss, T. Gruhn, G. Roma, and C. Felser. "Theoretical study on the structure and energetics of Cd insertion and Cu depletion of $CuIn_5Se_8$." In: *Journal of Physical Chemistry C* 117.21 (2013), pp. 10892–10900. DOI: 10.1021/jp312467f.

[54] E. Ghorbani, J. Kiss, H. Mirhosseini, G. Roma, M. Schmidt, J. Windeln, T. D. Kühne, and C. Felser. "Hybrid-Functional Calculations on the Incorporation of Na and K Impurities into the $CuInSe_2$ and $CuIn_5Se_8$ Solar-Cell Materials." In: *Journal of Physical Chemistry C* 119.45 (2015), pp. 25197–25203. DOI: 10.1021/acs.jpcc.5b07639.

[55] R. Scheer and H.-W. Schock. *Chalcogenide photovoltaics: physics, technologies, and thin film devices*. John Wiley & Sons, 2011.

[56] J. Lindahl, U. Zimmermann, P. Szaniawski, T. Torndahl, A. Hultqvist, P. Salomé, C. Platzer-Björkman, and M. Edoff. "Inline Cu(In,Ga)Se_2 co-evaporation for high-efficiency solar cells and modules." In: *IEEE Journal of Photovoltaics* 3.3 (2013), pp. 1100–1105. DOI: 10.1109/JPHOTOV.2013.2256232.

[57] A. W. Blakers, A. Wang, A. M. Milne, J. Zhao, and M. A. Green. "22.8% Efficient Silicon Solar Cell." In: *Applied Physics Letters* 55.13 (1989), pp. 1363–1365. DOI: 10.1063/1.101596.

[58] M. A. Green. "The Passivated Emitter and Rear Cell (PERC): From conception to mass production." In: *Solar Energy Materials and Solar Cells* 143 (2015), pp. 190–197. DOI: 10.1016/j.solmat.2015.06.055.

[59] B. Vermang, Y. Ren, O. Donzel-gargand, C. Frisk, J. Joel, P. Salomé, S. Sadewasser, C. Platzer-bj, and M. Edoff. "Rear Surface Optimization of CZTS Solar Cells by Use of a Passivation Layer With Nanosized Point Openings." In: *IEEE Journal of Photovoltaics* 6.1 (2016), pp. 332–336. DOI: 10.1109/JPHOTOV.2015.2496864.

[60] J. M. Kephart, A. Kindvall, D. Williams, D. Kuciauskas, P. Dippo, A. Munshi, and W. S. Sampath. "Sputter-Deposited Oxides for Interface Passivation of CdTe Photovoltaics." In: *IEEE Journal of Photovoltaics* 8.2 (2018), pp. 587–593. DOI: 10.1109/JPHOTOV.2017.2787021.

[61] H.-l. Chen, A. Cattoni, R. D. Lépinau, A. W. Walker, O. Höhn, D. Lackner, G. Siefer, M. Faustini, N. Vandamme, J. Goffard, B. Behaghel, C. Dupuis, N. Bardou, F. Dimroth, and S. Collin. "A 19.9%-efficient ultrathin solar cell based on a 205-nm-thick GaAs absorber and a silver nanostructured back mirror." In: *Nature Energy* 4.9 (2019), pp. 761–767. DOI: 10.1038/s41560-019-0434-y.

[62] B. Vermang, H. Goverde, L. Tous, A. Lorenz, P. Choulat, J. Horzel, J. John, J. Poortmans, and R. Mertens. "Approach for Al_2O_3 rear surface passivation of industrial p-type Si PERC above 19 %." In: *Progress in Photovoltaics: Research and Applications* 20 (2012), pp. 269–273. DOI: 10.1002/pip.2196.

[63] B. Vermang, J. T. Wätjen, V. Fjällström, F. Rostvall, M. Edoff, R. Kotipalli, F. Henry, and D. Flandre. "Employing Si solar cell technology to increase efficiency of ultra-thin Cu(In,Ga)Se_2 solar cells." In: *Progress in Photovoltaics: Research and Applications* 22 (2014), pp. 1023–1029. DOI: 10.1002/pip.2527.

[64] B. Vermang, J. T. Watjen, C. Frisk, V. Fjallstrom, F. Rostvall, M. Edoff, P. Salome, J. Borme, N. Nicoara, and S. Sadewasser. "Introduction of Si PERC rear contacting design to boost efficiency of Cu(In,Ga)Se_2 solar cells." In: *IEEE Journal of Photovoltaics* 4.6 (2014), pp. 1644–1649. DOI: 10.1109/JPHOTOV.2014.2350696.

[65] P. M. Salomé, B. Vermang, R. Ribeiro-Andrade, J. P. Teixeira, J. M. Cunha, M. J. Mendes, S. Haque, J. Borme, H. Águas, E. Fortunato, R. Martins, J. C. González, J. P. Leitão, P. A. Fernandes, M. Edoff, and S. Sadewasser. "Passivation of Interfaces in Thin Film Solar Cells: Understanding the Effects of a Nanostructured Rear Point Contact Layer." In: *Advanced Materials Interfaces* 5.2 (2018), p. 1701101. DOI: 10.1002/admi.201701101.

[66] W. W. Hsu, J. Y. Chen, T. H. Cheng, S. C. Lu, W. S. Ho, Y. Y. Chen, Y. J. Chien, and C. W. Liu. "Surface passivation of Cu(In,Ga)Se_2 using atomic layer deposited Al2O3." In: *Applied Physics Letters* 100.2 (2012), p. 023508. DOI: 10.1063/1.3675849.

[67] R Kotipalli, B Vermang, J Joel, R Rajkumar, M Edoff, and D Flandre. "Investigating the electronic properties of Al_2O_3/Cu(In,Ga)Se_2 interface." In: *AIP Advances* 5.10 (2015), p. 107101. DOI: 10.1063/1.4932512.

[68] J. M. Cunha, P. A. Fernandes, A. Hultqvist, J. P. Teixeira, S. Bose, B. Vermang, S. Garud, D. Buldu, J. Gaspar, M. Edoff, J. P. Leitao, and P. M. Salome. "Insulator Materials for Interface Passivation of Cu(In,Ga)Se_2 Thin Films." In: *IEEE Journal of Photovoltaics* 8.5 (2018), pp. 1313–1319. DOI: 10.1109/JPHOTOV.2018.2846674.

[69] B. Vermang, V. Fjällström, J. Pettersson, P. Salomé, and M. Edoff. "Development of rear surface passivated Cu(In,Ga)Se_2 thin film solar cells with nano-sized local rear point contacts." In: *Solar Energy Materials and Solar Cells* 117 (2013), pp. 505–511. DOI: 10.1016/j.solmat.2013.07.025.

[70] O. Poncelet, R. Kotipalli, B. Vermang, A. Macleod, L. A. Francis, and D. Flandre. "Optimisation of rear reflectance in ultra-thin CIGS solar cells towards >20% efficiency." In: *Solar Energy* 146 (2017), pp. 443–452. DOI: 10.1016/j.solener.2017.03.001.

[71] S. Bose, J. M. Cunha, J. Borme, W. C. Chen, N. S. Nilsson, J. P. Teixeira, J. Gaspar, J. P. Leitão, M. Edoff, P. A. Fernandes, and P. M. Salomé. "A morphological and electronic study of ultrathin rear passivated Cu(In,Ga)Se_2 solar cells." In: *Thin Solid Films* 671 (2019), pp. 77–84. DOI: 10.1016/j.tsf.2018.12.028.

[72] S. Bose, J. M. Cunha, S. Suresh, J. De Wild, T. S. Lopes, J. R. Barbosa, R. Silva, J. Borme, P. A. Fernandes, B. Vermang, and P. M. Salomé. "Optical Lithography Patterning of SiO_2 Layers for Interface Passivation of Thin Film Solar Cells." In: *Solar RRL* 2.12 (2018), p. 1800212. DOI: 10.1002/solr.201800212.

[73] J. M. Cunha, T. S. Lopes, S. Bose, A. Hultqvist, W. C. Chen, O. Donzel-Gargand, R. M. Ribeiro, A. J. Oliveira, M. Edoff, P. A. Fernandes, and P. M. Salome. "Decoupling of Optical and Electrical Properties of Rear Contact CIGS Solar Cells." In: *IEEE Journal of Photovoltaics* 9.6 (2019), pp. 1857–1862. DOI: 10.1109/JPHOTOV.2019.2933357.

[74] C. Van Lare, G. Yin, A. Polman, and M. Schmid. "Light Coupling and Trapping in Ultrathin Cu(In,Ga)Se_2 Solar Cells Using Dielectric Scattering Patterns." In: *ACS Nano* 9.10 (2015), pp. 9603–9613. DOI: 10.1021/acsnano.5b04091.

[75] A. J. N. Oliveira, J. D. Wild, K. Oliveira, B. A. Valença, J. P. Teixeira, J. R. L. Guerreiro, S. Abalde-Cela, T. S. Lopes, R. M. Ribeiro, J. M. V. Cunha, M. A. Curado, M. Monteiro, A. Violas, A. G. Silva, M. Prado, P. A. Fernandes, B. Vermang, and P. M. P. Salomé. "Encapsulation of Nanostructures in a Dielectric Matrix Providing Optical Enhancement in Ultra-thin Solar Cells." In: *Solar RRL* 4.11 (2020), p. 2000310. DOI: 10.1002/solr.202000310.

[76] G. Yin, A. Steigert, P. Andrae, M. Goebelt, M. Latzel, P. Manley, I. Lauermann, S. Christiansen, and M. Schmid. "Integration of plasmonic Ag nanoparticles as a back reflector in ultra-thin Cu(In,Ga)Se_2 solar cells." In: *Applied Surface Science* 355 (2015), pp. 800–804. DOI: 10.1016/j.apsusc.2015.07.195.

[77] L. Gouillart, W. C. Chen, A. Cattoni, J. Goffard, L. Riekehr, J. Keller, M. Jubault, N. Naghavi, M. Edoff, and S. Collin. "Reflective Back Contacts for Ultrathin Cu(In,Ga)Se_2-Based Solar Cells." In: *IEEE Journal of Photovoltaics* 10.1 (2020), pp. 250–254. DOI: 10.1109/JPHOTOV.2019.2945196.

[78] T. S. Lopes, J. M. Cunha, S. Bose, J. R. Barbosa, J. Borme, O. Donzel-Gargand, C. Rocha, R. Silva, A. Hultqvist, W. C. Chen, A. G. Silva, M. Edoff, P. A. Fernandes, and P. M. Salome. "Rear Optical Reflection and Passivation Using a Nanopatterned Metal/Dielectric Structure in Thin-Film Solar Cells." In: *IEEE Journal of Photovoltaics* 9.5 (2019), pp. 1421–1427. DOI: 10.1109/JPHOTOV.2019.2922323.

[79] G. Sozzi, F. Troni, and R. Menozzi. "Numerical analysis of the effect of grain size and defects on the performance of CIGS solar cells." In: *International Conference on Compound Semiconductor Manufacturing Technology, CS MANTECH*. Portland, Oregon, USA, 2010.

[80] G. Sozzi, F. Troni, and R. Menozzi. "On the combined effects of window/buffer and buffer/absorber conduction-band offsets, buffer thickness and doping on thin-film solar cell performance." In: *Solar Energy Materials and Solar Cells* 121 (2014), pp. 126–136. DOI: 10.1016/j.solmat.2013.10.037.

[81] G. Sozzi, S. DI Napoli, M. Enna, R. Menozzi, D. Hariskos, and W. Witte. "Numerical simulation of CIGS solar cells with Zn(O,S) or (Cd,Zn)S buffers and (Zn,Mg)O as high-resistive layer." In: *2019 IEEE 46th Photovoltaic Specialists Conference (PVSC)*. Chicago, IL, USA, 2019, pp. 2155–2158. DOI: 10.1109/PVSC40753.2019.8980882.

[82] T. M. Friedlmeier, P. Jackson, A. Bauer, D. Hariskos, O. Kiowski, R. Wuerz, and M. Powalla. "Improved Photocurrent in Cu(In,Ga)Se_2 Solar Cells: From 20.8 % to 21.7 % Efficiency with CdS Buffer and 21.0 % Cd-Free." In: *IEEE Journal of Photovoltaics* 5.5 (2015), pp. 1487–1491. DOI: 10.1109/JPHOTOV.2015.2458039.

[83] T. M. Friedlmeier, P. Jackson, A. Bauer, D. Hariskos, O. Kiowski, R. Menner, R. Wuerz, and M. Powalla. "High-efficiency Cu(In,Ga)Se_2 solar cells." In: *Thin Solid Films* 633 (2017), pp. 13–17. DOI: 10.1016/j.tsf.2016.08.021.

[84] F. Pianezzi, P. Reinhard, A. Chirilă, B. Bissig, S. Nishiwaki, S. Buecheler, and A. N. Tiwari. "Unveiling the effects of post-deposition treatment with different alkaline elements on the electronic properties of CIGS thin film solar cells." In: *Physical Chemistry Chemical Physics* 16.19 (2014), pp. 8843–8851. DOI: 10.1039/c4cp00614c.

[85] M. Burgelman, P. Nollet, and S. Degrave. "Modelling polycrystalline semiconductor solar cells." In: *Thin Solid Films* 361-362 (2000), pp. 527–532. DOI: 10.1016/S0040-6090(99)00825-1.

[86] H. Heriche, Z. Rouabah, and N. Bouarissa. "High-efficiency CIGS solar cells with optimization of layers thickness and doping." In: *Optik* 127.24 (2016), pp. 11751–11757. DOI: 10.1016/j.ijleo.2016.09.071.

[87] M. Mostefaoui, H. Mazari, S. Khelifi, A. Bouraiou, and R. Dabou. "Simulation of High Efficiency CIGS Solar Cells with SCAPS-1D Software." In: *Energy Procedia* 74 (2015), pp. 736–744. DOI: 10.1016/j.egypro.2015.07.809.

[88] T. Kodalle, T. Bertram, R. Schlatmann, and C. A. Kaufmann. "Effectiveness of an RbF Post Deposition Treatment of CIGS Solar Cells in Dependence on the Cu Content of the Absorber Layer." In: *IEEE Journal of Photovoltaics* 9.6 (2019), pp. 1839–1845. DOI: 10.1109/JPHOTOV.2019.2929418.

[89] Lumerical Inc. *Nanophotonic FDTD Simulation Software - Lumerical FDTD*. URL: https://www.lumerical.com/products/fdtd/ (visited on 11/24/2020).

[90] M. Burgelman and J. Marlein. "Analysis of graded band gap solar cells with scaps." In: *23rd European Photovoltaic Solar Energy Conference*. Valencia, Spain, 2008, pp. 2151–2155.

[91] O. Triebl. "Reliability Issues in High-Voltage Semiconductor Devices." Doctoral dissertation. Technical University of Wien, 2012. URL: https://www.iue.tuwien.ac.at/phd/triebl/main.html.

[92] H Neumann. "Optical properties and electronic band structure of $CuInSe_2$." In: *Solar Cells* 16 (1986), pp. 317–333.

[93] G. Coli and K. K. Bajaj. "Excitonic transitions in ZnO/MgZnO quantum well heterostructures." In: *Applied Physics Letters* 78.19 (2001), pp. 2861–2863. DOI: 10.1063/1.1370116.

[94] T. S. Lopes, J. De Wild, C. Rocha, A. Violas, J. M. V. Cunha, J. P. Teixeira, M. A. Curado, A. Oliveira, J. Borme, G. Birant, G. Brammertz, P. A. Fernandes, B. Vermang, and P. M. P. Salomé. "On the importance of joint mitigation strategies for front, bulk and rear recombination in ultrathin Cu(In,Ga)Se2 solar cells." In: submitted to *ACS Applied Materials and Interfaces* (2020).

[95] J. R. Barbosa. "Point contact structures for Thin Film Solar Cells." Master's thesis. NOVA University of Lisbon, School of Sciences and Technology, 2020.

[96] J. Lontchi, M. Zhukova, M. Kovacic, J. Krc, W. C. Chen, M. Edoff, S. Bose, P. M. Salome, J. Goffard, A. Cattoni, L. Gouillart, S. Collin, V. Gusak, and D. Flandre. "Optimization of Back Contact Grid Size in Al_2O_3-Rear-Passivated Ultrathin CIGS PV Cells by 2-D Simulations." In: *IEEE Journal of Photovoltaics* 10.6 (2020), pp. 1908–1917. DOI: 10.1109/JPHOTOV.2020.3012631.

[97] MicroChem Corporation. *LOR™ Lift-Off Resists datasheet*. 2002. URL: https://amolf.nl/wp-content/uploads/2016/09/datasheets_LOR_datasheet.pdf (visited on 11/20/2020).

[98] Merck Performance Materials GmbH. *AZ 1505 series datasheet*. URL: https://www.microchemicals.com/micro/tds_az_1500_series.pdf (visited on 11/20/2020).

[99] R. M. M. Ribeiro. "Development of a lift-off process for sub-micrometer structures implemented on ultra-thin film Cu(In,Ga)Se2 (CIGS) solar cells." Master's thesis. NOVA University of Lisbon, School of Sciences and Technology, 2019.

[100] R. Kotipalli, O. Poncelet, G. Li, Y. Zeng, L. A. Francis, B. Vermang, and D. Flandre. "Addressing the impact of rear surface passivation mechanisms on ultra-thin Cu(In,Ga)Se_2 solar cell performances using SCAPS 1-D model." In: *Solar Energy* 157 (2017), pp. 603–613. DOI: 10.1016/j.solener.2017.08.055.

[101] Y. Hirai, Y. Kurokawa, and A. Yamada. "Numerical study of Cu(In,Ga)Se2 solar cell performance toward 23% conversion efficiency." In: *Japanese Journal of Applied Physics* 53.1 (2014), p. 012301. DOI: 10.7567/JJAP.53.012301.

[102] N. Touafek and R. Mahamdi. "Back Surface Recombination Effect on the Ultra-Thin CIGS Solar Cells by SCAPS." In: *International Journal of Renewable Energy Research* 4.4 (2014), pp. 958–964. DOI: 10.20508/ijrer.02477.

[103] Y. Aida, V. Depredurand, J. K. Larsen, H. Arai, D. Tanaka, M. Kurihara, and S. Siebentritt. "Cu-rich $CuInSe_2$ solar cells with a Cu-poor surface." In: *Progress in Photovoltaics: Research and Applications* 23.6 (2015), pp. 754–764. DOI: 10.1002/pip.2493.

[104] M. Morkel, L. Weinhardt, B. Lohmüller, C. Heske, E. Umbach, W. Riedl, S. Zweigart, and F. Karg. "Flat conduction-band alignment at the CdS/$CuInSe_2$ thin-film solar-cell heterojunction." In: *Applied Physics Letters* 79.27 (2001), pp. 4482–4484. DOI: 10.1063/1.1428408.

[105] J. Song, S. S. Li, C. H. Huang, O. D. Crisalle, and T. J. Anderson. "Device modelling and simulation of the performance of $Cu(In_{1-x},Ga_x)Se_2$ solar cells." In: *Solid-State Electronics* 48.1 (2004), pp. 73–79. DOI: 10.1016/S0038-1101(03)00289-2.

[106] R. Carron, E. Avancini, T. Feurer, B. Bissig, P. A. Losio, R. Figi, C. Schreiner, M. Bürki, E. Bourgeois, Z. Remes, M. Nesladek, S. Buecheler, and A. N. Tiwari. "Refractive indices of layers and optical simulations of Cu(In,Ga)Se_2 solar cells." In: *Science and Technology of Advanced Materials* 19.1 (2018), pp. 396–410. DOI: 10.1080/14686996.2018.1458579.

[107] L. M. Mansfield, R. L. Garris, K. D. Counts, J. R. Sites, C. P. Thompson, W. N. Shafarman, and K. Ramanathan. "Comparison of CIGS Solar Cells Made with Different Structures and Fabrication Techniques." In: *IEEE Journal of Photovoltaics* 7.1 (2017), pp. 286–293. DOI: 10.1109/JPHOTOV.2016.2616188.

[108] M. A. Contreras, B. Egaas, K. Ramanathan, J. Hiltner, A. Swartzlander, F. Hasoon, and R. Noufi. "Progress toward 20% efficiency in Cu(In,Ga)Se_2 polycrystalline thin-film solar cells." In: *Progress in Photovoltaics: Research and Applications* 7.4 (1999), pp. 311–316. DOI: 10.1002/(SICI)1099-159X(199907/08)7:4<311::AID-PIP274>3.0.CO;2-G.

[109] M. Powalla, W. Witte, P. Jackson, S. Paetel, E. Lotter, R. Wuerz, F. Kessler, C. Tschamber, W. Hempel, D. Hariskos, R. Menner, A. Bauer, S. Spiering, E. Ahlswede, T. M. Friedlmeier, D. Blázquez-Sánchez, I. Klugius, and W. Wischmann. "CIGS cells and modules with high efficiency on glass and flexible substrates." In: *IEEE Journal of Photovoltaics* 4.1 (2014), pp. 440–446. DOI: 10.1109/JPHOTOV.2013.2280468.

[110] Y. Wang, T. Muryobayashi, K. Nakada, Z. Li, and A. Yamada. "Correlation between carrier recombination and valence band offset effect of graded Cu(In,Ga)Se_2 solar cells." In: *Solar Energy Materials and Solar Cells* 201 (2019), p. 110070. DOI: 10.1016/j.solmat.2019.110070.

[111] T. Nishimura, S. Toki, H. Sugiura, K. Nakada, and A. Yamada. "Effect of Cu-deficient layer formation in Cu(In,Ga)Se_2 solar-cell performance." In: *Progress in Photovoltaics: Research and Applications* 26.4 (2018), pp. 291–302. DOI: 10.1002/pip.2972.

[112] T. Nishimura, H. Sugiura, K. Nakada, and A. Yamada. "Characterization of Interface Between Accurately Controlled Cu-Deficient Layer and Cu(In,Ga)Se_2 Absorber for Cu(In,Ga)Se_2 Solar Cells." In: *Physica Status Solidi - Rapid Research Letters* 12.8 (2018), p. 1800129. DOI: 10.1002/pssr.201800129.

[113] S. H. Wei and S. B. Zhang. "Defect properties of $CuInSe_2$ and $CuGaSe_2$." In: *Journal of Physics and Chemistry of Solids* 66.11 (2005), pp. 1994–1999. DOI: 10.1016/j.jpcs.2005.10.003.

[114] S. Chatraphorn, K. Yoodee, P. Songpongs, C. Chityuttakan, K. Sayavong, S. Wongmanerod, and P. O. Holtz. "Photoluminescence of a high quality $CuInSe_2$ single crystal." In: *Japanese Journal of Applied Physics* 37.Part 2, No. 3A (1998), pp. L269–L271. DOI: 10.1143/jjap.37.l269.

[115] H. J. Möller and E. M. Rodak. "Investigation of the defect chemistry of $CuInSe_2$ single crystals by DLTS measurements." In: *Tenth E.C. Photovoltaic Solar Energy Conference*. Lisbon, Portugal, 1991, pp. 913–916. DOI: 10.1007/978-94-011-3622-8.

[116] A. L. Li and I. Shih. "Majority and minority carrier traps in monocrystalline $CuInSe_2$." In: *Journal of Electronic Materials* 22.2 (1993), pp. 195–199. DOI: 10.1007/BF02665026.

[117] A. M. Bakry and A. M. Elnaggar. "Study of deep levels in Schottky/$CuInSe_2$ single-crystal devices by deep-level transient spectroscopy measurements." In: *Journal of Materials Science: Materials in Electronics* 7.3 (1996), pp. 191–192. DOI: 10.1007/bf00133114.

[118] K. Taretto and U. Rau. "Numerical simulation of carrier collection and recombination at grain boundaries in Cu(In,Ga)Se2 solar cells." In: *Journal of Applied Physics* 103.9 (2008), p. 094523. DOI: 10.1063/1.2917293.

[119] M. Gloeckler, J. R. Sites, and W. K. Metzger. "Grain-boundary recombination in Cu(In,Ga)Se_2 solar cells." In: *Journal of Applied Physics* 98.11 (2005), p. 113704. DOI: 10.1063/1.2133906.

[120] S. Siebentritt and S. Schuler. "Defects and transport in the wide gap chalcopyrite $CuGaSe_2$." In: *Journal of Physics and Chemistry of Solids* 64.9-10 (2003), pp. 1621–1626. DOI: 10.1016/S0022-3697(03)00150-1.

[121] S. Sadewasser, T. Glatzel, S. Schuler, S. Nishiwaki, R. Kaigawa, and M. C. Lux-Steiner. "Kelvin probe force microscopy for the nano scale characterization of chalcopyrite solar cell materials and devices." In: *Thin Solid Films* 431-432 (2003), pp. 257–261. DOI: 10.1016/S0040-6090(03)00267-0.

[122] G. Hanna, T. Glatzel, S. Sadewasser, N. Ott, H. P. Strunk, U. Rau, and J. H. Werner. "Texture and electronic activity of grain boundaries in Cu(In,Ga)Se_2 thin films." In: *Applied Physics A: Materials Science and Processing* 82.1 (2006), pp. 1–7. DOI: 10.1007/s00339-005-3411-1.

[123] I. Repins, M. A. Contreras, B. Egaas, C. DeHart, J. Scharf, C. L. Perkins, B. To, and R. Noufi. "19.9 % - efficient ZnO/CdS/ CuInGaSe2 Solar Cell with 81.8 % Fill Factor." In: *Progress in Photovoltaics: Research and Applications* 16.3 (2008), pp. 235–239. DOI: 10.1002/pip.822.

[124] C. Frisk, C. Platzer-Björkman, J. Olsson, P. Szaniawski, J. T. Wätjen, V. Fjällström, P. Salomé, and M. Edoff. "Optimizing Ga-profiles for highly efficient Cu(In,Ga)Se_2 thin film solar cells in simple and complex defect models." In: *Journal of Physics D: Applied Physics* 47.48 (2014), p. 485104. DOI: 10.1088/0022-3727/47/48/485104.

[125] R. Kotipalli, B. Vermang, V. Fjällström, M. Edoff, R. Delamare, and D. Flandre. "Influence of Ga/(Ga + In) grading on deep-defect states of Cu(In,Ga)Se_2 solar cells." In: *Physica Status Solidi - Rapid Research Letters* 9.3 (2015), pp. 157–160. DOI: 10.1002/pssr.201510024.

[126] A. Laemmle, R. Wuerz, and M. Powalla. "Efficiency enhancement of Cu(In,Ga)Se_2 thin-film solar cells by a post-deposition treatment with potassium fluoride." In: *Physica Status Solidi - Rapid Research Letters* 7.9 (2013), pp. 631–634. DOI: 10.1002/pssr.201307238.

[127] C. P. Muzzillo. "Review of grain interior, grain boundary, and interface effects of K in CIGS solar cells: Mechanisms for performance enhancement." In: *Solar Energy Materials and Solar Cells* 172 (2017), pp. 18–24. DOI: 10.1016/j.solmat.2017.07.006.

[128] S. Siebentritt, E. Avancini, M. Bär, J. Bombsch, E. Bourgeois, S. Buecheler, R. Carron, C. Castro, S. Duguay, R. Félix, E. Handick, D. Hariskos, V. Havu, P. Jackson, H. P. Komsa, T. Kunze, M. Malitckaya, R. Menozzi, M. Nesladek, N. Nicoara, M. Puska, M. Raghuwanshi, P. Pareige, S. Sadewasser, G. Sozzi, A. N. Tiwari, S. Ueda, A. Vilalta-Clemente, T. P. Weiss, F. Werner, R. G. Wilks, W. Witte, and M. H. Wolter. "Heavy Alkali Treatment of Cu(In,Ga)Se_2 Solar Cells: Surface versus Bulk Effects." In: *Advanced Energy Materials* 10.8 (2020), p. 1903752. DOI: 10.1002/aenm.201903752.

[129] M. Malitckaya, H. P. Komsa, V. Havu, and M. J. Puska. "Effect of Alkali Metal Atom Doping on the $CuInSe_2$-Based Solar Cell Absorber." In: *Journal of Physical Chemistry C* 121.29 (2017), pp. 15516–15528. DOI: 10.1021/acs.jpcc.7b03083.

[130] N. Nicoara, R. Manaligod, P. Jackson, D. Hariskos, W. Witte, G. Sozzi, R. Menozzi, and S. Sadewasser. "Direct evidence for grain boundary passivation in Cu(In,Ga)Se_2 solar cells through alkali-fluoride post-deposition treatments." In: *Nature Communications* 10.1 (2019), pp. 1–8. DOI: 10.1038/s41467-019-11996-y.

[131] K. F. Tai, R. Kamada, T. Yagioka, T. Kato, and H. Sugimoto. "From 20.9 to 22.3% Cu(In,Ga)$(S,Se)_2$ solar cell: Reduced recombination rate at the heterojunction and the depletion region due to K-treatment." In: *Japanese Journal of Applied Physics* 56.8S2 (2017), p. 08MC03. DOI: 10.7567/JJAP.56.08MC03.

[132] I. M. Dharmadasa. "Fermi level pinning and effects on $CuInGaSe_2$-based thin-film solar cells." In: *Semiconductor Science and Technology* 24.5 (2009), p. 055016. DOI: 10.1088/0268-1242/24/5/055016.

[133] M. Turcu and U. Rau. "Numerical simulations." In: *Wide-gap Chalcopyrites*. Springer, 2006. Chap. Recombination Mechanisms in Cu(In,Ga)$(Se,S)_2$ Solar Cells, pp. 102–108.

[134] S.-H. Wei and A. Zunger. "Band offsets at the CdS/$CuInSe_2$ heterojunction." In: *Applied Physics Letters* 63.18 (1993), pp. 2549–2551. DOI: 10.1063/1.110429.

[135] T. Minemoto, T. Matsui, H. Takakura, Y. Hamakawa, T. Negami, Y. Hashimoto, T. Uenoyama, and M. Kitagawa. "Theoretical analysis of the effect of conduction band offset of window/CIS layers on performance of CIS solar cells using device simulation." In: *Solar Energy Materials and Solar Cells* 67.1-4 (2001), pp. 83–88. DOI: 10.1016/S0927-0248(00)00266-X.

[136] S. Kumar, V. Gupte, and K. Sreenivas. "Structural and optical properties of magnetron sputtered $Mg_xZn_{1-x}O$ thin films." In: *Journal of Physics Condensed Matter* 18.13 (2006), pp. 3343–3354. DOI: 10.1088/0953-8984/18/13/002.

[137] T. Hara, T. Maekawa, S. Minoura, Y. Sago, S. Niki, and H. Fujiwara. "Quantitative assessment of optical gain and loss in submicron-textured $CuIn_{1-x}Ga_xSe_2$ solar cells fabricated by three-stage coevaporation." In: *Physical Review Applied* 2.3 (2014), p. 034012. DOI: 10.1103/PhysRevApplied.2.034012.

[138] P. Jackson, R. Würz, U. Rau, J. Mattheis, M. Kurth, T. Schlötzer, G. Bilger, and J. H. Werner. "High Quality Baseline for High Efficiency, Cu(In_{1-x},Ga_x)Se_2 Solar Cells." In: *Progress in Photovoltaics: Research and Applications* 15.6 (2007), pp. 507–519. DOI: 10.1002/pip.757.

[139] S. Cheng, B. Li, W. Liu, K. Zhang, Y. Zhang, Z. He, L. Lin, S. Sun, and Y. Sun. "Analyzing the causes of limited performance improvement in cigs devices after potassium fluoride post-deposition treatment using SCAPS." In: *Optik* 219 (2020), p. 164757. DOI: 10.1016/j.ijleo.2020.164757.

[140] J. D. Wild, D. G. Buldu, T. Schnabel, M. Simor, T. Kohl, G. Birant, G. Brammertz, M. Meuris, J. Poortmans, and B. Vermang. "High V_{oc} upon KF post deposition treatment for ultrathin single-stage co-evaporated Cu(In,Ga)Se_2 solar cells." In: *ACS Applied Energy Materials* 2.8 (2019), pp. 6102–6111. DOI: 10.1021/acsaem.9b01370.

[141] J. M. V. Cunha, K. Oliveira, J. Lontchi, T. S. Lopes, M. A. Curado, J. R. S. Barbosa, C. Vinhais, W.-c. Chen, J. Borme, H. Fonseca, J. Gaspar, D. Flandre, M. Edoff, A. G. Silva, J. P. Teixeira, P. A. Fernandes, and P. M. P. Salomé. "High-performance and Industrially Viable Nanostructured SiO_x Layers for Interface Passivation in Thin Film Solar Cells." In: submitted to *Solar RRL* (2020).

[142] A. Hultqvist, T. Sone, and S. F. Bent. "Buffer Layer Point Contacts for CIGS Solar Cells Using Nanosphere Lithography and Atomic Layer Deposition." In: *IEEE Journal of Photovoltaics* 7.1 (2017), pp. 322–328. DOI: 10.1109/JPHOTOV.2016.2627621.

A | SCAPS-1D Parameters

Table A.1: Parameters used in SCAP-1D for the initial model. All defects are mid-gap defects, except for the E_F pinning interface defect which are placed 0.2 eV below E_c. See Symbols chapter for all parameters meaning. "A" stands for acceptor, "D" for donor, and "N" for neutral. This initial model represents the previous baseline from Pettersson *et al.* [15].

Layer properties	**CIGS**	**SDL**	**CdS**	**i:ZnO**	**AZO**
Thickness (μm)	1.8	0.015	0.05	0.1	0.3
E_g (eV)	1.34 -1.08 (graded)	1.3	2.4	3.3	3.3
χ_a (eV)	4.20 - 4.46 (graded)	4.46	4.46	4.66	4.66
ϵ_r	13.6	13.6	5.4	9	9
N_c (cm^{-3})	6.8×10^{17}	6.8×10^{17}	1.3×10^{18}	3.0×10^{18}	3.0×10^{18}
N_v (cm^{-3})	1.5×10^{19}	1.5×10^{19}	9.1×10^{18}	1.7×10^{19}	1.7×10^{19}
v_{th}^{e} ($cm\cdot s^{-1}$)	3.9×10^{7}	3.9×10^{7}	3.1×10^{7}	2.4×10^{7}	2.4×10^{7}
v_{th}^{h} ($cm\cdot s^{-1}$)	1.4×10^{7}	1.4×10^{7}	1.6×10^{7}	1.3×10^{7}	1.3×10^{7}
μ_e ($cm^2\cdot V^{-1}s^{-1}$)	100	100	72	100	100
μ_h ($cm^2\cdot V^{-1}s^{-1}$)	12.5	12.5	20	31	31
N_D (cm^{-3})	–	–	5.0×10^{17}	1.0×10^{17}	1.0×10^{20}
N_A (cm^{-3})	1.0×10^{16}	1.0×10^{16}	–	–	–
Abs. coeff. (cm^{-1})	[32]	[32]	[106]	[106]	[106]
Bulk defects					
Type	Single (D)	Single (D)	Single (A)	Single (A)	Single (A)
σ_e (cm^2)	1.0×10^{-13}	1.0×10^{-13}	1.0×10^{-15}	1.0×10^{-15}	1.0×10^{-15}
σ_h (cm^2)	1.0×10^{-15}	1.0×10^{-15}	5.0×10^{-13}	5.0×10^{-13}	5.0×10^{-13}
N_t (cm^{-3})	1.0×10^{14}	1.0×10^{14}	5.0×10^{16}	1.0×10^{16}	1.0×10^{16}
Interface defects		**SDL/CdS**			
	CIGS/SDL	Recomb.	Pinning		
Type	Single (N)	Single (N)	Single (D)		
σ_e (cm^2)	1.0×10^{-15}	1.0×10^{-15}	1.0×10^{-18}		
σ_h (cm^2)	1.0×10^{-15}	1.0×10^{-15}	1.0×10^{-18}		
N_{it} (cm^{-2})	1.0×10^{11}	3.0×10^{13}	3.0×10^{13}		
Contacts	**Rear**	**Front**			
Electrons SRV ($cm\cdot s^{-1}$)	1.0×10^{7}	1.0×10^{7}			
Holes SRV ($cm\cdot s^{-1}$)	1.0×10^{7}	1.0×10^{7}			
Reflection (%)	0	0			

Table A.2: Parameters used in SCAP-1D for the baseline model for high-efficiency devices obtained with this study. The interface defects are the same as in Table A.1, except the removal of the E_F pinning defect. Furthermore, the optical reflection simulations are presented and discussed in chapter 3. See Symbols chapter for all parameters meaning. "A" stands for acceptor, and "D" for donor.

Layer properties	**CIGS**	**SDL**	**CdS**	**ZMO**	**AZO**
Thickness (μm)	2.5	0.015	0.021	0.05	0.15
E_g (eV)	1.31 - 1.11 - 1.27 double graded	1.42	2.4	3.8	3.3
χ_a (eV)	4.22 - 4.43 - 4.31 double graded	4.31	4.11	4.21	4.21
ϵ_r	13.6	13.6	5.4	9	9
N_c (cm^{-3})	6.8×10^{17}	6.8×10^{17}	1.3×10^{18}	3.0×10^{18}	3.0×10^{18}
N_v (cm^{-3})	1.5×10^{19}	1.5×10^{19}	9.1×10^{18}	1.7×10^{19}	1.7×10^{19}
v_{th}^{e} (cm$\cdot$s^{-1})	3.9×10^{7}	3.9×10^{7}	3.1×10^{7}	2.4×10^{7}	2.4×10^{7}
v_{th}^{h} (cm$\cdot$s^{-1})	1.4×10^{7}	1.4×10^{7}	1.6×10^{7}	1.3×10^{7}	1.3×10^{7}
μ_e (cm$^2\cdot$V^{-1}s^{-1})	100	100	72	100	100
μ_h (cm$^2\cdot$V^{-1}s^{-1})	12.5	12.5	20	31	31
N_D (cm^{-3})	1.0×10^{16}	1.0×10^{16}	5.0×10^{17}	1.0×10^{17}	1.0×10^{20}
N_A (cm^{-3})	5.0×10^{16} - 1.1×10^{16} wo type-inv. 5.0×10^{16} - 1.0×10^{14} type-inv.	1.1×10^{16} wo type-inv. 1.0×10^{14} type-inv.	–	–	–
Abs. coeff. (cm^{-1})	[32]	[32]	[106]	[136]	[106]
Bulk defects					
1 - Type	Double (D)	Double (D)	Single (A)	Single (A)	Single (A)
1 - σ_e (cm^2)	1.0×10^{-13}	1.0×10^{-13}	1.0×10^{-15}	1.0×10^{-15}	1.0×10^{-15}
1 - σ_h (cm^2)	1.0×10^{-15}	1.0×10^{-15}	5.0×10^{-13}	5.0×10^{-13}	5.0×10^{-13}
1 - E_t (eV)	$E_c - 0.25$ / $E_c - 0.34$	$E_c - 0.25$ / $E_c - 0.34$	mid-gap	mid-gap	mid-gap
1 - N_t (cm^{-3})	1.0×10^{13}	1.0×10^{13}	5.0×10^{16}	1.0×10^{16}	1.0×10^{16}
2 - Type	Double (A)	Double (A)			
2 - σ_e (cm^2)	1.0×10^{-15}	1.0×10^{-15}			
2 - σ_h (cm^2)	1.0×10^{-13}	1.0×10^{-13}			
2 - E_t (eV)	$E_v + 0.29$ / $E_v + 0.58$	$E_v + 0.29$ / $E_v + 0.58$			
2 - N_t (cm^{-3})	1.0×10^{13}	1.0×10^{13}			
3 - Type (GB)	Single (A/D)	Single (A/D)			
3 - σ_e (cm^2)	1.0×10^{-15}	1.0×10^{-15}			
3 - σ_h (cm^2)	1.0×10^{-15}	1.0×10^{-15}			
3 - E_t (eV)	$E_v + 0.27$	$E_v + 0.27$			
3 - N_t (cm^{-3})	5.0×10^{13} - 5.0×10^{12}	5.0×10^{12}			
Contacts	**Rear**	**Front**			
El. SRV (cm$\cdot$s^{-1})	1.0×10^{7}	1.0×10^{7}			
Hole SRV (cm$\cdot$s^{-1})	1.0×10^{7}	1.0×10^{7}			
Reflection (%)	optical sim.	optical sim.			

Table A.3: Parameters used in SCAP-1D for the baseline model for ultra-thin devices. The interface defects are the same as in Table A.1, except the removal of the E_F pinning defect. Furthermore, the optical reflection simulation is presented and discussed in chapter 3. See Symbols chapter for all parameters meaning. "A" stands for acceptor, and "D" for donor.

Layer properties	**CIGS bulk**	**SDL**	**CdS**	**i:ZnO**	**AZO**
Thickness (nm)	425	15	50	100	400
E_g (eV)	[94]	1.42	2.4	3.3	3.3
χ_a (eV)	[94]	4.31	4.11	4.31	4.31
ϵ_r	13.6	13.6	5.4	9	9
N_c (cm^{-3})	6.8×10^{17}	6.8×10^{17}	1.3×10^{18}	3.0×10^{18}	3.0×10^{18}
N_v (cm^{-3})	1.5×10^{19}	1.5×10^{19}	9.1×10^{18}	1.7×10^{19}	1.7×10^{19}
v_{th}^{e} ($cm\cdot s^{-1}$)	3.9×10^{7}	3.9×10^{7}	3.1×10^{7}	2.4×10^{7}	2.4×10^{7}
v_{th}^{h} ($cm\cdot s^{-1}$)	1.4×10^{7}	1.4×10^{7}	1.6×10^{7}	1.3×10^{7}	1.3×10^{7}
μ_e ($cm^2\cdot V^{-1}s^{-1}$)	100	100	72	100	100
μ_h ($cm^2\cdot V^{-1}s^{-1}$)	12.5	12.5	20	31	31
N_D (cm^{-3})	–	1.0×10^{16}	5.0×10^{17}	1.0×10^{17}	1.0×10^{20}
N_A (cm^{-3})	6.05×10^{15} (PDT) 4.05×10^{15} (wo PDT)	1.0×10^{14}	–	–	–
Abs. coeff. (cm^{-2})	[32]	[32]	[106]	[106]	[106]
Bulk defects					
Defects 1 & 2 Double (D & A)	Table A.2	Table A.2	–	–	–
3 - Type (GB)	Single (A/D)	Single (A/D)	Single (A)	Single (A)	Single (A)
3 - σ_e (cm^2)	1.0×10^{-13}	1.0×10^{-13}	1.0×10^{-15}	1.0×10^{-15}	1.0×10^{-15}
3 - σ_h (cm^2)	1.0×10^{-15}	1.0×10^{-15}	5.0×10^{-13}	5.0×10^{-13}	5.0×10^{-13}
3 - E_t (eV)	E_v + 0.27	E_v + 0.27	mid-gap	mid-gap	mid-gap
3 - N_t (cm^{-3})	5.0×10^{15} - 2.0×10^{15} (PDT) 1.5×10^{16} (wo PDT)	2.0×10^{15} (PDT) 1.5×10^{16} (wo PDT)	4.7×10^{17}	1.0×10^{16}	1.0×10^{16}
Contacts	**Rear**	**Front**			
El. SRV ($cm\cdot s^{-1}$)	1.0×10^{2} (pass) 1.0×10^{7} (wo pass)	1.0×10^{7}			
Hole SRV ($cm\cdot s^{-1}$)	1.0×10^{7}	1.0×10^{7}			
Reflection (%)	50 (pass) 30 (wo pass)	optical sim.			

B | Supplementary Figures and Tables

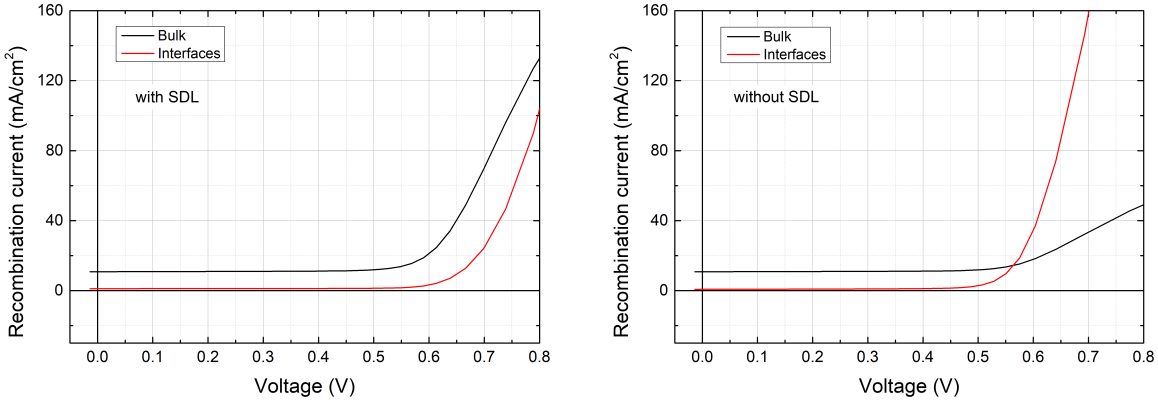

Figure B.1: Bulk and interface recombination currents with (left) and without (right) the SDL layer.

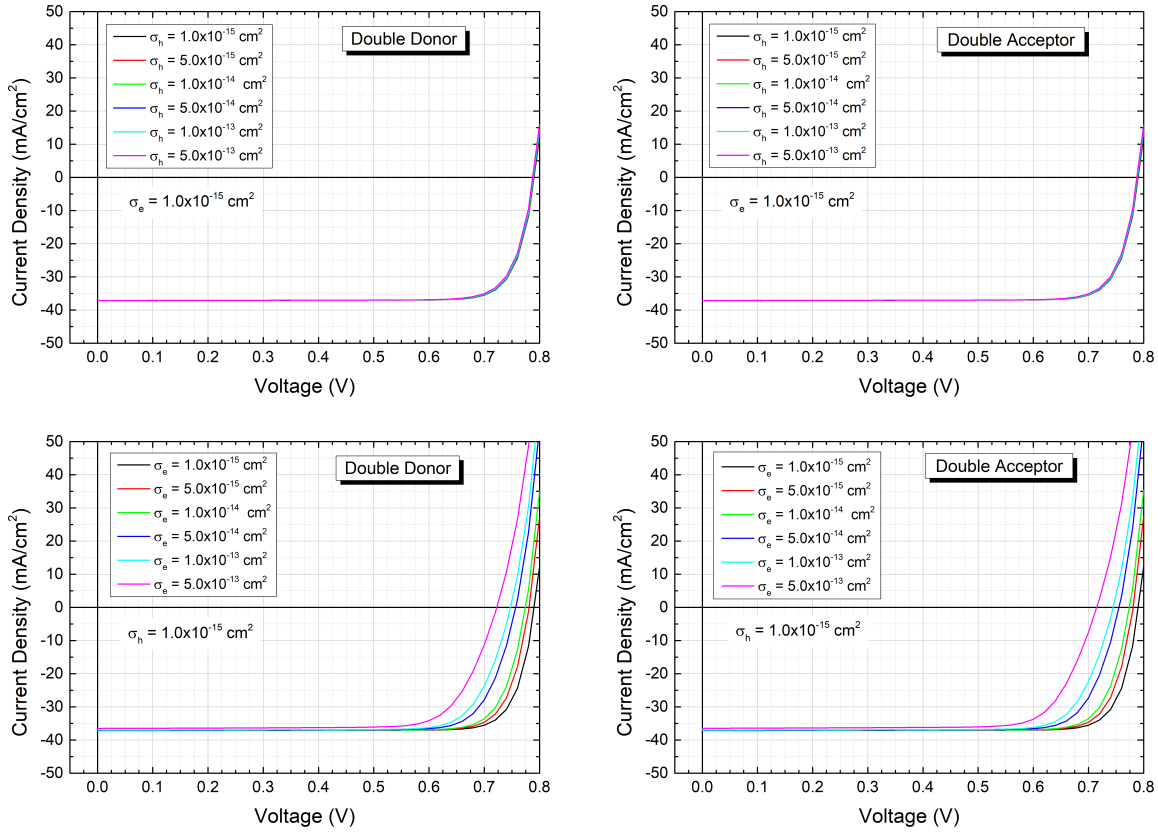

Figure B.2: Cross-section test with the variation of electrons (bottom) and holes (top) capture cross-section, in the double donors (left) and double acceptors (right) defects.

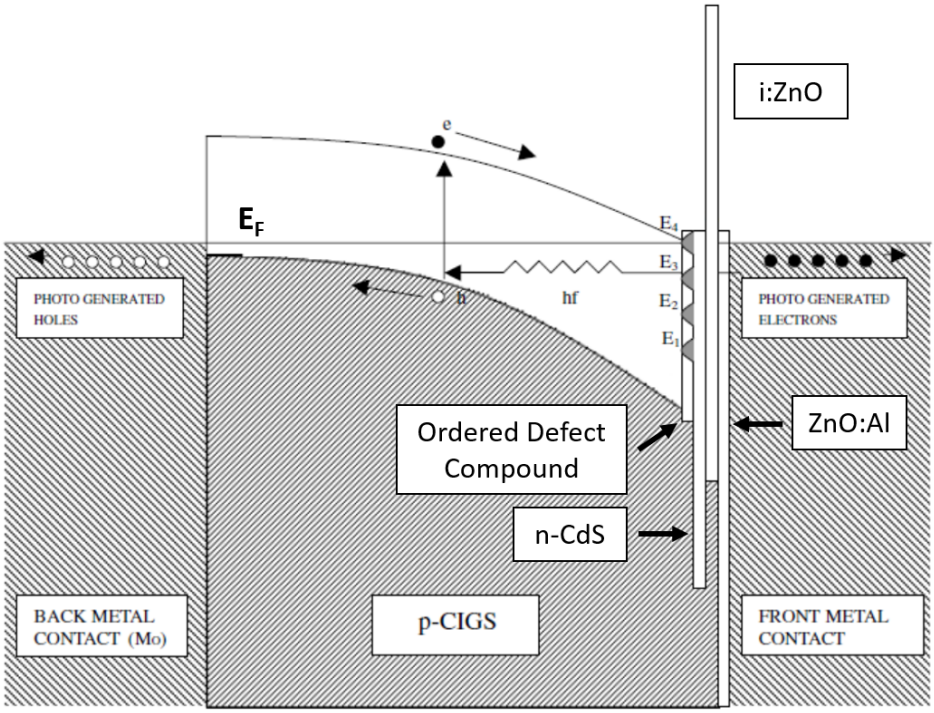

Figure B.3: Band diagram adapted from [132] illustrating the Fermi level (E_F) pinning process. Here E_F is pinned at energy E_4, with other possible three defect levels at the interface. The E_F pinning at E_4 provides the highest V_{oc} in opposition with the pinning at E_1.

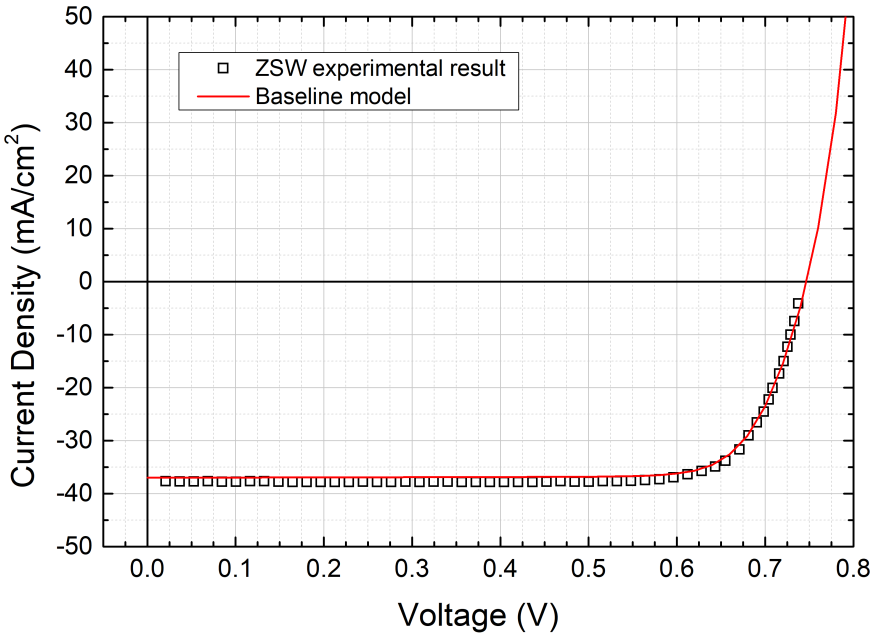

Figure B.4: J-V curve comparison between the baseline model obtained with this study and the experimental result of the high-efficiency record cell from ZSW.

Table B.1: Resume of the simulation results for the optical optimisation steps of the baseline model to high-efficiency devices, without considering the ARC optimisations.

CIGS model	V_{oc} (mV)	J_{sc} (mA · cm^{-2})	FF (%)	η (%)
CBO update (previous)	745	35.4	80.4	21.2
CdS thickness reduction	746	36.4	80.3	21.8
i:ZnO to ZMO	747	36.6	80.3	21.9
ZMO thickness reduction	747	36.6	80.3	21.9
AZO thickness reduction	748	37.3	80.3	22.4
Rear reflection update	749	38.2	80.2	22.9
Fixed front reflection (2.7 %)	747	37.2	80.3	22.3

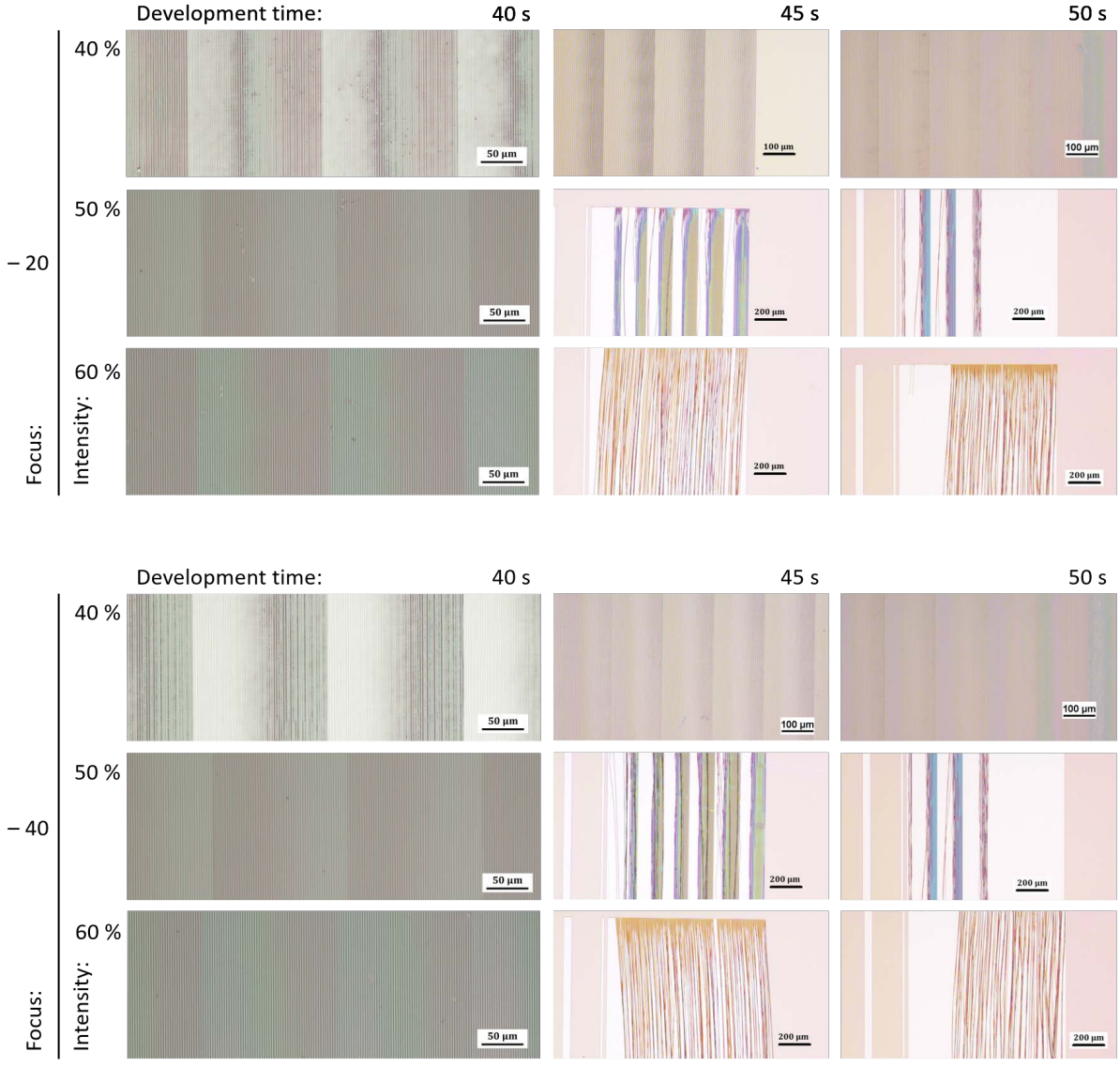

Figure B.5: Optical microscope images for the calibration of the DWL laser Focus and Intensity conditions together with the development time. All the exposed lines presented here have 1.6 μm width and 2.8 μm pitch. Note the different scale unit at different images.

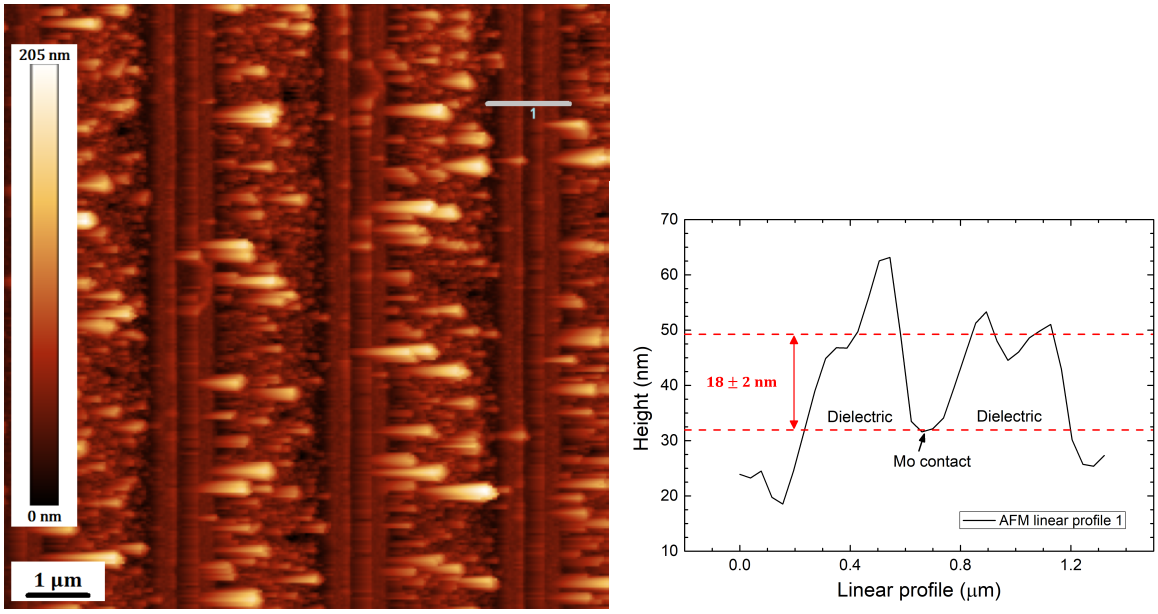

Figure B.6: AFM analysis of the substrate after the lift-off, the correspondent SEM image is shown in Figure 3.15 b) and c). It is demonstrated the dielectric thickness with the linear profile (right) through 10 measurements at different locations, and as an example it is presented the referred linear profile on the gray line at AFM image (left).

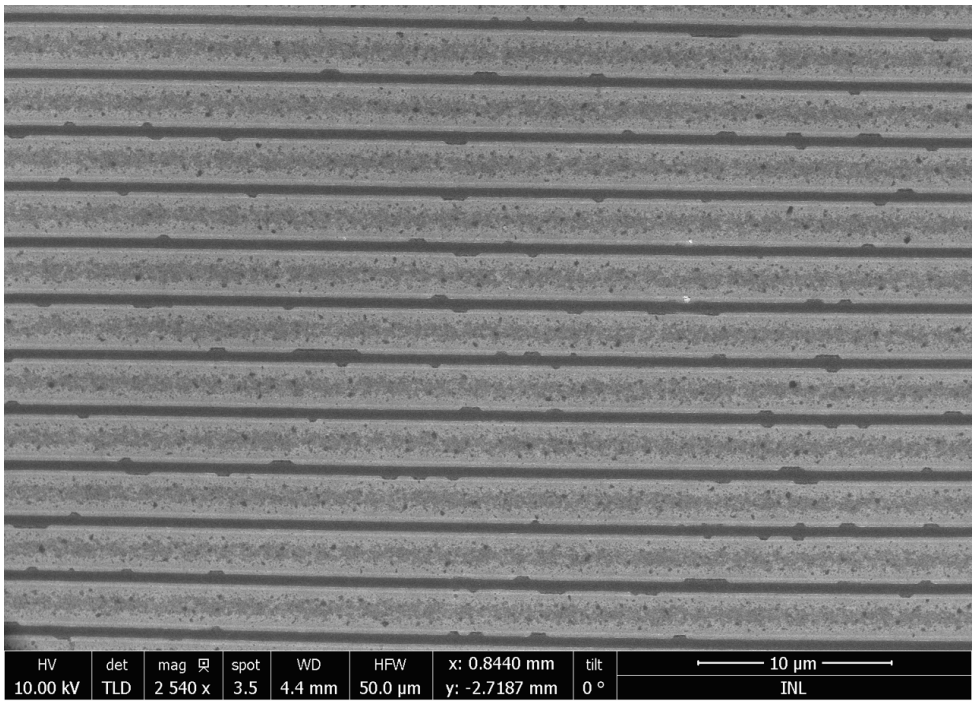

Figure B.7: SEM top image pf the substrate after the lift-off. This SEM image is an example of the uniformity of the lines dimension obtained with this study.

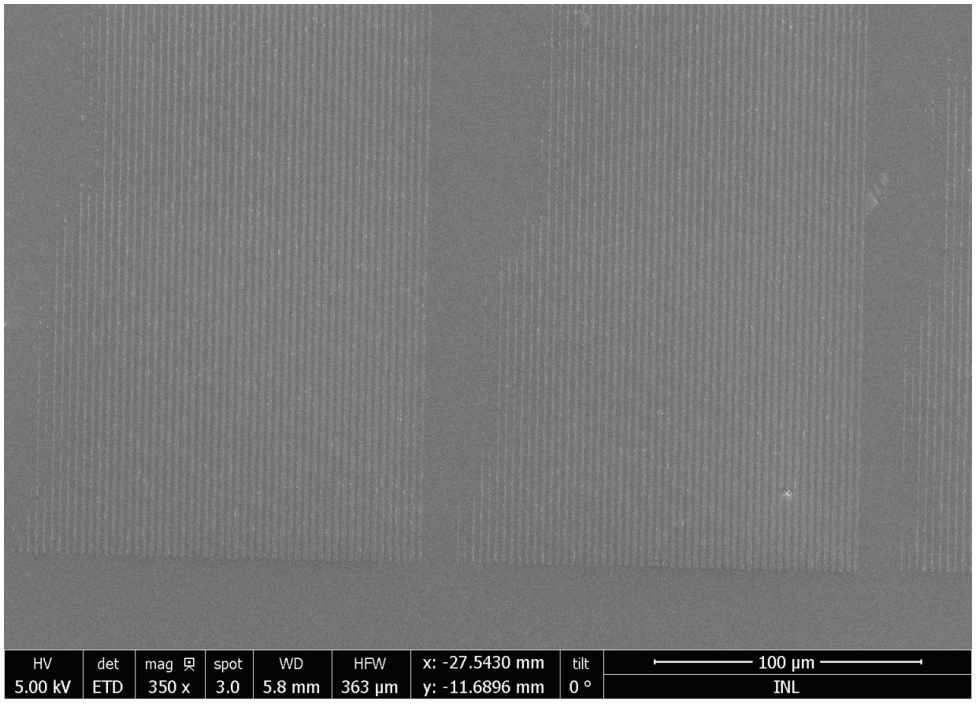

Figure B.8: SEM image of the successful lift-off of the ALD alumina deposited at $\approx 100\,^{o}$C. However, this lift-off was done before the DWL exposure calibration to assess the viability of the ALD high-quality dielectric lift-off and does not have the proper line dimensions, as it is possible to see by the areas without lines where the resist peeled-off.

I Program to Retrieve Figures of Merit in SCAPS-1D

Throughout the first simulations results it became clear that I should automate the process of retrieving the Figures of Merit values from a series or a batch of simulation results. Initially, I had to write one-by-one all the values from .txt files with the simulations results. So, I create a Visual Basic for Applications (VBA) program in Excel that stores the Figures of Merit values, based on the .txt file provided by the SCAPS-1D J-V simulations, into an Excel table to be further used. Therefore, the process of obtaining the respective Figures of Merit is simplified compared to the initial copy and paste time-consuming approach.

Figure I.1 presents the output Excel sheet, whereas the input .txt file path, batch and I-V parameters are inserted. The click on *Calculate Figures of Merit* button place the results in the respective grey cells.

	A	B	C	D	E	F	G	H	I	J	K	L	M	N	O	P	Q
1	File folder (complete path)	C:\Users\ASUS\Desktop\FCT\5A\2ºS\DEMN(MI)\SCAPS-1D\Results\Modelos CIGS\2020-07-08_To ZSW - Front and Back Reflection tunning\Front Reflection - Ga 0.15\Updat															
2	# Batch par. (0 if not batch)	0															
3	IV parameters	Voc begin	0	Voc end	0.8	Step	0.02	Nº points	41								
4																	
5	Step	Voc (mV)	Jsc (mA/cm2)	FF (%)	η (%)												
6	1	745.55	36.05064	80.327	21.59												
7	2	745.92	36.31594	80.316	21.757												
8	3	746.17	36.491	80.31	21.867												
9	4	746.3	36.578	80.308	21.922												
10	5	746.32	36.590	80.308	21.93												
11	6	746.31	36.585	80.31	21.927												
12	7	746.23	36.523	80.314	21.889												
13	8	746.07	36.411	80.321	21.819												
14	9	745.87	36.268	80.328	21.73												
15																	
16																	
17																	
18																	
19																	
20																	

Calculate Figures of Merit

Figure I.1: Example of an output Excel sheet of the VBA program to retrieve the Figures of Merit from the .txt file obtained with the SCAPS-1D simulation results.

It also shown an example of how the SCAPS-1D software outputs the Figures of Merit values in the text files, Figure I.2, whereas the difficulty of obtaining several groups of these values, as an example with batch simulations, is visible.

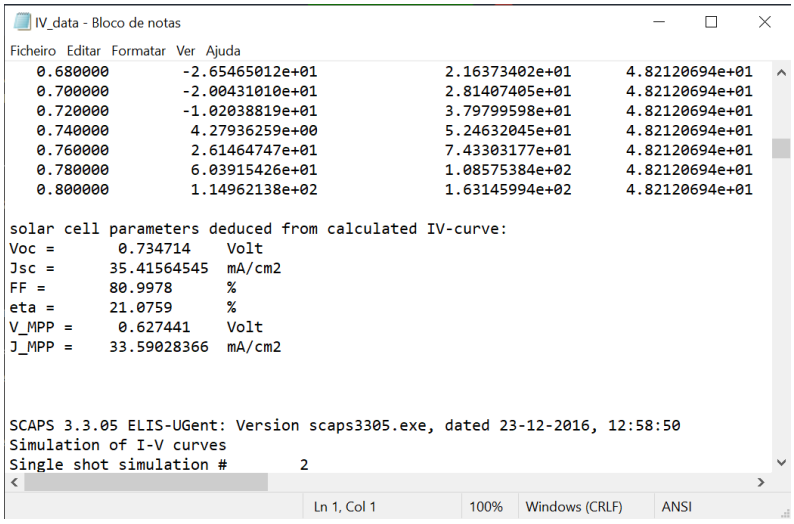

Figure I.2: Example of an output .txt file obtained with SCAPS-1D I-V simulations with the Figures of Merit values.